Western Graduate&PostdoctoralStudies

Western University
Scholarship@Western

Electronic Thesis and Dissertation Repository

9-19-2011 12:00 AM

Hyperthermal H2 Induced C–H Bond Cleavage: A Novel Approach To Cross-linking Of Organic Molecules

Tomas Trebicky, *The University of Western Ontario*

Supervisor: Dr. Leo W. M. Lau, *The University of Western Ontario*

A thesis submitted in partial fulfillment of the requirements for the Doctor of Philosophy degree in Physics

© Tomas Trebicky 2011

Follow this and additional works at: https://ir.lib.uwo.ca/etd

Part of the Condensed Matter Physics Commons

Recommended Citation

Trebicky, Tomas, "Hyperthermal H2 Induced C–H Bond Cleavage: A Novel Approach To Cross-linking Of Organic Molecules" (2011). *Electronic Thesis and Dissertation Repository*. 270.
https://ir.lib.uwo.ca/etd/270

This Dissertation/Thesis is brought to you for free and open access by Scholarship@Western. It has been accepted for inclusion in Electronic Thesis and Dissertation Repository by an authorized administrator of Scholarship@Western. For more information, please contact wlswadmin@uwo.ca.

Hyperthermal H_2 Induced C–H Bond Cleavage: A Novel Approach To Cross-linking Of Organic Molecules

(Spine title: Hyperthermal Hydrogen Induced Cross-linking)

(Thesis format: Monograph)

by

Tomas Trebicky

Graduate Program in Physics

A thesis submitted in partial fulfillment
of the requirements for the degree of
Doctor of Philosophy

The School of Graduate and Postdoctoral Studies
The University of Western Ontario
London, Ontario, Canada

© Tomas Trebicky 2011

THE UNIVERSITY OF WESTERN ONTARIO
School of Graduate and Postdoctoral Studies

CERTIFICATE OF EXAMINATION

Supervisor

Dr. Leo W. M. Lau

Supervisory Committee

Dr. Peter J. Simpson

Dr. Mahi R. Singh

Examiners

Dr. Giovanni Fanchini

Dr. Lyudmila Goncharova

Dr. Paul A. Charpentier

Dr. Dolf Landheer

The thesis by

Tomas Trebicky

entitled:

Hyperthermal H_2 Induced C–H Bond Cleavage: A Novel Approach To Cross-linking Of Organic Molecules

is accepted in partial fulfillment of the
requirements for the degree of
Doctor of Philosophy

Date

Chair of the Thesis Examination Board

Abstract

The development of simple and effective methods of incorporating molecular moieties with desirable properties into new functional materials is one of the ultimate goals of material scientists. The work presented in this thesis demonstrates an easy way to accomplish this using a beam of gaseous H_2, which we call hyperthermal hydrogen induced cross-linking (HHIC). We prove theoretically and experimentally that when the kinetic energy of H_2 is raised to ~20 eV, it becomes a light-mass projectile which is energetic enough to knock hydrogen atoms off of organic molecules, but not other heavier atoms. By developing a reactor to inexpensively generate a high flux of H_2 with the appropriate kinetic energy, we exploit this selective C–H cleavage method to create carbon radicals, which then recombine to yield covalent cross-links. Using this method to cross-link organic moieties of our choice with no change in their desirable properties, we have a) fabricated functional materials with tailor-made mechanical, chemical, and biomedical properties, and b) modified electrical properties of conducting and semiconducting polymers.

Chapter 2 provides an insight into the inception of the HHIC reactor, its operation, and necessary theoretical background of electron cyclotron resonance plasma, gas phase collisions involved in HHIC, and hydrogen abstraction. We also discuss energy distribution of cross-linking projectiles as measured by quadrupole mass spectrometer and Faraday cup detector. We have found that under standard HHIC conditions, the number of hyperthermal projectiles doubles with respect to the number of collision initiating particles, yielding a high-throughput of the HHIC method.

Chapter 3 focuses on the evaluation of the HHIC method in terms of degree of cross-linking, topographical, chemical, and electrical changes, and selectivity towards chemical functional groups. We show that the HHIC method is very gentle in treating chemical functionalities. However, we also show that the HHIC reactor in its current configuration is responsible for exposing sensitive organic semiconducting materials to deep vacuum UV irradiation, damaging their π–π^* conjugated system and negatively effecting their electrical properties.

Chapter 4 extends the study of HHIC by exploring its capability of grafting organic moieties onto polymer surfaces disallowed under normal conditions.

Keywords

Cross-linking – curing –·ECR plasma – hot-atom chemistry – green technology – laminates – organic molecules – polymers – polythiophene – polyacrylic acid – surface grafting – polyolefins – surface modification – surface polymerization

Co-Authorship Statement

The body of this Thesis also consists of two papers, which were co-authored with various collaborators.

Ab initio molecular dynamics simulations presented in Chapter 2 were carried out by Dr. Fan. The Monte Carlo model was proposed by Dr. Paliy and implemented in C++ by myself along with running the simulations.

Chapter 3 is based on a draft of a paper written by me and Dr. Lau, where I was responsible for designing and conducting of experiments, and writing of the manuscript.

Chapter 4 is based on a paper where I am the second author and was responsible for all HHIC related experiments in terms of conducting the experiments as well as writing the relevant parts of the paper.

Acknowledgments

I am pleased to acknowledge a number of people without whom the completion of my Thesis would not have been possible:

First and foremost, I am grateful to Leo Lau, who took care of me after my previous supervisor Igor Bello retired from the university, who guided me through every step of the way, who challenged me and put great trust in me. I learned a tremendous amount from his deep physical and chemical knowledge. I also thank you for your support and advice over all those years.

Igor Bello for giving me the opportunity to work with such great people in this amazing environment.

Mary Jane Walzak, Mark Biesinger, and Heng-Yong Nie for their help in overcoming numerous experimental and theoretical hurdles at any time and any place.

Maxim Paliy and Patrick Crewdson for their help in discussing various aspects of physics and chemistry involved in HHIC.

Suzanne Hicks for doing a great job, and supplying me with countless pens, which mysteriously kept disappearing from around me.

SSW and its staff for allowing me to use their equipment whenever I liked, for keeping the instruments up and running when it was the most crucial, and last but definitely not least for being very friendly and welcoming.

Brian Dalrymple and Frank Van Sas for making my dreams come true… literally… in case of machining of various vacuum components from my crazy sketches.

Doug Hie for lending me electronic equipment and fixing it without any delay.

Phin Perquin for keeping me supplied with necessary tools and equipment.

The Nanofab crew for letting me use their facility and for offering good advice whenever I needed it.

The brave servicemen, past and present, for keeping us safe so that we can lie in our books and enjoy the life.

The pioneers of hockey for inventing such a thrilling and dynamic sport.

Barbora, my wife, my mom Mamut, my dad, and both our families, for gentle encouragement, unconditional support, love, and for always believing in me. I love you all very dearly.

Table of Contents

CERTIFICATE OF EXAMINATION ii

Abstract iii

Co-Authorship Statement v

Acknowledgments vi

Table of Contents viii

List of Tables xi

List of Figures xii

List of Appendices xix

Chapter 1 1

1 Introduction 1

Chapter 2 13

2 Hyperthermal Hydrogen Induced Cross-linking 13

2.1 Construction 13

2.1.1 ECR plasma 16

2.1.2 Reaction chamber 18

2.1.3 Vacuum system 20

2.1.4 Analytical chamber 23

2.2 Theoretical framework 24

2.2.1 Electron cyclotron resonance plasma 25

2.2.2 Cascade of collisions 39

2.2.3 Simulation of the cascade of collisions 46

2.2.4 Hydrogen abstraction 49

2.3 Energy measurements 59

2.3.1 Energy measurements using quadrupole mass spectrometer 60
2.3.2 Energy measurements using Faraday cup 68
Chapter 3 83
3 Evaluation of HHIC method 83
3.1 Introduction 83
3.2 Dotriacontane 84
3.2.1 Experimental setup 85
3.2.2 Results and discussion 87
3.2.3 Conclusion 90
3.3 Poly(3-hexylthiophene) 90
3.3.1 Experimental setup 91
3.3.2 Results and discussion 94
3.3.3 Conclusion 102
3.4 Poly(acrylic acid) 103
3.4.1 Experimental setup 103
3.4.2 Results and discussion 105
3.4.3 Conclusion 106
Chapter 4 111
4 Functional polymer laminates 111
4.1 Introduction 111
4.2 Experimental setup 114
4.3 Results and discussion 116
4.4 Conclusion 125
Chapter 5 129
5 Summary and outlook 129

Appendices 133

Curriculum Vitae 146

List of Tables

Table 1. Comparison of thickness retention ratios for hydrogen and helium driven HHIC. ...89

Table 2. Variation in P3HT film thickness in nm. 95

Table 3. Resistance ratios for HHIC treated P3HT films. 101

Table 4. XPS results showing area percentages for components of C 1s and O 1s peaks. 124

Table 5. Raw data for Figure 18. 134

Table 6. Raw data for Figure 19. 135

Table 7. Raw data for Figure 26. 135

Table 8. Raw data for Figure 30. 141

Table 9. Raw data for Figure 32. 142

Table 10. Raw data for Figure 33. 143

Table 11. Raw data for Figure 34. 145

Table 12. Raw data for Figure 35a. 145

Table 13. Raw data for Figure 35b. 145

List of Figures

Figure 1. Photograph of the HHIC reactor. 14

Figure 2. Overview of vacuum fittings used on the HHIC reactor: a) ConFlat (CF), knife-edge; b) a Swagelok tube fitting before (left) and after (right) tightening (image sources: a) http://www.surfacefinishing.com/article.mvc/ISA-Swagelok-introduces-new-tube-fitting-0001; b) http://aquisemprende.com/modules/com_sobi2/?swagelok-tube-fitting-980) 15

Figure 3. Construction schematic diagram of the HHIC system. Shown are 4 parts of the system: (a) ECR plasma generation chamber and components, (b) reaction chamber hosting the specimen, (c) analytical chamber separated by a plate with a small hole of radius 0.5 mm, (d) vacuum components. 16

Figure 4. Grounding electrode with a hole size of 1.2 mm and a pitch size of 1.9 mm. 18

Figure 5. Detailed and expanded views of the reaction and plasma vacuum chambers. The mesh electrodes are made from a thin stain-less steel wire of diameter 100 μm and the pitch of 5 mm. The overall length of the drift zone is 45 cm and the diameter is 15.24 cm. The length of the ceramic stand-offs is 2.54 cm. 19

Figure 6. Two types of shutters for controlling time of exposure of samples to HHIC: a) single-axle solid shutter, b) blade blinds. 20

Figure 7. Cross-sections of a set of two vacuum pumps: a) rotary vane pump; b) turbomolecular pump (source http://www4.nau.edu/microanalysis/Microprobe-SEM/Instrumentation.html). 21

Figure 8. Cross-sections of a set of three pressure gauges: a) Pirani; b) cold cathode, inverted magnetron; c) capacitance manometer, Baratron (Courtesy of Kurt J. Lesker Company). 22

Figure 9. SIM300P probe construction schematics (Courtesy of Hiden Analytical Inc.). 24

Figure 10. Separation of plasma body into bulk plasma and sheath regions. The sheath regions show number densities $n_i \gg n_e$ with strong electric field. The bulk plasma is approximated as an electric field-free region with $n_i = n_e$ and plasma potential V_p. 29

Figure 11. Simplified emission spectrum of hydrogen atom. Spectral lines in the visible spectrum are shown in the black window. 31

Figure 12. Schematic diagram of coupling of the microwave energy to plasma. 33

Figure 13. Distribution of the electric field in two different transverse modes of propagation of electromagnetic waves. A cross-section of a rectangular waveguide carrying a TE_{10} mode in shown at the top. A cross-section of a circular waveguide carrying a TM_{01} mode is shown at the bottom. 35

Figure 14. Mode converter transforming the TE_{10} mode onto the TM_{01} mode (note: the TM_{01} mode cannot exist in a rectangular waveguide). 36

Figure 15. Schematic diagram of the HHIC reactor showing the generation of hydrogen ions, their extraction, and collisions with background gas molecules, as well as reflection of charged particles above the sample stage. 39

Figure 16. Hard-sphere scattering. A particle of radius r_2 impinges on an infinitely massive particle of radius r_1 and scatters at an angle θ. The impact parameter b is the distance between the centres as projected onto the axis perpendicular to the axis of incidence. 42

Figure 17. Simplified schematic diagram of an elastic collision of two particles. The impact parameter b is not shown (see Figure 16). 44

Figure 18. Modeling of HHIC production: (left) the number of H_2 projectiles per incident particle having energies higher than 5, 19, and 40 eV, the dashed line denotes the typical operational pressure of 0.8 mTorr; (b) Monte Carlo simulations of time evolution of a gas-phase (293 K, 1 mTorr) cascade of collisions in a drift zone (blue tube) initiated by a 100 eV H+ projectile. The H_2 projectiles with energies $E > 19$ eV are shown in red, those with $E < 19$ eV are shown in

green, and the background gas particles not participating in the collision cascade are not shown. 47

Figure 19. Number of H_2 projectiles per incident particle having sufficient energy to break C–H bonds (> 19 eV). The parameter is the energy of H+ initiators as given by the accelerating potential. 48

Figure 20. Schematic diagram of hydrogen abstraction as induced by hyperthermal H_2. (a) H_2 hitting H of a C–H bond, possessing enough kinetic energy to break the bond and knocking H off of the molecule; (b) H_2 hitting C of a C–H bond, ineffectively transferring some of its kinetic energy to the methane molecule and bouncing off of it. 50

Figure 21. Computational results of ab initio MD showing cleavage of the C–H bond of C_2H_6 by 19 eV H_2 with the molecular axis of H_2 perpendicular to the axis of the H–C bond of C_2H_6 (note: the respective views of H#4 and H#7 of C_2H_6 are blocked by H#5 and H#8). The plot on the right shows the evolution of potential energy of the C_2H_6 molecule. The C_2H_6 molecule eventually becomes C_2H_5 52

Figure 22. Computational results of ab initio MD of 39 eV H_2 arriving with its molecular axis along the $C_{\#1}$–$C_{\#2}$ bond axis of C_2H_6 and with $H_{\#9}$ of H_2 hitting $C_{\#2}$ of C_2H_6 (the respective views of $H_{\#4}$ and $H_{\#7}$ are blocked by $H_{\#5}$ and $H_{\#8}$). After the collision, the H_2 is scattered with a loss of about 18 eV in kinetic energy (44% energy transfer) and a very small gain in vibrational and rotational energy. The C_2H_6 suffers no bond cleavage, with about 9 eV gain in kinetic energy and some gain in rotational and vibrational energy. The plot on the right shows the evolution of potential energy of the C_2H_6 molecule. 53

Figure 23. Schematic diagram of a quadrupole mass analyzer. Ion optics is responsible for ionizing (if required), energy filtering (if equipped), and transporting focused ions into the quadrupole rod system. Rods would ideally have a shape of hyperbolas (facing the mid-axis), but because it is difficult to machine, simple cylinders are generally used. Ion detectors usually make use of a Faraday cup or a secondary electron multiplier detector. 61

Figure 24. Schematic diagram of SIM300P analyzer including voltage references. 63

Figure 25. Cross-section of the RGA modification to the HHIC reactor. 64

Figure 26. Energy distribution of neutral hydrogen molecules as measured by RGA for a) constant $V_{acc} = -50$ V and four pressures (left), and b) constant $p = 0.8$ mTorr and three accelerating voltages. 66

Figure 27. Faraday cup detector with a set of ion lenses and a pair of mesh electrodes for energy discrimination. Below is the typical potential profile. 69

Figure 28. SIMION® simulation of the behaviour of the FC detector for ions with incident energies of 20 (top) and 30 (bottom) eV and the potential barrier V_r of 20 V. The FC is modeled without the bevelled insert because it does not affect the results and is difficult to model in a system of cylindrical symmetry. 71

Figure 29. Three positions of the FC detector during measurements: at the centre of the drift zone at 0° and 45°, and at the side of the drift zone out of line-of-sight of plasma at 45° (angles relative to the vertical). 73

Figure 30. Energy distributions of positive hydrogen ions (left) and the corresponding FC currents (right) as measured for $V_{acc} = 0$ V and three pressures at the centre of the drift zone and 0°. 74

Figure 31. Change of ion energy distribution in the plane of a sample with the sample-level coil current i_m (Matsuoka et al., 1988b). The case of $i_m = 0$ A should be considered. 75

Figure 32. Energy distributions of positive hydrogen ions (left) and the corresponding FC currents (right) as measured for $V_{acc} = -50$ V and three pressures at the centre of the drift zone and 0°. 76

Figure 33. Energy distributions of positive hydrogen ions (left) and the corresponding FC currents (right) as measured at the centre of the drift zone and two angles (0° and 45°), and an edge of the drift zone at 45°, for $V_{acc} = -50$ V and pressure 0.8 mTorr. 77

Figure 34. Effectiveness of C–H cleavage of n-$C_{32}H_{66}$ as a function of V_{acc} (initial KE of hydrogen initiators), showing a drastic reduction of cross-linking efficiency for projectiles

having insufficient energy to cleave C–H bonds. Shown is the retention of sample thickness after HHIC and after washing. 88

Figure 35. Further studies of efficiency of the HHIC method. Thickness ratios for constant $V_{acc} = 200$ eV, and a) $I_{acc} = 10$ mA and b) $I_{acc} = 20$ mA. 89

Figure 36. Layout of a four-probe measurement device with a diagram of current-voltage sensing mechanism. 93

Figure 37. AFM topography images of P3HT thin film on silicon substrate for a) pristine sample, b) HHIC treated sample, and c) HHIC treated and washed. 95

Figure 38. AFM topography images of P3HT thin film after HHIC and washing. HHIC bombardment times were: a) 5 s, b) 15 s, and c) 25 s. 96

Figure 39. High-resolution XPS spectra of C 1s (top row) and S 2p (bottom row) regions for P3HT film: a) pristine, b) HHIC treated, and c) HHIC treated and washed. 97

Figure 40. XPS survey spectra of a) pristine and b) HHIC treated P3HT film showing elemental composition of oxygen, carbon, and sulfur. 98

Figure 41. UV-Vis optical absorbance for 10 nm thick P3HT layer exposed to HHIC at a) 10 mA, and b) 100 mA showing a blue shift. 99

Figure 42. Retention of lost optical absorbance as measured by UV-Visible spectroscopy for 15 nm P3HT film HHIC treated at a) 10 mA and b) 100 mA extraction current, and 35 nm P3HT film HHIC treated at c) 10 mA and d) 100 mA extraction current. 100

Figure 43. ToF-SIMS depth-profile data of a sandwich structure comprising (in order from top to bottom) cross-linked poly(methyl methacrylate) (green line), a) cross-linked, and b) uncross-linked P3HT (red line), and poly(ethylene terephthalate) (blue line). 102

Figure 44. XPS high-resolution C 1s spectra of pristine and HHIC treated PAA showing over 95% retention of COOH functionality. 105

Figure 45. ToF-SIMS elemental maps of patterned PAA through HHIC treatment. 106

Figure 46. Schematic diagram of a) the preparation of laminates using HHIC and b) chemical transformations of the PVAc layer. 113

Figure 47. AFM topography images of BOPP surface (left) and Bu/BOPP surface after HHIC (right). 117

Figure 48. ATR-FTIR spectra showing changes in chemical functionalities at surface layers: a) cross-linked Bu/BOPP; b) cross-linked PVAc/Bu/BOPP; c) hydrolysis gave PVA/Bu/BOPP; d) treatment of PVA/Bu/BOPP with acetyl chloride restored ester functional groups. 118

Figure 49. High-resolution XPS spectra of the C 1s region showing C–C,C–H, beta shifted C^{β}–C,C^{β}–H, C–O-C=O, C=O, and C–O–C=O species for a) cross-linked Bu/BOPP surface, b) cross-linked PVAc/Bu/BOPP surface, c) NaOH treated PVAc/Bu/BOPP surface showing PVA formation, d) re-esterified surface after acetyl chloride (AcCl) treatment of PVA/Bu/BOPP. The red line represents the actual spectrum, the thin black line represents GL fitting curve, and the dashed black line represents a sum of individual fitting curves. 119

Figure 50. Receding contact angle measurements of polymer surfaces for a) BOPP, b) Bu/BOPP, c) PVAc/Bu/BOPP, d) PVA/Bu/BOPP, e) PVA/Bu/BOPP aged 3 days, and f) PVA/Bu/BOPP treated with AcCl to give back PVAc/Bu/BOPP. 120

Figure 51. High-resolution XPS spectra of the O 1s region showing C–O–C=O, C–O–C=O, and H_2O species for a) cross-linked PVAc/Bu/BOPP surface, and b) NaOH treated PVAc/Bu/BOPP surface showing PVA formation. 121

Figure 52. High-resolution XPS control spectra of the C 1s region showing C–C,C–H species for a) cross-linked Bu/BOPP surface, b) washed uncross-linked PVAc/Bu/BOPP surface, c) AcCl treated cross-linked Bu/BOPP surface, d) NaOH treated cross-linked Bu/BOPP surface, e) AcCl and NaOH treated cross-linked BOPP surface, and f) NaOH treated cross-linked BOPP surface. 122

Figure 53. High resolution XPS spectra of the C 1s region showing C–C,C–H, beta shifted C^{β}–C,C^{β}–H, C-O-C=O, C=O, and C-O-C=O species of: a) cross-linked PVAc/Bu/BOPP and b) PVAc standard surface. 125

Figure 54. Ion extraction configuration as proposed to minimize the intensity of escaping plasma radiation. 130

Figure 55. Modification of the HHIC reactor to measure the energy distribution of hyperthermal neutral projectiles using a quadrupole mass spectrometer. 131

Figure 56. Modification of the HHIC reactor operation for use in industrial environment. ..132

List of Appendices

Appendix A: Reactor operation 133

Appendix B: Raw data 134

Chapter 1

1 Introduction

Organic materials, such as simple molecules, shorter or longer chains, containing saturated hydrocarbon segments often have specific chemical and physical properties based on their structure and environment. These may often be chemically inert and function as building blocks of backbones or spacers (Pugh et al., 1997). In some cases and applications the initial properties may not be sufficient and further enhancement is necessary. If the chemical and physical strength or stability is the key, an inter-chain cross-linking is a way to improvement. If one needs to join or functionalize organic compounds, or graft chemical functionalities onto inert or other surfaces, cross-linking is again necessary.

Cross-linking is a process of chemically joining molecules by covalent bonds. This is a common and important process both in nature and in industry, to build large and function-specific molecules from small and simple ones. In the polymer industry, monomers are joined to macromolecular chains, which can also be further cross-linked into polymeric networks. In the simplest example, a CH_4 molecule can be converted to a CH_3 radical by the cleavage of one of its C–H bonds, and two CH_3 radicals can then recombine to form C_2H_6. Repeating the cleavage of C–H and recombination of carbon radicals can yield a large inter-chained (cross-linked) hydrocarbon network, possibly in the form of a thin film.

Currently, there are three basic approaches available for cross-linking and functionalizing of hydrocarbon chains (Garbassi et al., 1998): ultraviolet irradiation (see Choi et al., 1997; Dontula et al., 1997; Okamoto et al., 1997; Dontula et al., 1998; Shirai et al., 2003; Skurat, 2003; Weilnboeck et al., 2010; Wu et al., 2011), plasma exposure (Lee et al., 1998; Hegemann et al., 2003; Hwang et al., 2004; Forch et al., 2005; Tajima et al., 2007), and other radical-mediated reactions (Jacobs, 2002; Benetti et al., 2011; Hao et al., 2011; Horak et al., 2011; Park et al., 2011; Tria et al., 2011). Although all of them will ultimately achieve their goal, each possesses specifics that disqualify them in certain

situations. A common drawback is their insensitivity to most chemical functional groups that will inevitably be altered or destroyed. In terms of grafting tailor-made chemical functionalities onto various surfaces, surface-initiated polymerization methods (Edmondson et al., 2004) including atom transfer radical polymerization (Patten et al., 1996) are certainly applicable after a hydrocarbon segment has been properly pre-functionalized. Some studies also explore the suitability of low-temperature scanning tunnelling microscopy to selectively cleave hydrogen (Katano et al., 2007), but such methods can only be applied to small areas at very high resolution and generally take a long time to complete. However, the above processes typically involve multiple steps, make use of toxic chemicals, or are energetically inefficient, and require a great deal of time (Edmondson et al., 2004). The presented work revolves around a novel and unconventional, simple and fast, efficient method to overcome the deficiencies of the other processes. It utilizes molecular hydrogen with a kinetic energy appropriately higher than the C–H bond energy to preferentially cleave C–H bonds of the hydrocarbon segments without altering or damaging other chemical functionalities.

In the conventional cross-linking reactions, precursor molecules containing chemically reactive units to facilitate cross-linking are synthesized and placed together. Another reactive reagent is added to activate the cross-linking reaction; the activation is typically enacted by bond-cleavage and radical formation. Heat or another energy source (e.g., ultraviolet irradiation) is typically required to break bonds. To reduce the energy barrier for this bond cleavage and to increase the reaction rate, a catalyst is normally required. In addition, other chemical additives are often used to moderate the reaction rate, and to terminate the reaction after a certain degree of cross-linking is accomplished. Many of these reactive chemical reagents are toxic and environmentally harmful. As such, there is a desire to develop a “green” route of cross-linking so that the use of these chemical reagents can be reduced or altogether eliminated.

To develop such a “green” and practical route of cross-linking, it is relevant to examine the processes for cleaving C–H in an organic precursor molecule. Rupturing and removing a hydrogen atom from a hydrogen-containing molecule is commonly referred as hydrogen abstraction in chemistry. A number of reactants can be used in hydrogen

abstraction. Common reactants include hydrogen atom, halogen atom, hydroxyl radical, and other radical species. Although the reactants are reactive, activation energy is still commonly required for hydrogen abstraction and some reactions thus require adequate thermal energy (see Zavitsas, 1998). Among these reactants, the hydrogen atom is particularly attractive because it is not toxic and its generation is relatively easy. The hydrogen abstraction reaction of using atomic hydrogen to break a C–H bond of an alkane molecule is typically exothermal or energy-neutral but has a transition energy barrier of about 0.5 eV. As such, the reaction rate is relatively low at room temperature. Indeed, for a gas phase reaction of $H + CH_4 \rightarrow H_2 + \dot{C}H_3$ with a constant supply of both reactants at a partial pressure of 1×10^{-3} Torr at room temperature, the generation of $\dot{C}H_3$ to a partial pressure of 10^{-3} Torr, in the absence of any side reactions, will take about one month. By raising the reaction temperature to 300°C, the same result can be obtained in about 0.3 second. Although similar examples of using thermal energy to drive chemical reactions forward are indeed widely used in industry, this heat-driven approach is not applicable to those reaction systems in which heat causes other undesirable side reactions. For polymer manufacturing, heating the polymer above its glass transition temperature will cause undesirable deformation. Novel and economical reaction routes for selective C–H bond cleavage with a high throughput and without any heat requirement are thus attractive and desirable.

In another widely adopted method of cross-linking small organic precursor molecules to a polymeric film, the organic precursor molecules are fed into a gaseous plasma powered by a direct-current (DC), radio-frequency (RF) or microwave (MW) energy source. The science of technology of plasma polymerization has been adequately reviewed by pioneers in the field such as Yasuda, Biederman, and Fridman. It is commonly recognized that even when pure organic precursor molecules are fed into plasma, the plasma chemistry is complex and many competing bond-breaking processes are active in the plasma. In essence, when plasma is ignited in a gas, some atoms and molecules in the gas are ionized to generate a large number of electrons and ions. Typically these electrons can possess an average energy of a few electron volts and a broad energy distribution. Expressed in an equivalent value in temperature, these electrons can reach ~10^5 K. In the

plasma, they diffuse much more quickly than ions and their frequent collisions with the atoms and molecules in the plasma lead to excitation, ionization, and bond dissociation. The relaxation of some of these excited species can emit light including ultraviolet light, which can cause secondary excitation, ionization, and bond dissociation. Hence, although a polymer film can be practically formed using plasma polymerization technique, it is difficult to control the resultant film to match a specific chemical composition such as having a film with only one type of chemical functional group (e.g., COOH) in a certain desirable concentration (e.g., one COOH group per three carbon atoms such as that in polyacrylic acid). In fact, Yasuda wrote, "most organic compounds with oxygen-containing groups such as –COOH, –CO–, –OCO–, –OH, and –O–, are generally reluctant to form a polymer, and the plasma polymers rarely contain the original oxygen-containing groups" (see Yasuda, 1985, p.112-113).

Several special plasma polymerization methods have been developed to address these limitations of the general plasma polymerization methods. For example, the technique of pulsed plasma polymerization has been developed to harness the complex processes of excitation, ionization, and dissociation in the plasma by supplying the plasma energy to the reactant gas in a train of pulses with controls of the duration, frequency and power of the pulses. The concept and applications of this technique have been explained by Friedrich et al. In their work, monomer precursor molecules having a C=C bond such as acrylic acid (H_2C=CHCOOH) receive a short pulse of plasma energy and undergo excitation, ionization and dissociation. Although undesirable reactions leading to the loss of the –COOH functional groups will inevitably occur, most of these undesirable reactions cease during the pulse-off-cycle. However, the polymerization chain reaction in cross-linking acrylic acid molecules persists even when the plasma pulse is off. In an optimized pulsed plasma polymerization process, when the cross-linking chain reaction runs out of stream, the plasma pulse is applied to prime the chain reaction again. For example, Friedrich et al. have demonstrated that up to 73% of the –COOH in acrylic acid can be retained in a polymer film formed by this pulsed plasma polymerization method. Since the loss of useful functional group and the formation of undesirable functional groups can still occur when the plasma pulse is on, an alternative technique to eliminate these problems is still desirable.

In the research and development of new reaction routes, scientists have discovered that the kinetic energy of a reactant can be an important reaction attribute. It can be used to drive a chemical reaction which otherwise relies totally on the thermal energy supplied to the reaction system and the chemical potentials of reactive chemical reagents. The best fundamental evidence can be found in most scientific articles on molecular beam research in the literature (see for example Fluendy et al., 1973). In this research, a beam of atoms or molecules having a specific kinetic energy and internal energy is directed to a target. The energy exchange and resultant chemical reactions are examined. Such experiments are, however, technically demanding and economically expensive. In a typical molecular beam experiment, kinetic energy is added to the atoms or molecules when they are adiabatically expanded with an inert gas through a small nozzle. The velocity of the atoms or molecules can increase to supersonic speed. However, this technique is not suitable for light species, since it is not possible to achieve suitable energies. Although it is possible to speed up a heavy hydrogen-containing molecules such as HI and split it with a laser beam for the formation of hyperthermal atomic hydrogen, this is certainly not a practical method to practice C–H bond cleavage in industry as the throughput is very low.

The kinetic energies of atoms or molecules can also be increased by ionizing them and then accelerating them using an electrostatic ion acceleration process. These accelerated ions can be used to bombard a target in an “ion bombardment” process. Many industrial processes indeed use ion bombardment to reduce the reliance of synthetic reactions on thermal energy and to promote reactions via non-thermal equilibrium pathways (see for example Auciello et al., 1984). In practice, ion bombardment of an electrically insulating surface is not practical because of surface charging. Although many analytical instruments such as ion microscopes circumvent such surface charging problems by flooding the ion bombarded area with low energy electrons, the concurrent supplies of both energetic ions and electrons with precise controls in energy and dosage to a large irradiation area for practical industrial manufacturing are technically challenging and expensive.

Recently Lau and coworkers have shown that bombarding an organic molecule with hyperthermal protons can preferentially break C–H bonds without breaking other bonds. The pioneering work by Kwok and Lau describes for the first time a method for selectively removing hydrogen from molecules using hyperthermal protons (US Patent 20030165635). The feasibility of this method was also shown by Xi et al. based on a study of the hyperthermal proton bombardment effects on self-assembled monolayers of dodecanethiol on Au(111), by Choi et al. on the example of fabrication of cross-linked multi-walled carbon nanotube coatings with improved adhesion and intrinsic strength by a two-step synthesis, by Lau et al. exploring the chemistry with a "tiny hammer" and cross-linking organic semiconducting molecules, by Xi et al. looking at the effects of hyperthermal proton bombardment on alkanethiol self-assembled monolayer on Au(111), by Zheng et al. studying the selectivity of proton bombardment by cleaving C-H but not COO-H bonds to synthesize tailor-made molecular films, by Zheng et al. exploring a new cross-linking route via the unusual collision kinematics of hyperthermal protons in unsaturated hydrocarbon— poly(trans-isoprene), by Xu et al. on surface modification of polystyrene by a low energy hydrogen ion beam, and by Zheng et al. studying ultrathin polymer film formation by collision-induced cross-linking of adsorbed organic molecules with hyperthermal protons.

The novelty of this approach lies in the exploitation of the unusual kinematics when a hyperthermal proton strikes an organic molecule adsorbed on a conductive solid substrate. In this bombardment process, the incoming proton will first be neutralized by the conductive substrate when it is still >0.5 nm above the surface. The neutral atomic hydrogen projectile carrying a few eV in kinetic energy continues to approach the target organic molecule and enters first to the attractive chemical potential region and forms a transient molecule with the target. The kinetic energy then drives the projectile into the repulsive potential region and finally the projectile uses up its kinetic energy. If the projectile and target are merely two hard spheres, after the closest encounter they will fly apart and the maximum energy transfer is determined by the two masses with the formula: $4m_p m_t/(m_p + m_t)^2$. Hence, a projectile of an atomic mass unit of one can transfer its kinetic energy very effectively to a target of an atomic mass unit of one

(hydrogen atom) but the maximum kinematic energy transfer drastically drops to ~28% if the target has an atomic mass unit of twelve (carbon atom). This difference in kinematic energy transfer can be exploited, in principle, to preferentially break C–H bonds because the typical dissociation energy of C–H and other sigma bonds of an organic molecule is 4–5 eV. Indeed, Lau and co-workers have demonstrated the feasibility of this concept by using protons of ~20 eV to break C–H bonds without breaking other bonds in a variety of organic molecules.

By condensing polyacrylic acid as the precursor molecules on a silicon wafer surface, they have demonstrated the cross-linking of these molecules into a stable molecular layer with retention of more than 95% of the –COOH group by their proton bombardment method. In all their published experimental data, protons are used because protons can be attracted from hydrogen plasma and the proton energy can be controlled quite precisely with the common techniques of ion optics. They have also confirmed the theoretical validity of the concept by ab initio molecular dynamics computations for the collisions of a proton with a simple hydrocarbon molecule under different collision trajectory conditions. Their published results are informative in laying the foundation of using kinematic energy transfer to break C–H bonds, but the approach of proton bombardment suffers the same surface charging problems of all ion bombardment techniques. It is also impractical for industrial manufacturing of polymeric products because of the small size of the beam.

Therefore, it would be very advantageous to provide a method of selectively breaking C–H and/or Si–H bonds, which can be used with any substrate and which avoids breaking other molecular bonds.

The use of hyperthermal H_2 as the projectile of choice in our experiments is novel because traditionally helium and other inert gases with a typical kinetic energy of 1–100 keV are used in direct recoiling spectrometry to knock off atoms indiscriminatingly from a sample for chemical compositional analysis (Rabalais, 1990). For example, Rodriguez et al. used 4–6 keV Ar+ as a projectile to recoil H, C, S, Ga, and As atoms from the target of alkyl-thiol on Au(111) in order to reveal the adsorption dynamics of the system

(Rodriguez et al., 2007). In comparison, our employment of H_2 as the projectile of choice is a very specific and practical niche in the general discipline of collision-induced dissociation, in the context of effective and selective cleavage of C–H bonds.

While the proposed chemistry is simple in nature, to my knowledge its applicability has never been explored. The first technical difficulty is to estimate and harness the kinetic energy of H_2 for selective C–H cleavage, an energy which is likely less than 20 eV, as suggested by the computational results as presented in Chapter 2. The second problem is to generate a high flux of H_2 at this hyperthermal energy regime because the known method of photodissociation of a supersonic molecular beam of hydrogen halide does not satisfy the energy and flux requirements (Scoles, 1988; Levine, 2005) and the method of neutralizing a hyperthermal H_2^+ beam (Rechtien et al., 1993) is too expensive and does not produce a high enough flux.

The proposed new reaction mechanism of this work is similar to, yet different from, those collision-induced dissociation mechanisms discovered by Ceyer in 1990 regarding breaking C–H bonds of CH_4 physisorbed on Ni(111) (Beckerle et al., 1990). Ceyer showed that when CH_4 physisorbed on Ni(111) is hit by a hyperthermal argon atom, the projectile transfers some energy to CH_4 and is backscattered by a mechanism similar to the binary hard-sphere collision. The subsequent forward motion of the CH_4 is enough to induce the conversion from physisorption to dissociative chemisorption. She also showed that by replacing argon with krypton, which is much heavier than CH_4, the krypton atom after collision is not backscattered but instead moves forward with CH_4 and in turn hammers CH_4 into the Ni substrate causing dissociative chemisorption. Although both cases also yield C–H cleavage, they are different from the new method presented in this work in that her mechanism of C–H cleavage is not a direct recoiling of a hydrogen target by a projectile.

After conceiving and computationally validating the idea of using hyperthermal H_2 to facilitate selective C–H cleavage, we developed a working technology to generate a high flux of hyperthermal H_2. Although the computational results shown in Chapter 2 suggest a threshold energy of 19 eV for cleaving C–H of C_2H_6 by molecular hydrogen, the

threshold is expected to drop when C–H is actually present in a saturated hydrocarbon segment of a solid because as the carbon atom of the C–H bond is fixed more rigidly than that on an isolated C_2H_6 molecule, the energy loss of the projectile to the "carbon substrate" is reduced.

The work is divided into three major parts. Part 1 (Chapter 2) shows the inception of an HHIC reactor, its operation, and necessary theoretical background of electron cyclotron resonance plasma, gas phase collisions involved in HHIC, and hydrogen abstraction. We also discuss energy distribution of cross-linking projectiles as measured by quadrupole mass spectrometer and Faraday cup detector. Part 2 (Chapter 3) focuses on evaluation of the HHIC method in terms of degree of cross-linking, topographical, chemical, and electrical changes, and selectivity towards chemical functional groups. Part 3 (Chapter 4) extends the study of HHIC by exploring its capability of grafting organic moieties onto polymer surfaces.

References

Auciello, O. and Kelly, R.: 1984, *Ion bombardment modification of surfaces : fundamentals and applications*, Published by Elsevier Science Publishers, ISBN 0444423656

Beckerle, J. D., Johnson, A. D. and Ceyer, S. T.: 1990, *Journal of Chemical Physics* **93**, 4047-4065

Benetti, E. M., Acikgoz, C., Sui, X. F., Vratzov, B., et al.: 2011, *Advanced Functional Materials* **21**, 2088-2095

Biederman, H.: 2004, *Plasma polymer films*, Published by Imperial College Press, ISBN 9781860944673

Ceyer, S. T.: 1990, *Science* **249**, 133-139

Choi, C. Y., Zheng, Z., Wong, K. W., Du, Z. L., et al.: 2008, *Applied Physics a-Materials Science & Processing* **91**, 403-406

Choi, Y., Kim, S. K., Chang, K. H. and Lee, M. H.: 1997, *Journal of Applied Electrochemistry* **27**, 1118-1121

Dontula, N., Weitzsacker, C. L., Drzal, L. T. and Radtech: 1998, *Ultraviolet light pretreatment of polymers and polymer composite surfaces for adhesive bonding*, ISBN 1-878664-18-2

Dontula, N., Weitzsacker, C. L., Drzal, L. T. and Soc Plast, E.: 1997, *Surface activation of polymers using ultraviolet light activation*, ISBN 1-56676-553-6

Edmondson, S., Osborne, V. L. and Huck, W. T. S.: 2004, *Chemical Society Reviews* **33**, 14-22

Fluendy, M. A. D. and Lawley, K. P.: 1973, *Chemical applications of molecular beam scattering*, Published by Chapman and Hall distributed in the U.S.A. by Halsted Press, New York, ISBN 0412118106

Forch, R., Zhang, Z. H. and Knoll, W.: 2005, *Plasma Processes and Polymers* **2**, 351-372

Fridman, A. A.: 2008, *Plasma chemistry*, Published by Cambridge University Press, ISBN 9780521847353

Friedrich, J., Mix, R., Kuhn, G., Retzko, I., et al.: 2003, *Composite Interfaces* **10**, 173-223

Garbassi, F., Morra, M. and Occhiello, E.: 1998, *Polymer surfaces :from physics to technology*, Published by Wiley, ISBN 0471971006

Hao, J. X., Wang, F. Q., Dai, X. J., Gong, B. L., et al.: 2011, *Talanta* **85**, 482-487

Hegemann, D., Brunner, H. and Oehr, C.: 2003, *Nuclear Instruments & Methods in Physics Research Section B-Beam Interactions with Materials and Atoms* **208**, 281-286

Horak, D., Shagotova, T., Mitina, N., Trchova, M., et al.: 2011, *Chemistry of Materials* **23**, 2637-2649

Hwang, Y. J., Matthews, S., McCord, M. and Bourham, M.: 2004, *Journal of the Electrochemical Society* **151**, C495-C501

Jacobs, D. C.: 2002, *Annual Review of Physical Chemistry* **53**, 379-407

Katano, S., Kim, Y., Hori, M., Trenary, M., et al.: 2007, *Science* **316**, 1883-1886

Kwok, R. W. M. and Lau, W. M.: 2010, *Method for selectively removing hydrogen from molecules*

Lau, W. M., Zheng, Z., Wang, Y. H., Luo, Y., et al.: 2007, *Canadian Journal of Chemistry-Revue Canadienne De Chimie* **85**, 859-865

Lee, S. H. and Lee, D. C.: 1998, *Thin Solid Films* **325**, 83-86

Levine, R. D.: 2005, *Molecular reaction dynamics*, Published by Cambridge University Press, ISBN 052184276X

Okamoto, T., Ohmori, R., Hayakawa, S., Seo, I., et al.: 1997, *Optical Review* **4**, 516-520

Park, J. T., Koh, J. H., Seo, J. A., Cho, Y. S., et al.: 2011, *Applied Surface Science* **257**, 8301-8306

Patten, T. E., Xia, J. H., Abernathy, T. and Matyjaszewski, K.: 1996, *Science* **272**, 866-868

Pugh, C. and Kiste, A. L.: 1997, *Progress In Polymer Science* **22**, 601-691

Rabalais, J. W.: 1990, *Science* **250**, 521-527

Rechtien, J. H., Harder, R., Hermann, G., Nesbitt, A., et al.: 1993, *Surface Science* **282**, 137-151

Rodriguez, L. M., Gayone, J. E., Sanchez, E. A., Grizzi, O., et al.: 2007, *Journal of the American Chemical Society* **129**, 7807-7813

Scoles, G.: 1988, *Atomic and molecular beam methods*, Published by Oxford University Press, ISBN 0195042808

Shirai, M., Shinozuka, T., Tsunooka, M. and Itani, T.: 2003, *Japanese Journal of Applied Physics Part 1-Regular Papers Short Notes & Review Papers* **42**, 3900-3904

Skurat, V.: 2003, *Nuclear Instruments & Methods in Physics Research Section B-Beam Interactions with Materials and Atoms* **208**, 27-34

Tajima, S. and Komvopoulos, K.: 2007, *Journal of Applied Physics* **101**,

Tria, M. C. R. and Advincula, R. C.: 2011, *Macromolecular Rapid Communications* **32**, 966-971

Weilnboeck, F., Bruce, R. L., Engelmann, S., Oehrlein, G. S., et al.: 2010, *Journal of Vacuum Science & Technology B* **28**, 993-1004

Wu, C. M., Su, S. H., Wang, H. T., Yokoyama, M., et al.: 2011, *Japanese Journal of Applied Physics* **50**

Xi, L., Zheng, Z., Lam, N. S., Grizzi, O., et al.: 2007, *Applied Surface Science* **254**, 113-115

Xi, L., Zheng, Z., Lam, N. S., Nie, H. Y., et al.: 2008, *Journal of Physical Chemistry C* **112**, 12111-12115

Xu, X. D., Kwok, R. W. M. and Lau, W. M.: 2006, *Thin Solid Films* **514**, 182-187

Yasuda, H.: 1985, *Plasma polymerization*, Published by Academic Press, ISBN 0127687602

Zavitsas, A. A.: 1998, *Journal of the American Chemical Society* **120**, 6578-6586

Zheng, Z., Kwok, W. M. and Lau, W. M.: 2006, *Chemical Communications* 3122-3124

Zheng, Z., Wong, K. W., Lau, W. C., Kwok, R. W. M., et al.: 2007, *Chemistry-a European Journal* **13**, 3187-3192

Zheng, Z., Xu, X. D., Fan, X. L., Lau, W. M., et al.: 2004, *Journal of the American Chemical Society* **126**, 12336-12342

Chapter 2

2 Hyperthermal Hydrogen Induced Cross-linking

The Hyperthermal Hydrogen Induced Cross-linking (HHIC) method is a physical method for the generation of cross-links in organic compounds. It is a stochastical method where all effects are random in nature, from the initial point of extraction of positive ions, through a cascade of collisions with the background gas molecules, up to the point where the newly created hyperthermal neutrals impinge on a surface, penetrate it and ultimately cleave C–H bonds thus generating radicals available for mutual recombination. The penetration depth changes with the energy of incident particles and is dependent on the inelastic mean free path of the bombarded material. For organic materials, which contain no double bonds or are otherwise unlikely to allow for a long radical lifetime, the cross-linking depth is usually between 10 and 20 nm. Organic systems that contain carbon double bonds with sufficient density, like polyisoprene, were observed to cross-link up to 1 mm in length (Zheng et al., 2006) because of a chain polymerization reaction of the double bonds initiated by HHIC.

This chapter will help the reader to understand the basics of the HHIC method, which has the following general characteristics: It is simple to operate, it has high throughput, large samples can be exposed in a single run, it has relatively low energy consumption, it poses very low demands on reactants (only hydrogen), and it is an environmentally clean process (generates virtually no pollutants). We will start with a design and building of a HHIC reactor in Sections 2.1. A short example of the operation of the HHIC reactor is provided in Appendix A. Necessary theoretical background will be provided in Section 2.2, and the chapter will be concluded with measurements of energy distribution of the workhorse particles: hyperthermal hydrogen molecules.

2.1 Construction

A real photograph of the HHIC reactor is shown in Figure 1 (for comparison, the cylinder on the right is a T-sized cylinder). The system is mounted on a heavy-duty steel flat bed and the skeleton is made of durable aluminum to which all other components are bolted.

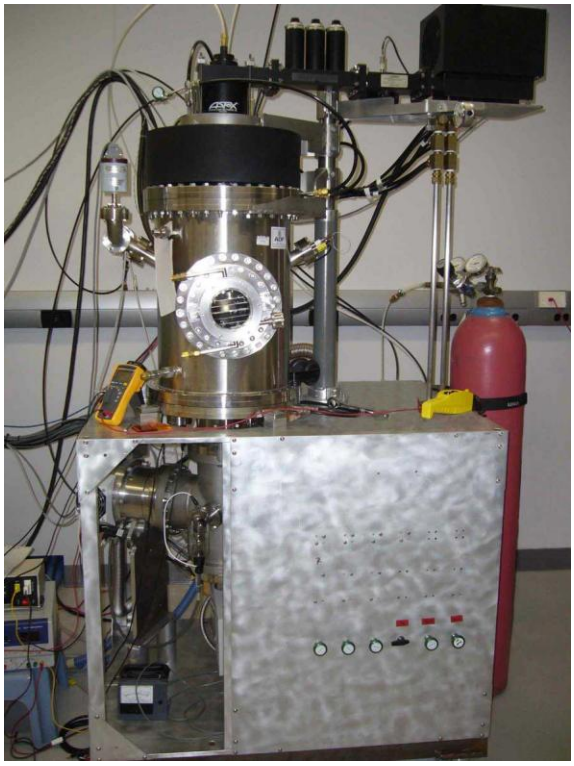

Figure 1. Photograph of the HHIC reactor.

The HHIC system consists of four fundamental blocks. The first one is responsible for the generation of plasma, in our case the principle of operation is based on electron cyclotron resonance maintained by microwave radiation. In the second block, hydrogen ions are extracted through an applied potential and let to collide with background gas molecules generating a high flux of energetic molecular hydrogen. For the purpose of analyzing an energy distribution of particles comprising the generated beam, an analytical chamber is added to the system and placed at the bottom of the reactor. In order to initialize hydrogen plasma at desirable conditions, a low pressure has to be maintained in the reactor with the help of vacuum generating/maintaining components.

Certain components generate undesirable heat during their operation, which needs to be removed. Among those are: solenoid coil, turbo pumps, and microwave dumping compartment. Other parts of the system, such as flanges, can also get hot due to heat conduction and need to be cooled down. For this purpose, a closed circuit water-cooling

system was connected to the reactor. The operational temperature was maintained at 15°C.

Only two types of fittings are used on the vacuum part of the system: ConFlat® (Varian Associates Ltd.), also called knife-edge (Figure 2a), and Swagelok® tube fitting (Figure 2b). To facilitate an ultra-high vacuum (UHV) compliant connection between vacuum components (flanges), copper gaskets are predominantly used as a sealing material. High vacuum grade Viton (elastomer) gaskets are also used where appropriate. Special type of compression fitting is used on the microwave waveguide.

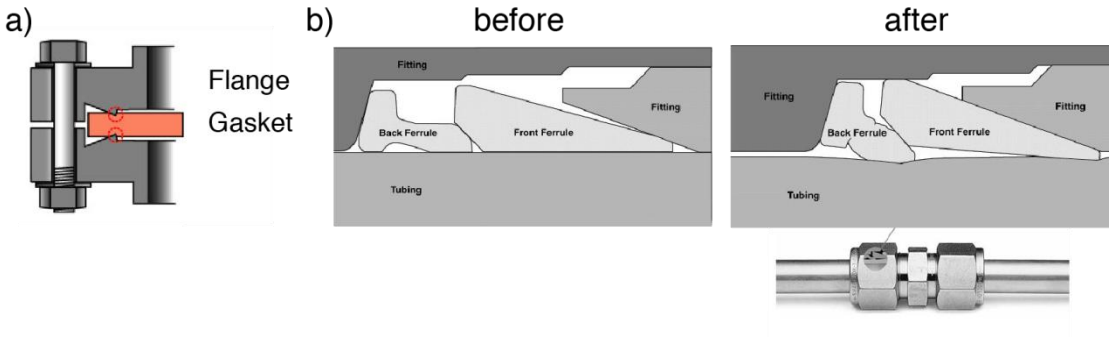

Figure 2. Overview of vacuum fittings used on the HHIC reactor: a) ConFlat (CF), knife-edge; b) a Swagelok tube fitting before (left) and after (right) tightening (image sources: a) http://www.surfacefinishing.com/article.mvc/ISA-Swagelok-introduces-new-tube-fitting-0001; b) http://aquisemprende.com/modules/com_sobi2/?swagelok-tube-fitting-980)

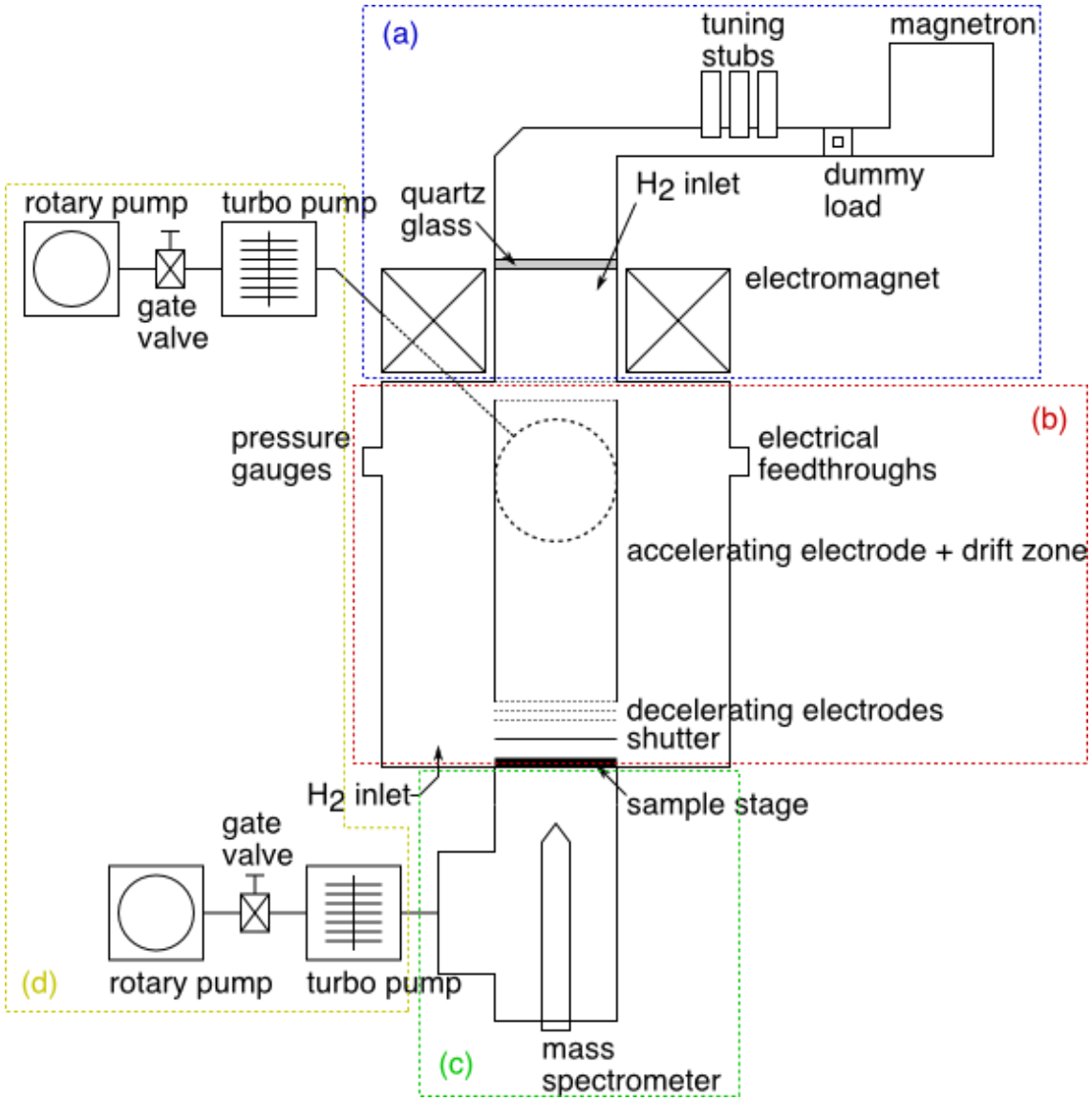

Figure 3. Construction schematic diagram of the HHIC system. Shown are 4 parts of the system: (a) ECR plasma generation chamber and components, (b) reaction chamber hosting the specimen, (c) analytical chamber separated by a plate with a small hole of radius 0.5 mm, (d) vacuum components.

2.1.1 ECR plasma

The plasma generation chamber is the vacuum part of the first block where a low-pressure electron cyclotron resonance (ECR) plasma is initiated (see Figure 3a). The choice of ECR as a high density plasma source was not accidental. Although there are other high density plasma sources available, such as helicon sources (Davies et al., 1969;

Boswell, 1970; Boswell et al., 1987; Perry et al., 1991), inductively coupled plasma sources (Yamashita, 1989; Hopwood et al., 1993; Keller et al., 1993), high frequency capacitive plasma sources (Bersin, 1978; Chapman et al., 1980; Godyak et al., 1992; Flohr et al., 1993), or surface wave plasma sources (Tuma, 1970; Ricard et al., 1988; Moisan et al., 1991; Margot et al., 1993), the need for specific spatial configuration and low operating pressure led to the choice of an ECR plasma source.

The driving force are free electrons present in a gaseous environment, be it hydrogen, helium, or any other gas. These free electrons are given energy by the right-hand circularly polarized incoming microwaves and being present in a strong and uniform dc magnetic field (B = 87.5 mT, set up by a solenoid electromagnet), they revolve around a cylindrical chamber. On their way they collide with molecules of the given gas and possessing enough energy they partially ionise the gas.

The microwave energy is generated using an electro-mechanical resonator (magnetron) at a frequency of 2.45 GHz, and directed to the plasma chamber through a waveguide. It is coupled to the vacuum system through a quartz window, which is properly sealed on both sides allowing only an insignificant amount of microwaves to leak outside, as well as keeping the vacuum tight. The most efficient operation is achieved when the maximum of microwave energy is absorbed in plasma. To control and modulate the amount of absorbed energy, three tuning stubs are inserted into the waveguide. The remaining amount of reflected microwaves should never reach the magnetron. For this reason, the reflected radiation is deflected into a damping compartment situated between the tuning stub and the magnetron entrance using a circulator.

From the bottom, the plasma chamber is separated from the reaction chamber by a perforated grounded electrode (Figure 4) with a hole size of 1.2 mm and a pitch size of 1.9 mm, which serves two purposes: (a) it prevents residual microwaves from leaving the plasma chamber; (b) it sets up a ground potential for extraction of charged particles.

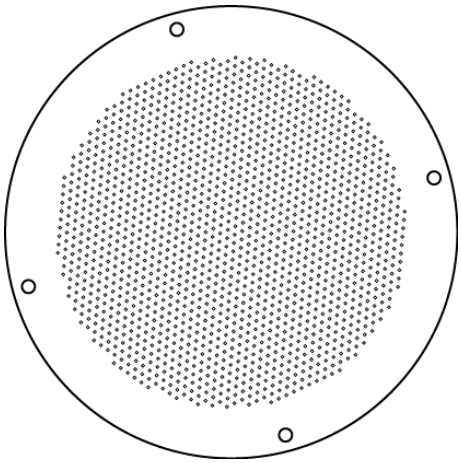

Figure 4. Grounding electrode with a hole size of 1.2 mm and a pitch size of 1.9 mm.

In the top part of this chamber there is also a gas inlet connected directly to a specially designed flange.

2.1.2 Reaction chamber

The reaction chamber is a cylindrical area, which hosts ion lenses, sample stage, shutter, pressure gauges, and electrical feedthroughs (see Figure 3b for schematics, Figure 5 for detail). At the very top is an accelerating electrode made of wire mesh of pitch 5 mm (all other mesh electrodes are made in the same way), suspended from the top flange and separated by ceramic stand-offs. This electrode is a part of a drift zone, which is an electric field-free region enclosed by a sheet of metal. The bottom part of the drift zone is again comprised of an electrode. Underneath the drift zone is a set of two electrodes that serve as decelerating electrodes towards both ions and electrons. The first electrode is biased oppositely to the drift zone, whereas the second one shares the same polarity as the applied accelerating voltage. In other words, the first electrode repels residual positive ions and the second one residual electrons. Inside the system, all electrical connections are secured using copper wires with a vacuum compliant insulation attached to the electrical feedthroughs situated at the side of the reaction chamber, and at the bottom flange, depending upon whether the wiring leads to the parts moving up and down along with the hoist or are connected to the stationary parts on the bottom flange. On the

outside, standard electrical wires with proper insulation are used for connection to three independent voltage power supplies.

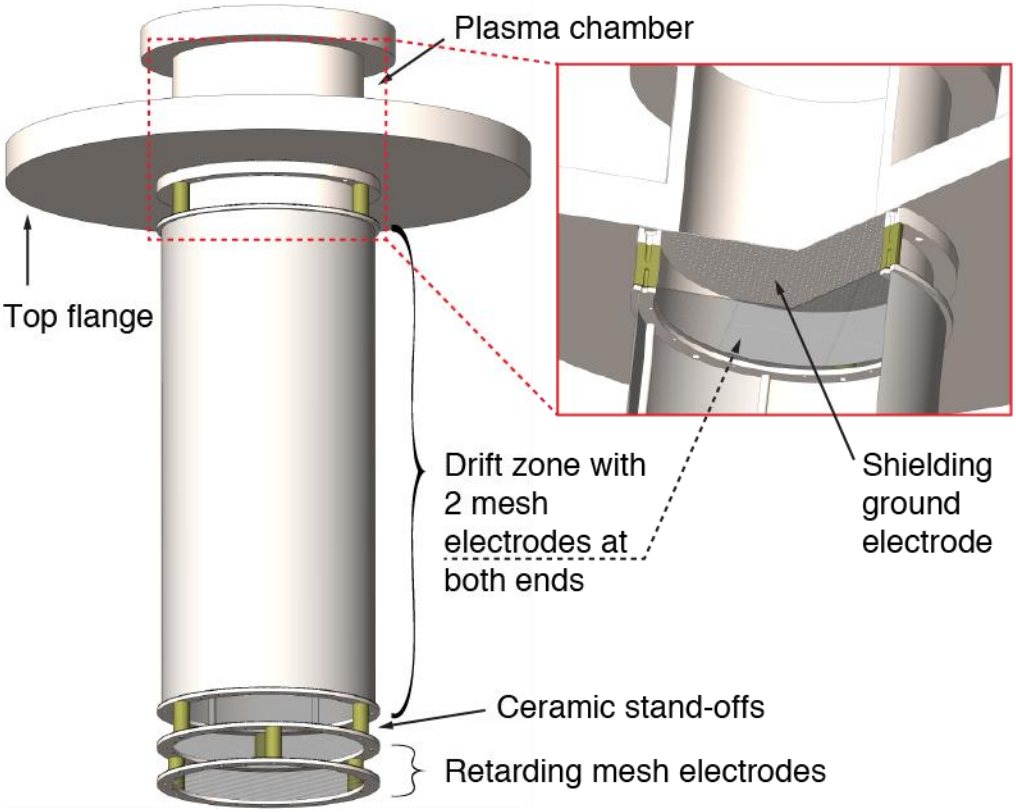

Figure 5. Detailed and expanded views of the reaction and plasma vacuum chambers. The mesh electrodes are made from a thin stain-less steel wire of diameter 100 µm and the pitch of 5 mm. The overall length of the drift zone is 45 cm and the diameter is 15.24 cm. The length of the ceramic stand-offs is 2.54 cm.

At the very bottom of the chamber is a sample stage in an intimate contact with the bottom flange. The sample stage can be grounded or can float on a different potential, as application requires. It can also be made of relatively thick metal (5 mm) with a small hole in the centre in order to keep the analytical chamber at much lower pressure. Because the system as a whole lacks an introduction chamber, both the plasma and reaction chambers are mounted on a hoist that can be raised when a sample needs to be manipulated. As a result, the reaction chamber is sealed from the bottom flange using a Viton gasket, whereas all the other parts make use of copper gaskets.

Emerging from the bottom flange is a second, and final, gas inlet.

A shutter is a mechanical part, which covers a sample stage and is used to control the time of exposure. Currently, the system can be equipped with two types of shutters (see Figure 6): a) simple single-axle solid shutter, b) blade blinds. The former does not allow for an effective utilization of the whole area of the sample stage (6" in diameter). The latter covers the whole sample stage, but is slightly more difficult to control mechanically.

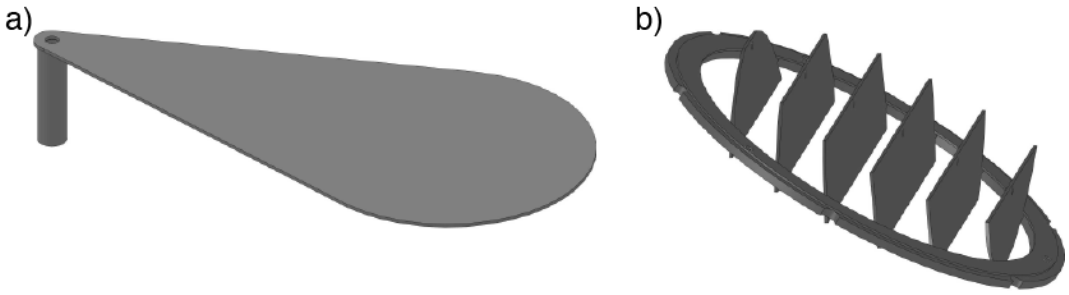

Figure 6. Two types of shutters for controlling time of exposure of samples to HHIC: a) single-axle solid shutter, b) blade blinds.

2.1.3 Vacuum system

The vacuum system comprises a proper set of equipment to evacuate the vacuum part of the reactor (vacuum pumps) as well as pressure gauges for monitoring purposes (see Figure 3d). From air, the system reaches the initial, low (~1000–1 mTorr), vacuum using a single-stage rotary vane pump (Figure 7a). In the current setup this type of pump is also referred to as a backing pump because it is necessary for the operation of turbomolecular pumps (also simply called turbo pumps, Figure 7b). A turbo pump brings the system to lower pressures, high vacuum, usually bellow 5×10^{-6} Torr. In our case, the background pressure for standard, day-to-day operation is below 2×10^{-6} Torr. The ultimate pressure of the HHIC system is around 1×10^{-8} Torr. In normal operation, the reactor and its vacuum generating components are left on to ensure the lowest degree of contamination possible. In the minimal configuration, the HHIC reactor is equipped with a Leybold Trivac CFS 16-25 single-stage rotary pump and a Pfeiffer TPH 521 turbomolecular pump. Whenever the RGA is connected to the analytical chamber, a second set of pumps

is utilized: a Varian DS 402 single-stage rotary pump and a Pfeiffer TPH 521 turbo pump.

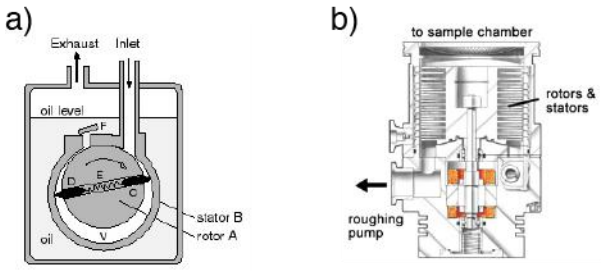

Figure 7. Cross-sections of a set of two vacuum pumps: a) rotary vane pump; b) turbomolecular pump (source http://www4.nau.edu/microanalysis/Microprobe-SEM/Instrumentation.html).

Because the design of this system does not allow for maintaining of high vacuum in the reaction chamber at all times (a lack of a load-lock mechanism), the system has to be brought down to atmospheric pressure in order to introduce samples inside the reactor. This operation consists of several steps: 1) closing a gate-valve situated between the turbo pump and the roughing pump; 2) shutting down the turbo pump and letting it slow down to its nominal venting speed; 3) introducing a nitrogen gas until the pressure inside the reactor reaches the atmospheric pressure. If the system is about to be serviced or out-of-order for a longer period of time, the roughing pumps are also turned off and brought to air, to avoid oil (oil vapour) creeping back up into the system.

Pressure gauges used on the system are of two types. First one is Pfeiffer PKR 251, a wide range gauge housing two gauge heads: a Pirani gauge (constant resistance type, Figure 8a, source Kurt J. Lesker Company) and an inverted magnetron ionisation gauge (Figure 8b) spanning a pressure range of $750–5\times10^{-9}$ Torr. This gauge is mainly used to monitor background gas pressure, as it is not very responsive or accurate in the pressure region of interest. The second gauge is MKS 626A, a 0.1 Torr Baratron® (MKS Instruments Inc.), which can accurately measure pressure spanning 3 orders of magnitude below the nominal pressure. It should be noted that Baratron gauges measure pressure directly (Figure 8c), whereas wide-range gauges operate indirectly, meaning that the

pressure is measured as a function of a pressure-dependent property of the gas (the pressure reading is always dependent on the nature of the gas). The working principle of Baratron gauges, also known as capacitance manometers, is based on a deflection of a diaphragm due to impinging gas molecules. The change in pressure is sensed as a change in capacitance between two parallel plates and transduced by a Wheatstone's bridge onto a voltage signal. Both gauges provide electrical input to their respective readouts.

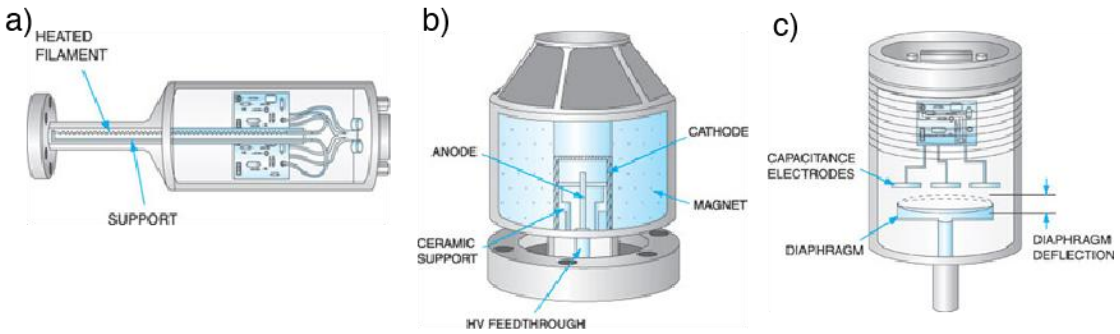

Figure 8. Cross-sections of a set of three pressure gauges: a) Pirani; b) cold cathode, inverted magnetron; c) capacitance manometer, Baratron (Courtesy of Kurt J. Lesker Company).

Both gauges are situated in the upper part of the reaction chamber, which means that the pressure measured in the reaction chamber differs from the pressure in the plasma chamber upon the plasma initiation and therefore throughout an experiment. It will also be affected by the close proximity to the turbo pump vacuum inlet. The reason being that the flow of gas in the plasma chamber is viscous, whereas in the reaction chamber it is molecular, especially in the region close to the pressure gauges and throughout most of the drift zone. However, this fact has no direct implication on any given experiment, and keeping all operational parameters across different experiments the same, does not adversely affect reproducibility.

It is known that maintaining a clean vacuum system is not an easy task. In high and ultra-high vacuum environments the major contaminants are adsorbed molecules on inner surfaces and samples themselves. To a certain degree one can never control the cleanliness of a sample, but can always take care of the system such that the contamination is minimal—assuming a proper choice of vacuum pumps. In order to

remove the contaminants on walls and other inner surfaces, one usually relies on elevated temperature (150–200°C) to desorb the molecules. Unfortunately, in the case of the HHIC reactor, it is impossible to do because the main chamber was designed as double-walled. It therefore relies exclusively on a UV-heating element inserted through the bottom flange inside the reaction chamber.

It should also be noted that all virtual leaks due to potential capsules of air (i.e., all screws used under vacuum have a hole drilled through the middle) were eliminated.

2.1.4 Analytical chamber

The analytical chamber is a home to a residual gas analyzer (RGA, see Figure 3c). In our case it is a Hiden SIM300P made by Hiden Analytical Inc. equipped with a secondary electron multiplier (SEM) detector. Its probe can be seen in Figure 9. The reasons for the existence of this separate chamber are: a) to have the means to analyze the HHIC method in terms of distribution of energy of hyperthermal neutral molecules; b) to use the spectrometer for background gas analysis (measure of contamination). This chamber is unnecessary for every day operation of the reactor. However, if one needs to place a sample farther away from the top-most electrode—to increase the average number of collision centres reducing the kinetic energy of the incident neutrals—this area can provide for such space.

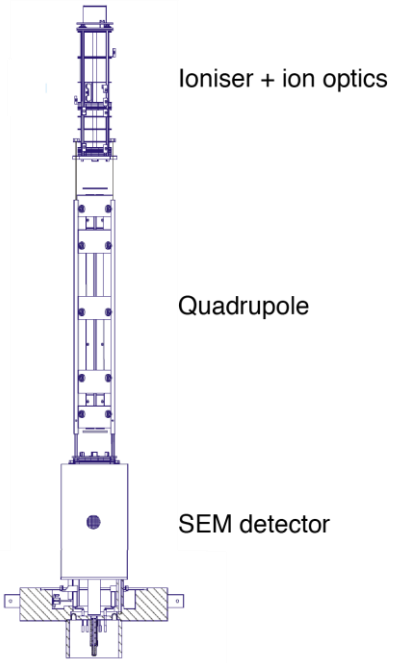

Figure 9. SIM300P probe construction schematics (Courtesy of Hiden Analytical Inc.).

Due to the nature of the working principle of the analyzer, and the fact that only molecules of interest need to be analyzed, the analytical chamber has to be kept at lower pressure than the reaction chamber. In other words, the analytical chamber needs to be differentially pumped. The RGA should not be operated at pressures above $5x10^{-6}$ Torr especially so if the background gas or the studied gas contains oxygen, which would significantly accelerate the oxidation of a filament.

2.2 Theoretical framework

It is necessary to provide basic theoretical background, which pertains to the most important aspects of HHIC. Among those are the generation of a high flux of hydrogen ions, which would serve as the primary collision initiators, the cascade of gas phase collisions in an electric-field-free drift zone, and the hydrogen abstraction from a C–H bond driven by molecular hyperthermal hydrogen.

Although indirectly, the hyperthermal hydrogen induced cross-linking is driven by plasma. It is a special kind of plasma, which can be sustained at low neutral gas pressures

due to the presence of strong steady magnetic field maintaining a high density of ionizing particles (Matsuo et al., 1982; Tokiguchi et al., 1986; Torii et al., 1987; Forster et al., 1989; Torii et al., 1992). The plasma is referred to as electron cyclotron resonance (ECR) plasma and dates its first inception to the early 1960's. It was first used in a configuration quite similar to that shown in Figure 3 for space craft propulsion application by Miller (Miller, 1966; Kosmahl et al., 1967) with the reaction chamber replaced by an opening for the plasma rocket exhaust. The ECR plasmas were also investigated in connection to controlled fusion (Consoli et al., 1963; Bardet et al., 1964; Dandl et al., 1964). A major boom of ECR plasma sources began after it was discovered that these sources could be used for semiconductor processing applications offering new and desirable parameter regimes pioneered by Suzuki et al. in 1977.

2.2.1 Electron cyclotron resonance plasma

2.2.1.1 Introduction

Some people say that the universe, its baryonic content, consists of up to 95% of plasma. It's always harder to disprove something than to prove it and this statement is also the case. But the understanding of facts is that at the beginning of time, the universe was all plasma. These days, stars, nebulae, interstellar space, they are all filled with plasma. If we look closer to our backyards, in lightning, fluorescent light bulbs, or ionosphere, one can find plasmas. Liquid mercury also exhibits many characteristics typical of conventional plasmas. But what really is plasma?

The term finds its origin in the Greek word πλασμα (meaning "mouldable substance" or "jelly") and was pioneered by the Czech anatomist and psychologist Jan Evangelista Purkyně (1787–1869) who working on clearing blood of its various corpuscles observed a transparent liquid. In 1927, the American chemist and Nobel laureate Irving Langmuir used the term *plasma* in relation to ionized gas (the electrified fluid carrying electrons and ions reminded him of the way blood plasma carries red and white corpuscles). So what is it?

Any matter of inner structure is bonded together by energies above the ambient thermal energy and when heated they decompose. At constant pressure and increasing

temperature a substance changes its state from solid to liquid to gas to plasma (plasma is sometimes referred to as the fourth state of matter). Typical temperatures required to form plasmas from pure substances in thermal equilibrium range from 4000 K (easily ionized elements) to 20,000 K (not so easily ionized elements). Similarly, atoms brought in temperature (energy) close to or above the ionization energy break down into positive ions and free electrons. In reality, the electrons are not free in a sense they would not be affected by the presence of, or lacked the interaction with, another matter. On the contrary, they, and the newly created positive ions are mutually affected by their respective electromagnetic fields, yet being separated they undergo a characteristic collective motion. It is worth reminding that the decomposition of a molecule occurs before the ionization, therefore, plasmas are also defined as sufficiently ionized gasses to exhibit plasma-like behaviour. It logically follows that when plasma is formed from an initially neutral gas it will also be a neutral body on the outside. By extension, if predominantly positively or negatively charged gas forms plasma, the body will also be appropriately charged.

2.2.1.2 Physical description of plasma

A substance in the plasma state is typically characterized in terms of number density of charged particles as $n_e \approx n_i \approx n_n$ (m^{-3})—a quasi-neutrality condition, where the subscript e stands for electrons, i for ions, and n for neutral gas molecules, and in thermal equilibrium by temperature $T_e = T_i = T_n$. As an example, if we look back and assert that stars are plasmas, we can say that these are in thermal equilibrium. For discharge plasmas typically used in laboratories and industrial processes (terrestrial plasmas), the ionic particles are almost never in thermal equilibrium either between themselves or with the surroundings, whereas electrons are near thermal equilibrium. The reason is that the power applied to these weakly ionized plasmas preferentially heats free electrons (light particles) over ions (heavy particles), which also efficiently exchange energy with the background gas molecules, leading to $T_e \gg T_i$. Because of this fact, it is the electrons that are responsible for dissociation and ionization of molecules, although T_e is usually less than both the dissociation energy (E_{diss}) and the ionization energy (E_{iz}). Nevertheless, we shall understand that electrons are distributed in energy and the high-energy tail is

responsible for the dissociation and ionization process. The electron energy distribution typically follows a Maxwell–Boltzmann distribution, however, electron heating and electron–neutral collisions can skew the high-energy tail.

Let us now look at the most fundamental parameters of plasmas, which define the typical plasma length- and time-scales for collective plasma effects. First of these parameters is the Debye length λ_D. It is defined as a length scale beyond which the electric field penetration generated by charged particles gets shielded. In other words, within the Debye length significant charge densities can exist and be screened out from the outside. One of the possible explanations of this behaviour exploits the fact that the plasma medium is electrically highly conductive, which allows plasma current to flow freely and in effect shorts out internal electric fields. Another possibility is to tackle the Debye length shielding as a dielectric phenomenon, where the redistribution of space charge associated with the polarizability of the plasma medium is responsible for shielding the penetration of the external electric field. Without a derivation let's define the Debye length as follows:

$$\lambda_D = \sqrt{\frac{\varepsilon_0 k}{e^2\left(\frac{n_e}{T_e} + \frac{n_i}{T_i}\right)}}$$

where the ionic term is usually (on normal—fast—time scales) left out as the mobility of ions is much lower than that of electrons, leaving us with the Debye length for electrons $\lambda_{D_e} = (\varepsilon k T_e / n_e e^2)^{1/2}$.

Another fundamental plasma parameter is the plasma frequency. The plasma frequency is a measure of a typical electrostatic oscillation frequency in response to a small charge density perturbation. It is characteristic to each species but given the relatively high electron frequency it is generally only defined as

$$f_p = \frac{1}{2\pi}\sqrt{\frac{e^2 n}{\varepsilon_0 m_e}} \equiv \frac{1}{\tau_p}$$

in terms of electron plasma frequency, yet referred to as simply "plasma frequency" in plasma physics. τ_p represents the plasma period, a characteristic plasma time-scale. The typical plasma frequencies for discharges lie in the microwave region (1–10 GHz). Although the ion plasma frequency is much smaller than the electron plasma frequency, it could simply be defined using the same equation as for f_p and replacing m_e with m_i. Consequently, the total plasma frequency would be given as $f_p = (f_e^2 + f_i^2)^{1/2}$.

To reflect back on the definitions of plasma, using the above fundamental parameters, one can further describe plasma by a set of simple relations:

$$L \gg \lambda_D \text{ and } \tau \gg \tau_p$$

where τ and L represent the typical time-scale and length-scale of a given discharge. We can then say that the characteristic collective plasma behaviour is only observed on time-scales longer than the plasma period and distance-scales larger than the Debye length.

In a vacuum system the plasma body is usually surrounded by grounded walls. At the instant of plasma initiation the potential profile across the plasma chamber is constant and the quasi-neutrality condition ($n_e \cong n_i$) holds. As we have already stated the electrons possessing much higher energy than ions move faster and are lost to the walls at a higher rate. In the short time interval during which they accelerate to the walls, the density of electrons and positive ions is no longer equal and $n_i \gg n_e$ in a region close to the walls, a sheath. This leads to a build up of potential and the electric field vector points in the direction away from plasma and into a wall. Electrons, in effect, experience a centripetal force confining them to the plasma, whereas ions get accelerated into the walls. When all transient effects disappear and the system reaches equilibrium (charge balance), the non-neutral potential regions between the walls and plasma are formed and are called sheaths.

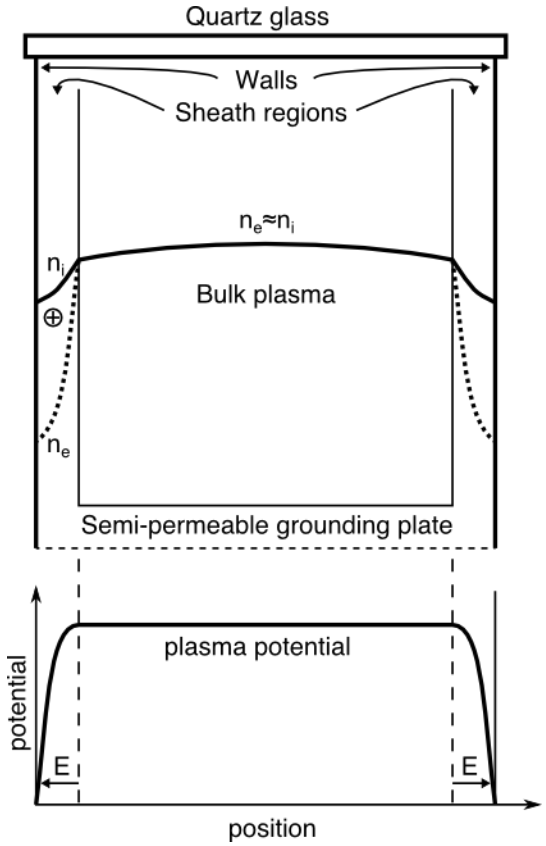

Figure 10. Separation of plasma body into bulk plasma and sheath regions. The sheath regions show number densities $n_i \gg n_e$ with strong electric field. The bulk plasma is approximated as an electric field-free region with $n_i = n_e$ and plasma potential V_p.

The fact that plasma can be viewed as a combination of bulk plasma (low-field, quasi-neutral region) and sheath regions (high-field region) is a concept valid for all types of discharges (Figure 10). Generally speaking, this concept makes the understanding, modeling, and description of plasma parameters easier, because it allows treating the separate regions using different approximations.

The concept of sheath regions as described above is still an approximation. If we move another step forward in providing more accurate description, the sheath region—non-neutral and a few Debye lengths long—has to be preceded by a pre-sheath region in order to maintain ion flux continuity. This condition gives rise to an ion velocity at the plasma–sheath interface known as the Bohm velocity. The description of plasma behaviour can

get even more complicated if, for example, the ion energy can no longer be ignored with respect to the electron energy, as is the case in highly ionized plasmas. Or if the background gas is electronegative, which causes imbalance in the negative charge velocities of fast moving electrons versus slow negative ions effecting conditions at the sheath interface.

Overall, having a strong steady magnetic field along the cylindrical axis leads to a better confinement of particles and consequently smaller loss of particles to the walls (low-voltage sheaths at all surfaces). It also increases both charge density and the ion flux.

2.2.1.3 Plasma radiation

The most important emission processes involve a single-photon generation. Among those, the electric dipole radiation (as a first-order approximation) is the strongest mechanism. A radiative relaxation of an excited molecular state can proceed in one of the following schemes (always assuming that the quantum-mechanical selection rules are satisfied): a) transition between electronic states of different energy; b) transition between vibrational or rotational levels (of the same vibrational state) for the same electronic state; c) combination of transitions between rotational and vibrational levels of different electronic states. Since the homonuclear H_2 does not possess a permanent dipole moment, the transitions in b) are forbidden under the selection rules. However, magnetic dipole and electric quadrupole transitions (as higher order approximations) may still occur.

Because the primary gas used in the reactor is hydrogen it is useful to show a schematic diagram of various radiative transitions for a hydrogen atom. The emission spectrum spans wavelengths from infrared to ultraviolet.

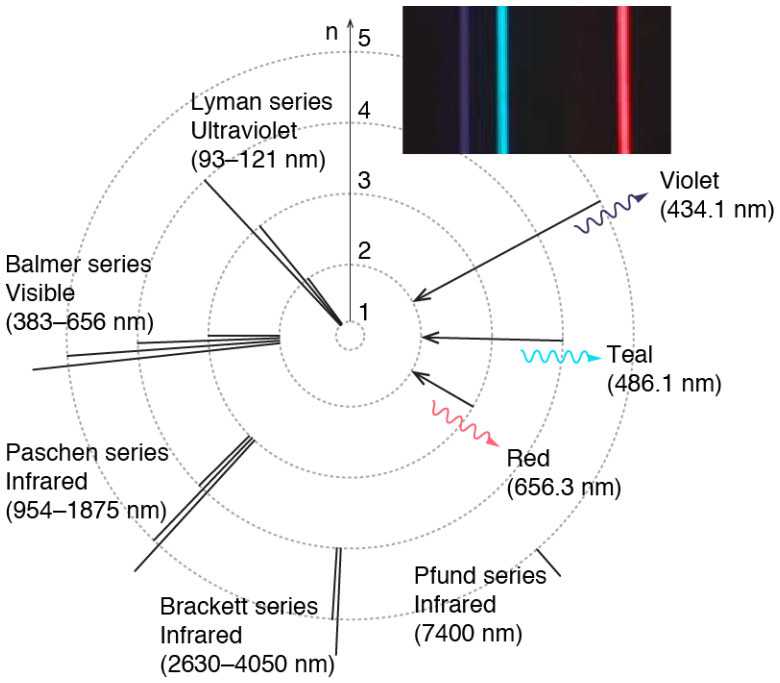

Figure 11. Simplified emission spectrum of hydrogen atom. Spectral lines in the visible spectrum are shown in the black window.

In the cyclotron plasmas, the emission lines due to the radiation from accelerating charges would be expected. However, because the plasma frequency (typically 1–10 GHz, in our case ~6 GHz for high-density magnetized plasma) is usually higher than the cyclotron frequency (in our case 2.45 GHz) the radiation will not occur, although higher order harmonics are possible to observe with much lower intensities. In highly improbable and theoretical situation even soft X-ray radiation would be possible to generate if the electron life time was sufficiently high, the constraining potential high enough to keep the electrons in orbit, and the amplitude of the stimulating microwave radiation necessarily high.

It should also be noted that the atomic emission lines will get broadened due to natural broadening, Doppler broadening, and Stark broadening. Natural broadening is common to all atomic transitions between two states as represented by simple oscillators with given frequencies and a damping width of the corresponding spectral line. The Doppler shift is a well-known effect, which in plasma affects both directly emitted as well as scattered radiation, where the latter reflects the velocity distribution function of the

atoms. The Stark broadening, in short, is a result of energy level splitting of hydrogen and hydrogen-like (highly excited) atoms in the presence of static electric field.

The following example (paraphrasing Lieberman et al., 2005) illustrates some molecular transitions in H_2, which lead to radiative emission. At 11.5 eV, the ${}^1\Sigma_u^+$ (a brief explanation of the nomenclature*) bound state is excited with subsequent electric dipole radiation in the ultraviolet region to the ${}^1\Sigma_g^+$ ground state (Lyman UV series from $n \geq 2$ to $n = 1$). At 11.8 eV, there is excitation to the ${}^3\Sigma_g^+$ bound state, followed by electric dipole radiation to the ${}^3\Sigma_u^+$ repulsive state, followed by a dissociation leaving each atom with ~2.2 eV. At 12.6 eV, the ${}^1\Pi_u$ bound state is excited, with UV emission to the ground state.

2.2.1.4 ECR plasma source

An ECR plasma source exploits the fact that electrons gyrating at a certain frequency in a magnetic field are able to absorb the energy carried by an electromagnetic wave. The frequency of gyration f_c has to match the frequency at which the electric field vector of the incident electromagnetic wave revolves around its wave vector. We can then calculate the necessary strength of the magnetic field

$$B = \frac{2\pi f_c m_e}{e}$$

For the magnetron source attached to the HHIC reactor radiating at frequency $f = 2.45$ GHz, the "minimum" strength of the magnetic is $B = 87.5$ mT. Under these conditions the radius of gyration is

* The prefix superscript denotes spin multiplicity, 2S+1, where S is the sum of individual spins. The capital Greek letters represent the total orbital angular momentum Λ along the internuclear axis (analogous to atomic s, p, d, f…) with the symbols Σ, Π, Δ, Φ, etc. All states except Σ are doubly degenerate. The Σ state, however, is further classified with suffix superscript "+" or "–", which represent the behaviour of an electronic eigenfunction upon reflection through the internuclear axis (plane of symmetry for diatomic molecules), "+" unchanged, "–" changes spin. Similarly, "g" and "u" (from German "even" and "odd") denotes whether the electronic eigenfunction if symmetric or antisymmetric with respect to interchange of the nuclei. Sometimes, the very first letter shows whether the state is a ground state, capital letter X, or a successive excited state of the same spin multiplicity but increasing energy A, B, C, etc.

$$R = \sqrt{\frac{2m_e V}{eB^2}} \cong 3.85 \times 10^{-5}\sqrt{V}\ \text{m},$$

and depending upon the potential through which the electron acquires its energy (for example 20 V), the radius of gyration is $R \cong 170$ μm. If we look at hydrogen ions, where the ions are in thermal equilibrium with the neutrals, the magnitude of the radii of gyration are of $R_{H^+} \cong 270$ μm and $R_{H_2^+} \cong 380$ um. In the case of ambipolar acceleration, where the ions can take on a significant portion of the electron energy (10 eV for example), the radii of gyration are $R_{H^+} \cong 5.2$ mm and $R_{H_2^+} \cong 7.4$ mm. On both examples, it is evident that ions are less strongly confined than electrons.

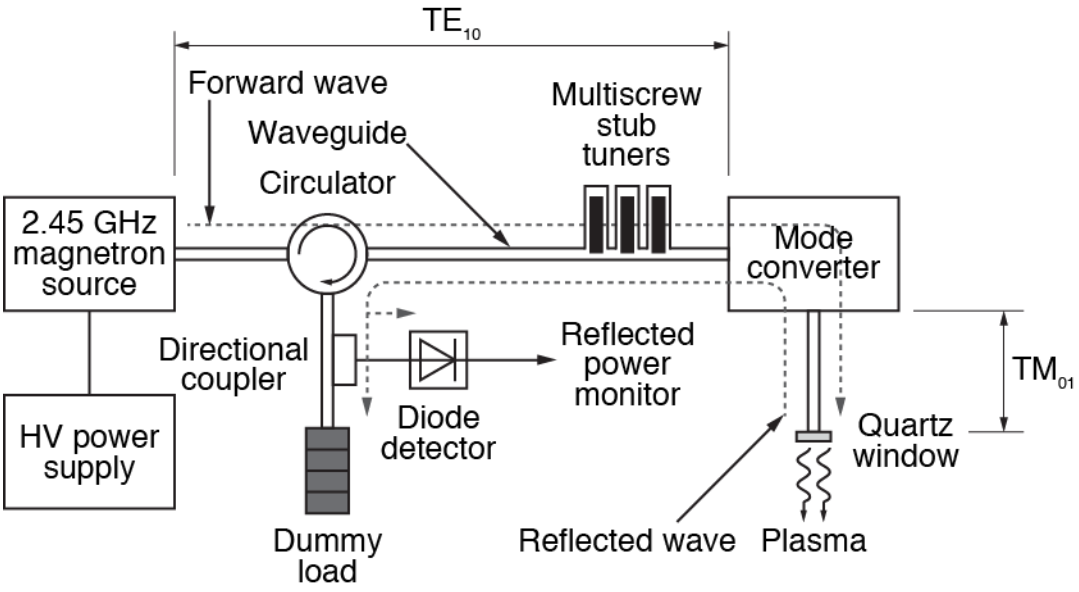

Figure 12. Schematic diagram of coupling of the microwave energy to plasma.

The following few paragraphs will explain how the plasma gets generated and sustained. Using Figure 12 as a reference, the process starts at the left with a radiation-generating component called the magnetron. It is a cleverly designed electro-magneto-mechanical oscillator, which relies on the interaction of electrons emitted from a hot filament (at the center of the cavity) with the electric and magnetic fields. The electrons move radially outward to the ring anode where they oscillate between regions of high and low density.

As they do (accelerate), they emit electromagnetic waves at frequency corresponding to the physical dimensions of the cavity.

The generated waves ($\lambda \cong 12.2$ cm) are transmitted using a hollow waveguide made of conductive metal of proper thickness (to account for the skin effect) and dimensions (to carry the dominant TE_{10} mode only). Because the waveguide consists of one solid conductor, the carried transverse wave can only be of two forms: a) transverse electric (TE), where the electric field vector is always perpendicular to the direction of propagation and the magnetic field vector has both components; b) transverse magnetic (TM), is the opposite and has the magnetic field vector always perpendicular to the direction of propagation. The way the waves propagate along a waveguide is quite hard to imagine and is usually portrayed as two waves bouncing back and forth between the walls of the waveguide at certain (allowed) angles and forming a standing wave pattern. It is therefore much easier to show a distribution of electric field along the waveguide in cross-sections. Figure 13 shows such a distribution for two segments of the waveguide carrying two different modes. A mode is essentially a two-dimensional solution to a boundary condition problem (wave equation). For a rectangular waveguide the subscripts indicate the number of half-wave patterns in both x and y directions, where the first subscript usually corresponds to the longer side. In circular waveguides, the first subscript represents the number of full-wave patterns around the circumference and the second subscript the number of half-wave patterns across the diameter of the waveguide.

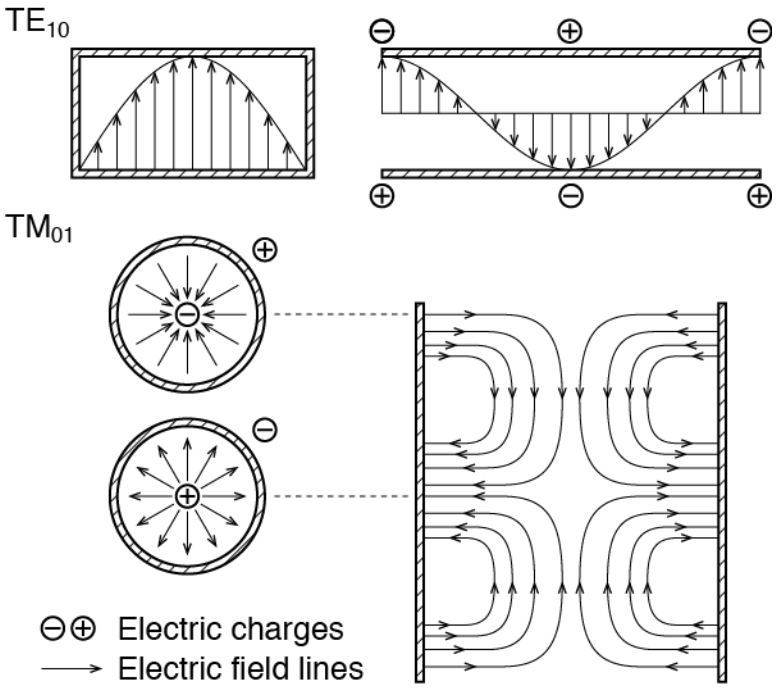

Figure 13. Distribution of the electric field in two different transverse modes of propagation of electromagnetic waves. A cross-section of a rectangular waveguide carrying a TE_{10} mode in shown at the top. A cross-section of a circular waveguide carrying a TM_{01} mode is shown at the bottom.

The magnetron head, positioned a quarter-wavelength away from the back wall of the waveguide, is radiating out electromagnetic waves forming the TE_{10} mode, which travels to the right until it reaches a "mode converter" ($TE_{10} \rightarrow TM_{01}$, Figure 14). At that point the wave enters a circular waveguide and propagates down to the plasma chamber. To minimize the amount of reflected microwave energy a set of three multi-screw tuning stubs is inserted prior to the mode converter. The stubs move up and down in the waveguide and are responsible for load-matching as seen by the microwaves and represented by the plasma. To control this process, a diode detector is used to monitor the reflected power. The reflected microwaves must therefore be redirected using a ferrite circulator placed between the stubs and the magnetron to the detector through a bidirectional coupler and the rest is dumped into a dummy load. The dummy load is made of highly absorbing material and water-cooled because sometimes a significant amount of energy needs to be dissipated during the load-matching process.

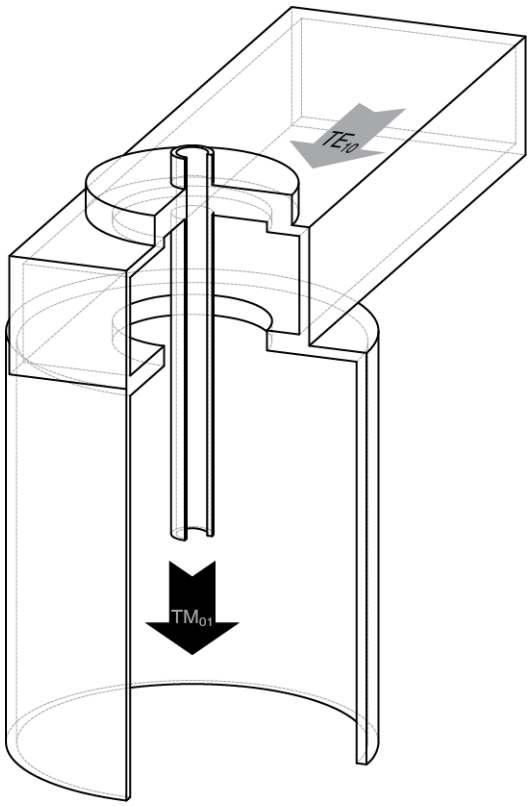

Figure 14. Mode converter transforming the TE_{10} mode onto the TM_{01} mode (note: the TM_{01} mode cannot exist in a rectangular waveguide).

Once the microwave power is delivered into the plasma chamber, the carried energy is used to heat up the free electrons present in the background gas. The mechanism can be explained by the fact that any linearly polarized wave can be decomposed into two circularly polarized waves of half the amplitude rotating in opposite directions: the right-hand circularly polarized wave (RHP) and the left-hand circularly polarized wave (LHP)[*]. When the frequency of the RHP wave approaches the frequency of gyration as given by the magnetic field, the free electrons are synchronously accelerated a) tangentially by the wave's electric field and b) perpendicularly by the external magnetic field. The LHP wave accelerates the electrons for half a cycle and decelerates for the other half rendering a zero average energy gain. The situation is more complicated given

[*] The usual convention for labeling right-hand and left-hand circular polarization is as follows: if we look at the wave when coming straight toward us and the end of the electric field vector rotates counterclockwise, we call it right-hand circular polarization.

the fact that the resonance zone does not span the whole plasma vacuum chamber but is rather narrow and concentrated and its relative position depends upon the absorption length and propagation distance of the microwave energy in the plasma. For regions where $f \neq f_c$, electrons do not continuously gain energy but the energy gain oscillates at frequency given by the difference $f - f_c$ leading to a transverse energy gain or loss as electrons move along the chamber's cylindrical axis. It is prudent to say that in ECR sources the propagation and absorption of microwave power in plasma is not yet fully understood and is still an active area of research.

Although the TM_{01} mode is unpolarized in the waveguide, it can still be locally decomposed at the plasma surface into plane-polarized waves (see for example Popov, 1995). The electron heating mechanism, the microwave absorption, as previously described is also valid for the TM_{01} mode.

In ECR sources the density of neutral particles is typically one or two orders of magnitude lower than the plasma density. The neutral pressure has been reported to decrease by up to 70% (Gorbatkin et al., 1990) and even by up to 86% (Rossnagel et al., 1990) for an argon plasma at an initial pressure of 0.7 mTorr. In the case of our reactor, we have observed a lower decrease in neutral pressure anywhere between 6–12% in the reaction chamber. Such a low drop is attributed to the separation of the plasma and reaction chambers by a perforated grounding plate, which helps to reduce differential pressure changes in either chamber.

It should be noted that higher plasma densities uniformly distributed along the diameter of the plasma chamber could be achieved if the magnetic field is above the B_{ECR} so that the microwave power propagates some distance before damping. This effect is attributed to the self-consistent interaction between wave propagation and the plasma density (Stevens et al., 1992) as well as ECR damping, which allows wave refraction to radially spread out the microwave power (Samukawa et al., 1991). The plasma density profile then approaches the simplified profile shown in Figure 10.

The magnetic field set up by the solenoid coil is nearly uniform in the ECR region and differs from upstream plasma configurations where the non-uniformity of the magnetic

field is responsible for the drift of particles along its field lines to the sample holder. The only purpose of our ECR plasma source is to generate a high flux of positive hydrogen ions. As opposed to other vacuum plasma processing used in etching or deposition, the uniformity of the plasma density is not an issue. However, it has been observed that the plasma region expands beyond its bounds (as represented by the grounding plate) and gives rise to a distributed potential $V_d \approx 10$ V (as measured at the accelerating electrode).

The plasma potential in ECR sources is known to increases with decreasing pressure, with a typical value of $V_p \approx 20$ V at 1 mTorr (Lee et al., 1989). It has also been shown (Ono et al., 1986) that the plasma potential can decrease from over 50 V down to 10 V through a downstream region at low pressures (<1 mTorr).

All energy losses related to electrons due to ionization, excitation, or elastic collisions, have to be supplied back to the system. However, in general, we could state that all energy losses related to the ECR plasma and its application in the HHIC system (e.g., out of plasma radiation, extracted ions, escaped electrons) must be recovered. The microwave radiation provides for such a continuous source of energy.

2.2.1.5 Conclusion

It is certain that without the possibility of operating the HHIC reactor at low neutral pressures the HHIC method would be impossible to realize because it relies on a certain average number of collisions in the drift zone. In other words, the inelastic mean free path of hydrogen molecules and atoms should be at least five times lower than the characteristic length scale of the drift zone. High plasma density achievable in ECR plasmas is also an invaluable asset. If the density of hyperthermal particles cleaving C–H bonds per unit area per unit time was low, the material would have to be bombarded much longer unnecessarily exposing it to potentially harmful radiation and elevated temperatures. The configuration of the system, although imperfect, drastically reduces the number of reactive species, which would otherwise drive undesirable side reactions. The system, therefore, cannot be classified as a remote plasma system, because the sample for all practical purposes does not see the plasma body.

A major drawback of the HHIC method is the presence of electromagnetic waves of various frequencies (primarily deep vacuum UV). This applies to materials (most current organic semiconductors) highly sensitive to UV and visible radiation (Li et al., 2008; Shuttle et al., 2008; Sezen et al., 2009; Devine et al., 2010), for which the inevitable absorption causes severe degradation of physical, chemical, or electrical properties.

2.2.2 Cascade of collisions

In order to accurately and sufficiently describe the cascade of collision taking place in the drift zone, we have to understand the various types of gas phase collisions. We will talk about a broader spectrum of collisional mechanisms, as they are relevant to both plasma and HHIC collision cascade.

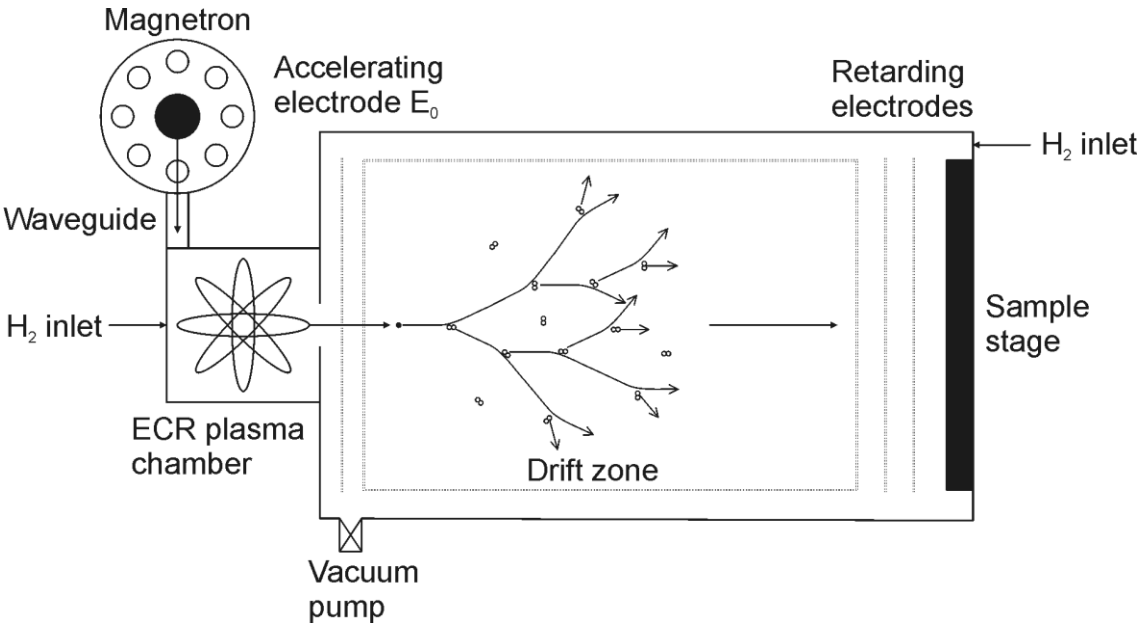

Figure 15. Schematic diagram of the HHIC reactor showing the generation of hydrogen ions, their extraction, and collisions with background gas molecules, as well as reflection of charged particles above the sample stage.

2.2.2.1 Introduction

A collision is a process describing intimate interaction of two and more particles. In our case we will constrain our study to the interaction of only two particles (binary collisions) in classical sense, whether the individual particles are electrons, ions, or molecules. In

physical terms, the collision will describe an exchange of any combination of the following properties: momentum, energy, or electrical charge.

The main processes involved in electron–atom–ion collisions typically include elastic and inelastic scattering. In atomic interactions we are interested in elastic energy and momentum transfer, resonant charge transfer, and inelastic excitation and ionization. For molecular interaction we enrich our collisional ensemble with, but not restricted to, electron driven dissociation, dissociative recombination, vibrational and rotational excitations, transfer of excitation, and ionic attachment and detachment.

Reactive collisional processes driving chemical and physical reactions are well described and have been explored and utilized in the past. Predominantly, these processes involve an interaction of primary atomic or molecular ionic species with other objects (i.e., neutrals, ions, electrons) in gaseous environment or with a solid surface. Studies of neutral particles involved in similar interactions are scarce. Based on the average translational energy of the incident particles incident upon an atom/molecule/surface system, we can distinguish the following fundamental processes[*]: molecular physisorption (10^{-1}–10^{0}), inellastic scattering (10^{-1}–10^{2}), soft-landing (10^{0}–10^{1}), dissociative chemisorption (10^{0}–10^{1}), atomic abstraction (10^{1}–10^{2}), nonadiabatic electron transfer (10^{1}–10^{4}), dissociative scattering (10^{1}–10^{4}), sputtering (10^{1}–10^{4}), and implantation (10^{2}–10^{4}). Ionic processes with reactive projectiles at low energies are not broadly used mainly because it is difficult to generate a high flux of well-collimated beams due to strong space charge interaction. However, some of these well known processes that utilize energetic gaseous reactants under vacuum conditions have found its way into a number of industrial applications such as plasma processing, ion implantation, reactive ion etching, or magnetron sputtering. These processes are routinely employed in the fabrication of microelectronic devices and some have even been used in organic electronic industry (e.g., e-beam evaporation).

Among the enumerated processes, there are only a few relevant to the HHIC method. The most important is atomic abstraction by which an atom is transferred to or from a surface

[*] The values represent approximate energy ranges over which the processes typically occur.

upon an impact by the incident hyperthermal molecule. It is also possible that due to a wide energy distribution of hyperthermal hydrogen projectiles generated by a cascade of collisions can be deposited intact (at energies bellow their dissociation threshold) to the surface in a soft-landing manner. If the incident energy exceeds the hydrogen molecule dissociation energy 4.52 eV (Lide, 2009), a dissociative chemisorption or scattering may occur. In the case of the dissociative chemisorption, the incident molecule dissociates upon impact and the resulting fragments bind tightly to the surface. In dissociative scattering, on the other hand, the breaking of the incident molecule produces only gas-phase fragments. In the sections of Chapter 2, the main focus is put on the process of atomic abstraction by molecular hyperthermal hydrogen without considering molecular dissociation as will be discussed in Section 2.2.4.3.

Among the most important parameters for gas phase collisions are the scattering cross-section (total and differential), mean free path, impact parameter, and the rate constant. In the hard-sphere approximation*, which we will use throughout the text, the concept of collision (scattering) cross-section σ is defined as an effective area for collision. For two colliding elastic hard spheres the collision cross-section is given by $\sigma = \pi r^2$.

* An atom is perceived as a sphere of constant diameter. Based on our theoretical Monte Carlo calculations, the difference between hard-sphere and variable hard-sphere approximations is for the purpose of this work insignificant.

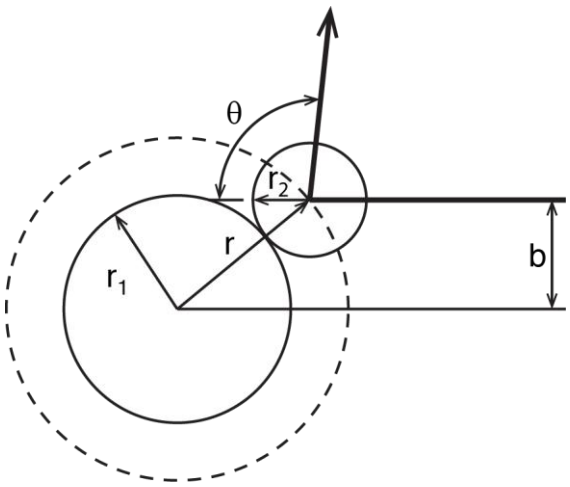

Figure 16. Hard-sphere scattering. A particle of radius r_2 impinges on an infinitely massive particle of radius r_1 and scatters at an angle θ. The impact parameter b is the distance between the centres as projected onto the axis perpendicular to the axis of incidence.

It is sometimes more useful to define the scattering cross-section as a function of a specific range of angles at which the particles scatter. The range of angles is represented by a differential solid angle $d\Omega = \sin\theta \, d\theta d\phi$, which in a radially symmetric scattering potential, such as the Coulombic potential, reduces to $d\Omega = 2\pi \sin\theta \, d\theta$. The differential cross-section is then defined as

$$d\sigma = \frac{b}{\sin\theta} \left| \frac{db}{d\theta} \right| d\Omega \, .$$

It could be shown that when the differential scattering cross-section is integrated over the solid angle it yields the total cross-section as defined above.

The mean free path or the average distance between collisions is defined, assuming that the colliding particles have an average relative velocity calculated from a molecular velocity distribution, as

$$\lambda = \frac{1}{\sqrt{2}\pi r^2 n}$$

where n is the number density of particles.

The rate constant, which has a meaning of collision frequency (=density × cross-section × relative speed) per unit density, is given as

$$K = \sigma v$$

where v is the relative velocity of the particles before collision.

2.2.2.2 Elastic collisions

This section covers the fundamental dynamics of elastic collisions. We shall put together a set of three equations, which will describe an elastic collision between two particles having initial velocities v_{1i} and $v_{2i} = 0$ and masses m_1 and m_2 (see Figure 17 for illustration). The equations for the conservation of momentum are written as

$$m_1 v_{1i} = m_1 v_{1f} \cos\theta_1 + m_2 v_{2f} \cos\theta_2$$
$$0 = m_1 v_{1f} \sin\theta_1 - m_2 v_{2f} \sin\theta_2$$

and the equation for the conservation of energy is

$$\frac{1}{2} m_1 v_{1i}^2 = \frac{1}{2} m_1 v_{1f}^2 + \frac{1}{2} m_2 v_{2f}^2$$

where θ_1 is the angle at which the first particle leaves upon scattering, and θ_2 is the scattering angle of the second particle. Both angles are relative to $\overrightarrow{v_1}$. After solving the three equations for the kinetic energy of particle 2, we get

$$\frac{1}{2} m_2 v_{2f}^2 = \frac{1}{2} m_1 v_{1i}^2 \frac{4 m_1 m_2}{(m_1 + m_2)^2} \cos^2\theta_2$$

which can be rewritten in terms of KE_{2f} and KE_{1i} as

$$\frac{KE_{2f}}{KE_{1i}} = \frac{4 m_1 m_2}{(m_1 + m_2)^2} \cos^2\theta_2 \ . \qquad (1)$$

The ratio of kinetic energies tells us how much energy is transferred from the incident particle onto the target particle based on their mass and the scattering angle. It should be

remembered that the collision is considered elastic and the particles are approximated as hard-spheres.

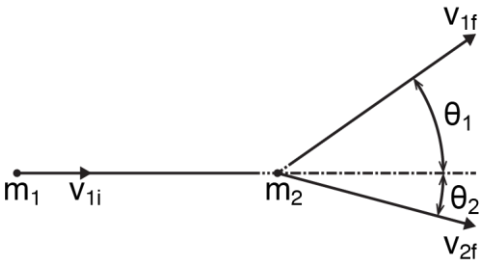

Figure 17. Simplified schematic diagram of an elastic collision of two particles. The impact parameter *b* is not shown (see Figure 16).

Apart from the hard-sphere approximation to particle scattering described above, there are other mechanisms (e.g., potential scattering—Coulomb, polarization), which are not covered in the thesis.

2.2.2.3 Inelastic collisions

The most basic definition of an inelastic collision is that the kinetic energy is not conserved during the collision. It means that some other mechanisms are responsible for redistribution of the total energy. In the following, it is assumed that the reader is familiar with both the classical model of an atom as well as the quantum mechanical specifics.

Let us start with the easiest inelastic mechanism to lose energy by the means of electric dipole radiation. During a collision, atoms in ground states can get excited to higher energy levels. The excess energy can be subsequently released in the form of a photon with a wavelength corresponding to the energy difference between the excited bound state and either a lower lying bound state or a ground state. The process, where A and B could be representing atoms or electrons, can be described as

$$A + B \rightarrow A^* + B \rightarrow A + B + \hbar\omega$$

where $\hbar\omega$ is the photon energy, with ω being its angular frequency. For such a collision, based on the characteristic timescales, an excited atom gets de-excited by a dipole radiation rather than in a collision.

Another inelastic mechanism is the electron–atom ionization proposed by Thomson. In classical sense, an electron with the kinetic energy $mv^2/2$ transfers an amount equal to ionization energy onto a valence electron. The process can be described as

$$e + A \rightarrow 2e + A^+ .$$

An ion–atom collision can result in an exchange of charge. The ion has a chance of grabbing the atom's valence electron, neutralizing itself and ionizing the atom. If the atoms are not the same, the energy levels for the valence levels participating in the exchange will differ and the kinetic energy for the collision will not be conserved. We can write it as

$$A^+ + B \rightarrow A + B^+ .$$

If $A = B$, the process is said to be resonant and the kinetic energy is conserved.

So far, we have been talking about simple inter atomic–particle collisions. Molecular collisions expand the complexity of possible collision schemes twofold. First, molecular bound states can be excited to molecular repulsive states, which—depending upon the transition times—may end up in molecular dissociation, change of a rotational state of motion, or photon emission. Second, molecules possessing additional degrees of freedom may get excited vibrationally or rotationally. Also the transfer of excitation in molecules is possible, whether it is a transfer of electronic, rotational, or vibrational excitation, if the potential energy curves cross or (nearly) touch for specific nuclear separation.

Again, paraphrasing Lieberman, the following example illustrates some inelastic electron collision phenomena in molecular hydrogen. In order of increasing electron impact energy, at a threshold energy of ~8.8 eV, there is excitation to the repulsive $^3\Sigma_u^+$ state followed by a dissociation into two fast H fragments each possessing ~2.2 eV. At 11.8 eV, there is excitation to the $^3\Sigma_g^+$ bound state, followed by electric dipole radiation to the

$^3\Sigma_u^+$ repulsive state, followed by dissociation leaving each atom with energy ~2.2 eV. At 15.4 eV, the $^2\Sigma_g^+$ ground state of H_2^+ is excited, leading to the production of H_2^+ ions. At 28 eV, the excitation of the repulsive $^2\Sigma_u^+$ state of H_2^+ leads to the dissociative ionization of the ion (resulting H and H^+ fragments possess ~5 eV each).

2.2.3 Simulation of the cascade of collisions

To explore the technical details of the HHIC design and to better understand the notion of efficiency of generating a high flux of hyperthermal hydrogen projectiles, a Monte Carlo (MC) approach was used to simulate the cascade of collisions taking place in the drift zone. Resulting from the MC simulation are typical yields* of hyperthermal H_2 projectiles as a function of pressure (the pressures of major interest range from 0.5 mTorr to 1.5 mTorr) in the drift zone and the energy of the H_2 projectiles at the drift zone exit, which are shown in Figure 18(left). The results indicate that there is an optimal pressure where the yield reaches a maximum. For example, the best yield of H_2 projectiles capable of breaking C–H bonds can be found near a H_2 pressure of ~0.5 mTorr for 100 eV H^+ entering the drift zone of 50 cm in length. The shape of a yield curve is consistent with the expected behaviour for collisions in gas phase driven by an energetic particle. At low pressures, the inelastic mean-free path is too long to let the initiators collide with the neutral hydrogen molecules and to generate a high number of energetic neutrals—the yield rises from a low value. In contrast, at the opposite end of the pressure spectrum, the number of collisions is high enough to drive the average KE energy of energetic neutrals bellow a minimum energy necessary for cleaving of C–H bonds—the yield eventually vanishes.

Figure 18(right) provides snap-shots of a typical MC simulation showing a time evolution of the cascade of collisions as initiated by one particle. The green balls represent projectiles, which has undergone collisions and their KE dropped below 19 eV, a threshold energy required to break C–H bonds. The red balls symbolize those projectiles that reached the drift zone exit and retained at least 19 eV.

* The yield is defined here as a number of particles generated by one initiating H^+ particle (initiator) and exiting the drift zone with at least 5 eV of kinetic energy.

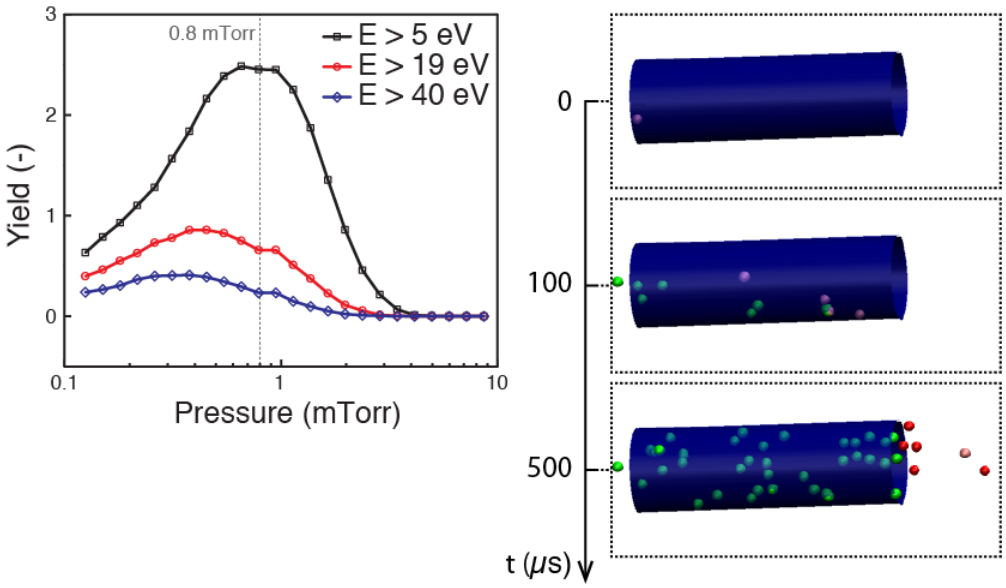

Figure 18. Modeling of HHIC production: (left) the number of H_2 projectiles per incident particle having energies higher than 5, 19, and 40 eV, the dashed line denotes the typical operational pressure of 0.8 mTorr; (b) Monte Carlo simulations of time evolution of a gas-phase (293 K, 1 mTorr) cascade of collisions in a drift zone (blue tube) initiated by a 100 eV H^+ projectile. The H_2 projectiles with energies $E > 19$ eV are shown in red, those with $E < 19$ eV are shown in green, and the background gas particles not participating in the collision cascade are not shown.

It is also interesting to study the HHIC efficiency at higher accelerating voltages. Figure 19 shows yields as a function of pressure for three accelerating voltages. It is not surprising that at constant pressure and increasing accelerating voltage, the yield of projectiles capable of hydrogen abstraction grows. It is also obvious that the yield maximum shifts up to higher pressures when the accelerating voltage is raised.

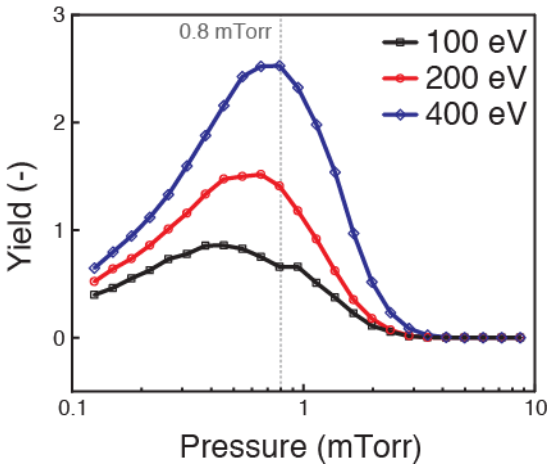

Figure 19. Number of H_2 projectiles per incident particle having sufficient energy to break C–H bonds (> 19 eV). The parameter is the energy of H^+ initiators as given by the accelerating potential.

The details of the MC simulation follow. The program was written in C++ to allow for easier future modifications and enhancements. The model implements a simple Monte Carlo (MC) scheme for a collision cascade of hyperthermal hydrogen ions and neutral hydrogen molecules represented as hard-sphere particles of mass $m = 2$ amu and a diameter $d = 2.92$ Å (as represented by Bird, 1998) in a cylindrical chamber of length $L = 0.5$ m (the x coordinate is the cylinder axis) and diameter $D = 0.15$ m (y and z coordinates). A series of normally and uniformly distributed random numbers $u_i \in (0,1), i = 1\text{–}5$ is used in the following procedure. The initiator, in other words a hyper-thermal particle with energy $E = 50..400$ eV and a velocity vector aligned along x, enters the chamber at the coordinate [0, $D\sqrt{u_1}\sin(2\pi u_2)$, $D\sqrt{u_1}\cos(2\pi u_2)$] and experiences a collision with a background gas molecule (not simulated explicitly) after having moved a distance l drawn from the exponential distribution $l = -\lambda \ln(u_3)$, where $\lambda = 1/n\sigma$ is the inelastic mean free path, $\sigma = \pi d^2$ is the hard sphere cross-section, and $n = p/kT$ is the density of the background gas at pressure p and temperature T = 293 K. This process does not simply result in a doubling of the number of energetic particles, but instead every collision increases the number of energetic particles by 1 if, and only if, the collision leaves both particles energetic enough to continue on. The process is then repeated for the subsequent generations of particles and a cascade of collisions is thus

achieved. Collisions with walls are simply modelled as elastic and do not allow for neutralization of the initiator. The impact parameter $b = d\sqrt{u_4}$ and the azimuthal angle $\phi = 2\pi u_5$ are initiated randomly for every collision to render a uniform distribution of target particle centres in a circle of diameter $2d$. All collisions (including the collisions with the walls of the chamber) are perfectly elastic and specular (momentum transfer occurs only in the direction normal to the collision surface). Those particles whose energy falls below $E < E_{cut} = 5$ eV during the collision cascade, are deemed frozen and discarded—no longer participate in the collision cascade. All other particles with $E > E_{cut}$ that reach the reaction zone at $x = L$, i.e., the energetic projectiles, are counted towards the final distribution. The initiator particle is also discarded if it reaches the reaction zone uncollided. The time is not explicitly included in the model, although it can be calculated. A yield is then defined as the number of projectiles with the energy greater than the E_{cut}, produced per one initiator particle. Typically, we use 10 000 initiating particles to gather the statistics. The simple collision process described above results in a scale-free fragmentation of the incident energy and thus produces the power-law energy distributions for the projectiles.

The simplicity of the model, which neglects many possible collision schemes both elastic and inelastic and thus provides only qualitative description, does not prohibit the use of the results for finding the best conditions for the operation of the HHIC reactor. Indeed, the successful experiments presented in the next chapters were based on the conditions as obtained from the MC simulation taking into account physical limitations of the system.

2.2.4 Hydrogen abstraction

In the previous sections we have shown the evolution of hyperthermal projectiles, which originated in plasma in the form of ions and were extracted through an applied potential into a drift zone, where they collided with background gas molecules to yield neutral, fast moving particles. The following paragraphs will tackle the core of the HHIC method, which is the ability to cleave C–H bonds in a purely physical way, without the presence of chemical reagents. It will be shown that it is indeed possible to excise hydrogen atom from a C–H bond by means of transferring mechanical energy to the target hydrogen atom. Based on the fact that bond strengths of C–H and C–C are nearly identical, one

might wonder why the HHIC method preferentially cleaves C–H over C–C. To answer this question and to evaluate the uniqueness of the HHIC method, ab initio molecular dynamics simulation and semi-empirical estimation techniques were employed. The mechanism of hydrogen abstraction using molecular hydrogen is schematically shown in Figure 20.

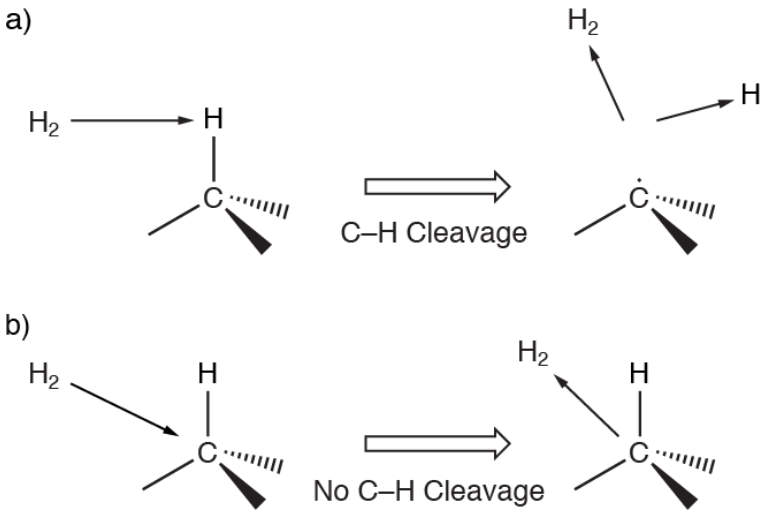

Figure 20. Schematic diagram of hydrogen abstraction as induced by hyperthermal H_2. (a) H_2 hitting H of a C–H bond, possessing enough kinetic energy to break the bond and knocking H off of the molecule; (b) H_2 hitting C of a C–H bond, ineffectively transferring some of its kinetic energy to the methane molecule and bouncing off of it.

2.2.4.1 Ab initio molecular dynamics calculation

To better understand the hydrogen abstraction mechanism by molecular hydrogen on the atomic level, a simulation of the collision process was performed using the ab initio molecular dynamics (MD) method (Payne et al., 1992).

The basic concept of preferentially cleaving C–H bonds with hyperthermal (Jacobs, 2002) H_2 is depicted in Figure 20 and validated with the ab initio MD computations shown in Figures 21 and 22. It translates the intuitive assumption of effective kinematic energy transfer as presented earlier into a useful reaction for the excision of a H atom from a C–H bond without breaking other bonds. More specifically, the computational

results show that when the H_2 projectile possesses a KE of ~19 eV, it knocks the H atom of the C–H bond off and a carbon radical is generated. Under the same conditions, when the projectile impacts at the C atom (or any other atom which is typically much heavier than H_2), the kinematic energy transfer is ineffective and the projectile cannot knock the target atom off and therefore no bond is cleaved.

The computation clarifies that when hyperthermal H_2 collides with C_2H_6, a hydrogen atom is excised from C_2H_6 through a direct recoiling mechanism (Rabalais, 1990; Rodriguez et al., 2007). Figure 21 shows computational results of ab initio MD modelling cleavage of the C–H bond of C_2H_6 by 19 eV H_2 with the molecular axis of H_2 perpendicular to the axis of the H–C bond of C_2H_6. The plot on the right shows the evolution of potential energy of the C_2H_6 molecule. The C_2H_6 molecule eventually becomes C_2H_5. As expected, both the H_2 projectile and the C_2H_6 are vibrationally and rotationally excited during the collision. In addition, the H_2 projectile does not dissociate in this example, hence, although it is not a hard-sphere projectile, it does function well as a recoiling agent. In comparison, when the projectile hits the carbon atom of C_2H_6, the ethane target remains intact even for H_2 with a kinetic energy of 39 eV (Figure 22[*]) due to the ineffective energy transfer for the collision of $H_2 \rightarrow C$. The threshold for C–C cleavage was found to be 40 eV. In short, these and other computational results indicate that preferential C–H cleavage without breaking other bonds is possible. Furthermore, the computational and experimental results also indicate that when H_2 is replaced by any heavier projectile such as He, the selectivity for preferentially breaking C–H bonds is lost. This is because these heavier projectiles can no longer differentiate hydrogen atoms from other target atoms by their mass (as detailed below).

Although the computational results for hydrogen abstraction by molecular hydrogen in the case of a C_2H_6 molecule suggest threshold energy of 19 eV, the threshold is expected to drop when the C–H bond is part of a saturated hydrocarbon segment of a solid. The reason is that the carbon atom of the C–H bond in solid is fixed more rigidly than that of an isolated C_2H_6 molecule, thus the energy loss of the projectile to the "carbon substrate"

[*] Note: the respective views of $H_{\#4}$ and $H_{\#7}$ are blocked by $H_{\#5}$ and $H_{\#8}$.

is reduced. This assumption was proven correct by an ab initio MD simulation, where the carbon atom $C_{\#2}$ was set to be infinitely massive to better simulate the organic matrix. The energy threshold was found to be 8 eV, which is 3 eV more than the C–H bond dissociation energy.

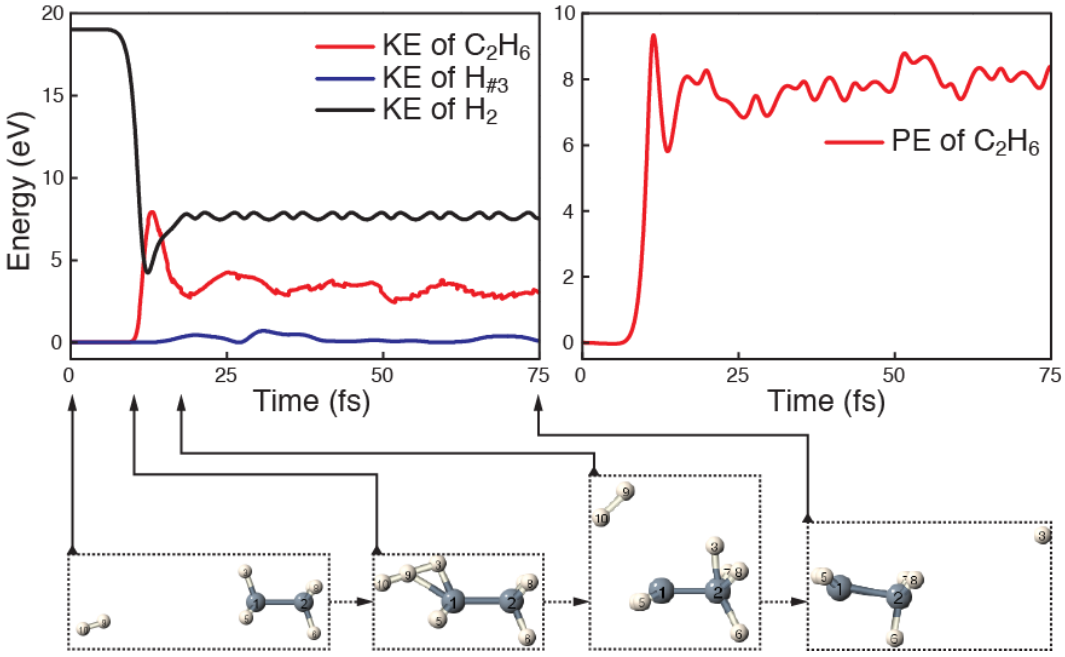

Figure 21. Computational results of ab initio MD showing cleavage of the C–H bond of C_2H_6 by 19 eV H_2 with the molecular axis of H_2 perpendicular to the axis of the H–C bond of C_2H_6 (note: the respective views of H#4 and H#7 of C_2H_6 are blocked by H#5 and H#8). The plot on the right shows the evolution of potential energy of the C_2H_6 molecule. The C_2H_6 molecule eventually becomes C_2H_5.

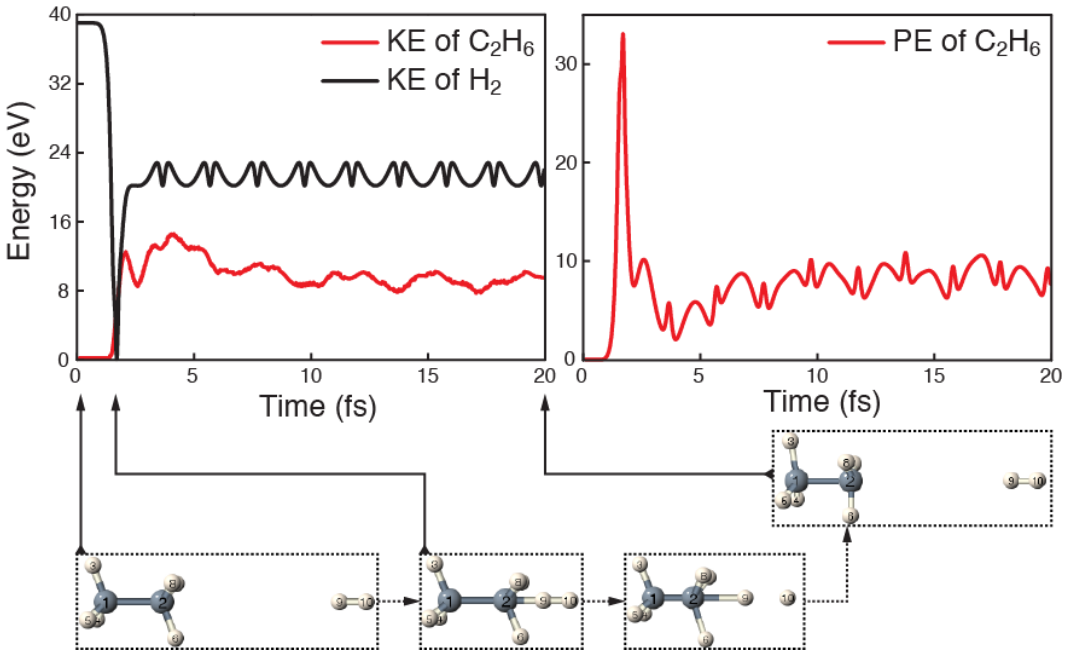

Figure 22. Computational results of ab initio MD of 39 eV H_2 arriving with its molecular axis along the $C_{\#1}$–$C_{\#2}$ bond axis of C_2H_6 and with $H_{\#9}$ of H_2 hitting $C_{\#2}$ of C_2H_6 (the respective views of $H_{\#4}$ and $H_{\#7}$ are blocked by $H_{\#5}$ and $H_{\#8}$). After the collision, the H_2 is scattered with a loss of about 18 eV in kinetic energy (44% energy transfer) and a very small gain in vibrational and rotational energy. The C_2H_6 suffers no bond cleavage, with about 9 eV gain in kinetic energy and some gain in rotational and vibrational energy. The plot on the right shows the evolution of potential energy of the C_2H_6 molecule.

For clarity, it should be noted that the MD simulation used a microcanonical* ensemble and was carried out by integrating the classical Newton's equations of motion using the Verlet algorithm (Verlet, 1967). The time step has been set to 0.05 fs. At each time step, electronic energy and all forces were calculated using the hybrid Density Functional method with the exchange-correlation function B3LYP and within the 6–31G* basis (Becke, 1993) using the Gaussian 03 package (Frisch et al., 2003). The forces acting on each atom were then used for the integration of equations of motion.

* The number of particles and volume does not change, and the total mechanical energy is conserved.

2.2.4.2 The C–H versus C–C bond cleavage

The simplest formula for the energy transfer between two elastically colliding particles in first-order approximation is given by Equation 1. For head-on elastic collisions between hard-sphere particles having mass m_j and energy $KE_{ji/f}$ (i stands for initial, f for final) the fraction coefficient ε of the exchanged energy is

$$\varepsilon = \frac{KE_{2f}}{KE_{1i}} = \frac{4m_1m_2}{(m_1+m_2)^2} .$$

According to this formula, the fraction coefficient for a H_2–H collision is $\varepsilon = 0.89$ and for a H_2–C collision is $\varepsilon = 0.49$ respectively. Consequently, since the energy transfer is more efficient for H_2 colliding with H, than for the collisions with carbon, there is in principle an opportunity for HHIC to do selective hydrogen abstraction. However, in the case of HHIC, the mass m_1 is likely less than 2 a.m.u. and the mass m_2 is likely more than 1 a.m.u.

It is important to know whether hydrogen abstraction could be done using different gases. Let's have a look at the next closest (in mass), readily available element—helium. In contrast, the fraction coefficients for helium based collisions are: a) $\varepsilon = 0.64$ for a He–H collision, and b) $\varepsilon = 0.75$ for a He–C collision. Since the latter figure is greater than the former, the possibility to do hydrogen abstraction with helium is hindered in principle as C–C bonds are on average more likely to break than C–H bonds. It is possible to do HHeIC, but massive fragmentation of organic chains occurs and the selectivity towards chemical functionalities is lost, rendering this approach useless. However, helium as a noble gas does not drive any undesirable side reactions.

The ab initio simulations presented earlier have provided us with the thresholds energies for breaking the C–H (19 eV) and C–C (40 eV) bonds by molecular hydrogen projectiles. However, these figures were obtained for the molecule of ethane, C_2H_6, which has a finite mass, and they have to be corrected (decreased) for the case when the target atoms are part of a surface (which can be seen as infinitely heavy on the atomic mass scale).

Indeed, from Figure 21 it is evident that when the initial kinetic energy of the H_2 projectile is 19 eV, the energy transferred to the ethane molecule (=11 eV) is divided into 3 eV of kinetic energy and 8 eV of internal energy (traces labelled "KE of C_2H_6" and "PE of C_2H_6", respectively). A part of this total internal energy is responsible for breaking the C–H bond, which has nominal bond strength of 4.5 eV, because the "KE of C_2H_6" represents a motion of the centre of mass. However, the total internal energy of the ethane molecule is only a sum of the individual rotational and vibrational modes of the elementary pairs (and higher fragments). It is therefore necessary to take into account the exact spatial orientation and time evolution of the displacement vectors. Incidentally, about the same energy (8 eV) needs to be transferred to a C_2H_6 molecule in order to break a C–C bond (its bonding energy is close to that of the C–H bond). A situation reflecting the onset of breaking of a C–C bond is shown in Figure 22, where the initial kinetic energy of H_2 projectile is 39 eV (just below the estimated threshold of 40 eV needed for cleaving a C–C bond). In this case, 18 eV is transferred to the C_2H_6 with 10 eV in kinetic energy and 8 eV in internal energy (traces labelled "KE of C_2H_6" and "PE of C_2H_6").

Even this limited set of data allows us to adjust the initial estimations for the C–H and C–C cleavage thresholds toward lower values. As mentioned before, the transfer of energy from the incident particle to the centre of mass of a hydrocarbon segment, which is a part of a bulk material, is negligible and is estimated to lower the cleavage threshold by the portion of energy stored in the translational form of an unconstrained ethane molecule (as shown in Figures 21 and 22, 3 eV and 10 eV, respectively). If we also assume that under the most favourable conditions (i.e., maximal impact parameter relative to the bond axis), the minimal transferred energy needed to cleave both C–H and C–C bonds is given by the total internal energy of ~8 eV, one can estimate the corresponding thresholds for the kinetic energy of the incident particle as ~9 eV and ~16 eV, respectively. Since there is a significant disagreement between different estimations and a more thorough modelling would be required (MD simulations for various impact parameters as well as longer organic chains of different conformities), all projectiles with energies falling in the interval of 5 to 40 eV are considered capable of preferentially breaking C–H bonds.

2.2.4.3 Reaction rates and reaction collision cross-sections

Another aspect of the HHIC technique is the rate at which hyperthermal hydrogen molecules break C–H bonds. It is also interesting to compare the rates for molecular and atomic hydrogen. In the following paragraphs, the calculations for the reaction rate and reaction collision cross-section for HHIC will be shown and compared with the corresponding quantities for hydrogen abstraction by atomic hydrogen (Sandreczki et al., 1990).

For an organic polymer of approximate volume density $1\ \mathrm{g\ cm^{-3}}$ and an average CH_2 composition (variation of the proportion of H does not significantly change the estimations below) the volume density of C atoms ($[\mathrm{C}]$) can be estimated as $\sim 4.3 \times 10^{22}\ \mathrm{cm^{-3}}$ and the corresponding area density as $\sim 4.3 \times 10^{16}\ \mathrm{cm^{-2}}$ for a 10-nm-thick polymeric layer.

Let us first consider the experiment (Sandreczki et al., 1990), where an organic polymer has been cross-linked with the help of atomic hydrogen gas. The reaction of the abstraction of H from such polymer by an atomic hydrogen can be symbolically described as follows, $\dot{\mathrm{H}} + \mathrm{HCR} \rightarrow \dot{\mathrm{C}}\mathrm{R} + \mathrm{H_2}$ where $\dot{}$ (a dot above a letter) denotes a radical, and *R* represents the rest of a polymer. This gives the reaction law

$$-\frac{d[\mathrm{C}]}{dt} = \frac{d[\dot{\mathrm{C}}]}{dt} = k[\mathrm{H}][\mathrm{C}] = k'[\mathrm{C}]$$

where $[\mathrm{C}]$ can be expressed in either volume or area units. The absolute rate of the production of C radicals, $d[\dot{\mathrm{C}}]/dt$, can be estimated as

$$\frac{d[\dot{\mathrm{C}}]}{dt} \approx \frac{1 \times 10^{14}\ \mathrm{cm^{-2}}}{100\ \mathrm{s}} = 1 \times 10^{12}\ \mathrm{cm^{-2}s^{-1}}$$

and the relatively high concentration of hydrogen atoms in the experiment is $[\mathrm{H}] \approx 1 \times 10^{15}\ \mathrm{cm^{-3}}$. Therefore, the reaction rates are $k' = k[\mathrm{H}] \approx 2.3 \times 10^{-5}\ \mathrm{s^{-1}}$, and

$$k_{\mathrm{ref}} \approx 2.3 \times 20^{-20}\ \mathrm{cm^{-3}s^{-1}} \qquad (2)$$

where we denoted the reaction rate in the literature reference (Sandreczki et al., 1990) with the subscript "ref", as it is used as a reference value below.

By contrast, in the HHIC setup presented in this work, the concentration of the H_2 projectiles ($[H_2]$) is some 7 orders of magnitude lower (compared to the $[H]$ quantity above). Indeed, at the H^+ plasma current of 10 mA, and other typical experimental conditions (as will be described in the following chapter), the typical flux of H_2 projectiles with energies in the range of 5–40 eV is $j_{H_2} \approx 7 \times 10^{14}$ cm^{-2}s^{-1}. This, at an average velocity of H_2 molecules, $\langle v \rangle \approx 4.4 \times 10^6$ cm s^{-1} (which would correspond to ~20 eV) gives a H_2 volume density of $[H_2] = j_{H_2}/\langle v \rangle \approx 1.5 \times 10^8$ cm^{-3}.

Nevertheless, the reaction of hydrogen abstraction in the HHIC reactor proceeds roughly 100 times faster, that the one observed by Sandreczki, even for the typical H_2 versus typical H concentrations in both experiments. What is more impressive is that in terms of the reaction rate k, it is some 9 orders of magnitude faster.

Namely, the reaction in HHIC can be describes as $H_2(\text{hyperthermal}) + HCR \rightarrow \dot{C}R + H_2 + H$, which gives the following rate equation

$$-\frac{d[C]}{dt} = \frac{d[\dot{C}]}{dt} = k[H_2][C] = k'[C]$$

where the value for $[C]$ is the same as above (taken for a typical organic layer) while one can estimate the absolute rate of the production of C radicals, $d[\dot{C}]/dt$, as follows. We observe in our experiments, that for a typical flux of the H_2 projectiles $j_{H_2} \approx 7 \times 10^{14}$ cm^{-2}s^{-1}, as indicated above, a ~10 nm-thick layer of $C_{32}H_{66}$ can be cross-linked and rendered completely insoluble in ~10 seconds. Assuming that at least two C–H bonds per $C_{32}H_{66}$ molecule have to be cleaved in order to cross-link all $C_{32}H_{66}$ units into an insoluble film with at least one C–C cross-link per $C_{32}H_{66}$ unit gives

$$\frac{d[\dot{C}]}{dt} \approx \frac{4.3\times10^{16}\ \text{cm}^{-2}}{10\ \text{s}}\frac{2}{32} = 2.7 \times 10^{14}\ \text{cm}^{-2}\text{s}^{-1}$$

Consequently, $k' = k[H_2] \approx 6.2 \times 10^{-3}$ s^{-1}, and

$$k_{\mathrm{HHIC}} \approx 4.2 \times 10^{-11}\ \mathrm{cm^{-3}s^{-1}} \tag{3}$$

More than nine orders of magnitude difference between the rates k in the cases of HHIC given in Equation 3 and the literature case as given by Equation 5 can be explained simply as the temperature difference of the reactants H_2 and Ḣ, respectively. Indeed, the barrier for the Ḣ abstraction $E_a \sim 0.5$ eV (see for example Kerkeni et al., 2006) should be compared to the temperature of hyperthermal H_2 ($kT \sim 20$ eV) and to the room temperature of atomic Ḣ ($kT \sim 0.025$ eV), in order to give the corresponding Boltzmann factors as follows: in the case of HHIC it is given as $\exp(-E_a/kT) \approx 0.97$, and as $\exp(-E_a/kT) \approx 2.1 \times 10^{-9}$ for the case of abstraction by atomic hydrogen. Thus, the HHIC method is efficient simply because the reaction barriers are virtually unnoticeable for the swift hyperthermal projectiles.

The high efficiency of HHIC can be further clarified with some relevant collisional data. First, the HHIC is typically applied to precursor molecules present in solid state with an atomic area density of one atom per ~5 $\mathrm{Å}^2$ per atomic layer equivalent. Second, although the cross-section of dissociative collision between H_2 and hydrocarbon is not known, once the rate of reaction k is known one can also estimate the corresponding reaction collision cross-section. For the simple hard-spheres collision model of a gas phase reaction one obtains for the reaction rate k (see for example Levine, 2002):

$$k = \sigma \langle v \rangle e^{-\frac{E_a}{kT}} \tag{4}$$

where $\langle v \rangle$ is an average velocity between the colliding particles and σ is the reaction collision cross-section. Substituting the values for HHIC, obtained above, into this expression one obtains $\sigma \sim 0.1$ A^2.

Note that the cross-section of the dissociative collision of $\mathrm{He}+\mathrm{H_2}$ is ~0.07 $\mathrm{Å}^2$ at 10 eV (Sakimoto, 2000) and that of $\dot{\mathrm{H}} + \mathrm{CH_4}$ at 1.6 eV is 1.5 $\mathrm{Å}^2$ (Germann et al., 1992), hence our estimation above is reasonable. It means that a hyperthermal H_2 projectile will penetrate the subsurface region and undergoes multiple scattering events in the top layer of a few nanometers before it loses enough energy and becomes non-reactive. In some of

these scattering events in addition to direct collision-induced C–H dissociation, C–H bond cleavage can also proceed via hydrogen abstraction by atomic hydrogen generated due to the dissociation of H_2 during collision. Since C–H dissociation via hydrogen abstraction is thermodynamically allowed with only a small energy barrier $E_a \sim 0.5$ eV (Kerkeni et al., 2006), C–H dissociation by hyperthermal atomic hydrogen can readily proceed even without any additional supply of thermal energy. This reaction channel, referred to as collision-assisted hydrogen abstraction, can effectively enhance the C–H dissociation yield, which is also supported by the high cross-section of hydrogen abstraction from hydrocarbon with hyperthermal atomic hydrogen (Germann et al., 1992).

2.2.4.4 Conclusion

The ab initio MD calculations have confirmed our assumption that a hyperthermal hydrogen projectile transfers its total mechanical energy most efficiently to H in a C–H with a probability of causing preferential cleavage of a C–H bond. Although the model uses the simple ethane molecule and thus does not well represent an organic bulk material, data obtained by setting one carbon infinitely heavy provided some insight into the behaviour of real material.

Atomic hydrogen is known to cause hydrogen abstraction so it was prudent to compare reaction rates for hyperthermal hydrogen molecule and atomic hydrogen. The result yields a staggering 9 orders of magnitude difference in favor of the HHIC method.

2.3 Energy measurements

The most important question facing the HHIC method in terms of experimental utility is whether it indeed delivers hyperthermal neutral particles of necessary energy to a sample. It also poses a question of how many such particles are supplied to the sample per unit time or during the bombardment. It is therefore necessary to map the energy distribution of these particles and to confirm that the proposed model of the inner workings of HHIC is correct. There are many ways how to measure energy distribution of particles and we employed two of them: a modified quadrupole mass spectrometer and a modified Faraday cup detector.

To quantify the total number of particles bombarding a sample over a certain period of time, we define $fluence$ as follows:

$$fluence = yield \cdot \frac{I_{\mathrm{acc}} t}{q\ A} \tag{5}$$

where *yield* is the parameter obtained from the MC simulation as described above, I_{acc} is the extraction current, q is the proton charge, t is the exposure time, and A is the effective area of exposure.

2.3.1 Energy measurements using quadrupole mass spectrometer

A quadrupole mass spectrometer (QMS), also called residual gas analyzer (RGA) for its main application, is one of the simplest mass analyzers. The principle of its operation is based on counting the number of ionized particles after they passed through a quadrupole filter. Only those ions, which have the correct mass-to-charge ratio (m/z) are allowed to pass through. The m/z ratio is determined by the combination of alternate and direct voltages applied across the quadrupole electrodes, which form steady and time varying electric fields. Such a system is schematically depicted in Figure 23[*].

[*] Note: rods comprising a quadrupole system would ideally be made in a shape of hyperbolas (facing the mid-axis), but because it is difficult to machine, simple cylinders are generally used.

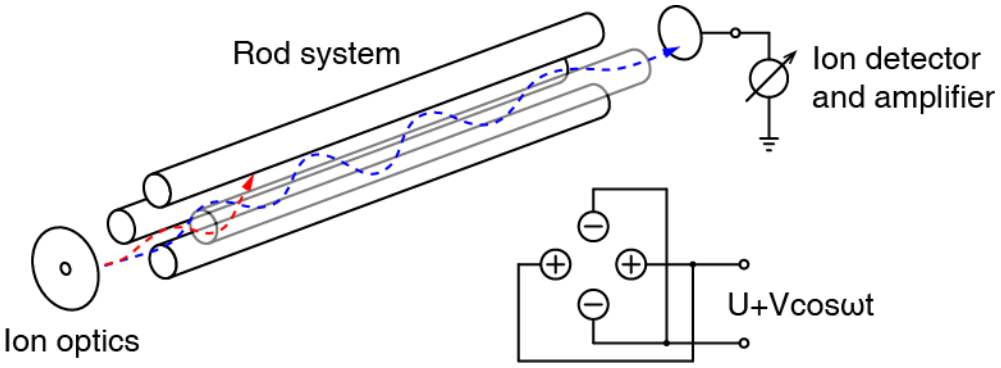

Figure 23. Schematic diagram of a quadrupole mass analyzer. Ion optics is responsible for ionizing (if required), energy filtering (if equipped), and transporting focused ions into the quadrupole rod system. Rods would ideally have a shape of hyperbolas (facing the mid-axis), but because it is difficult to machine, simple cylinders are generally used. Ion detectors usually make use of a Faraday cup or a secondary electron multiplier detector.

The ac voltage rejects or transmits ions according to their m/z ratio by alternately focusing them in different planes. As can be seen in Figure 23, the electrodes are connected in pairs such that the opposite ones share the same polarity of the superimposed ac voltage. During one half of an ac cycle the positive ions are squeezed into the plane parallel to the negatively biased electrodes. During the second half of the cycle the polarity reverses and the ions follow the electric field. The quadrupole field continues to alternate at the same frequency for the duration of collecting ions of a given m/z ratio. Ions thus travel along a complex set of trajectories in a wave-like pattern.

Ultimately, the quadrupole has to act as a band-pass filter. This behaviour is achieved by a clever application of ac and dc potentials along with an ac frequency.

A high-pass filter is realized by a combination of ac frequency and ac voltage establishing a low cut-off condition because the lighter ions are subject to greater acceleration and eventually collide with the electrodes. Heavier ions are free to move through the quadrupole because they do not re-adjust their momentum vectors as quickly as the ac frequency would dictate.

However, there is also a dc voltage applied across the rods. The dc voltage does not affect light ions because they respond much faster to the ac voltage and their trajectories could be thought of as re-focused every time the ac potential changes polarity. On the other hand, the heavier ions follow slowly the dc electric field and thus steadily drift away from the centre of the quadrupole. By the time they cross the rod system, they are too far off-axis to pass through the exit aperture and make it to the detector.

Adjusting, therefore, the magnitudes of the potentials and the frequency, a high-pass and low-pass filters are realized simultaneously to create a window for the transmission of a specific m/z ratio. The analyzer then collects the full mass spectrum by scanning the ac and dc fields. Simply put, the longer the quadrupole the higher the mass the analyzer can differentiate.

Quadrupole mass spectrometers are usually used to measure gas composition in a vacuum chamber. The neutral gas molecules enter the RGA where they get ionized, filtered, and counted. If the QMS is equipped with an ion extractor (a mesh grid) and a lens at the entrance, it can also analyze already ionized particles. When the application requires measuring fast moving atoms or molecules, the RGA has to be modified in order to slow them down to the so-called transfer velocity (usually around 3 eV in KE). Such a modification may consist of inserting a cylindrical energy filter (CEF) between an ionizer and a quadrupole, where the CEF, quadrupole, and SEM detector all float on a variable voltage power supply. This floating voltage presents a potential barrier to the incident ions and effectively acts as a high-pass filter. The CEF—having a solid, circular piece of metal in its center, i.e., on its cylindrical axis of symmetry—then pushes the remaining ions off axis and those with velocities above a cut-off velocity hit the walls and never leave through the exit aperture. This configuration has also another effect of shielding off UV radiation, which is under normal conditions responsible for the generation of low energy ions anywhere inside a QMS distorting the signal. A system capable of all these measurements is shown schematically in Figure 24.

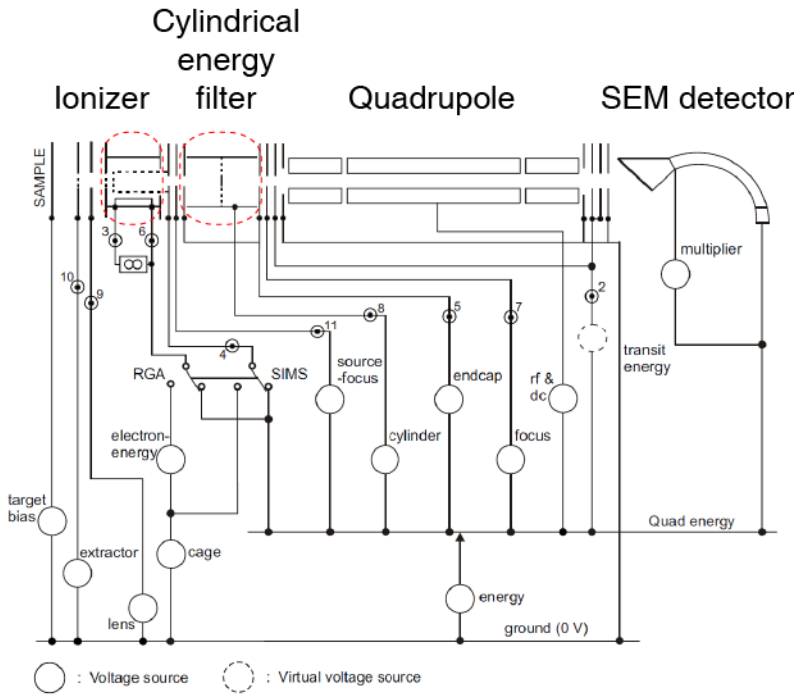

Figure 24. Schematic diagram of SIM300P analyzer including voltage references.

The following section shows how the HHIC reactor had to be modified to accommodate a RGA and what the conditions required for a successful operation are. The section after shows the results of energy distribution of hyperthermal hydrogen neutrals as obtained by the RGA and an explanation as to why the measurements were unsuccessful.

2.3.1.1 Experimental setup

To carry out this experiment, the HHIC reactor was expanded by attaching a Hiden SIM300P analyzer to the bottom of the reaction chamber. Because of the physical dimensions of the QMS and the degree of vacuum required for its operation, a second turbomolecular pump had to be used and mounted onto a tee. The newly created analytical chamber was separated from the reaction chamber by a plate of metal with a small hole in the centre to produce higher vacuum (maximum operating pressure recommended by the manufacturer is 5×10^{-6} Torr. A cross-section of the modified system is shown in Figure 25.

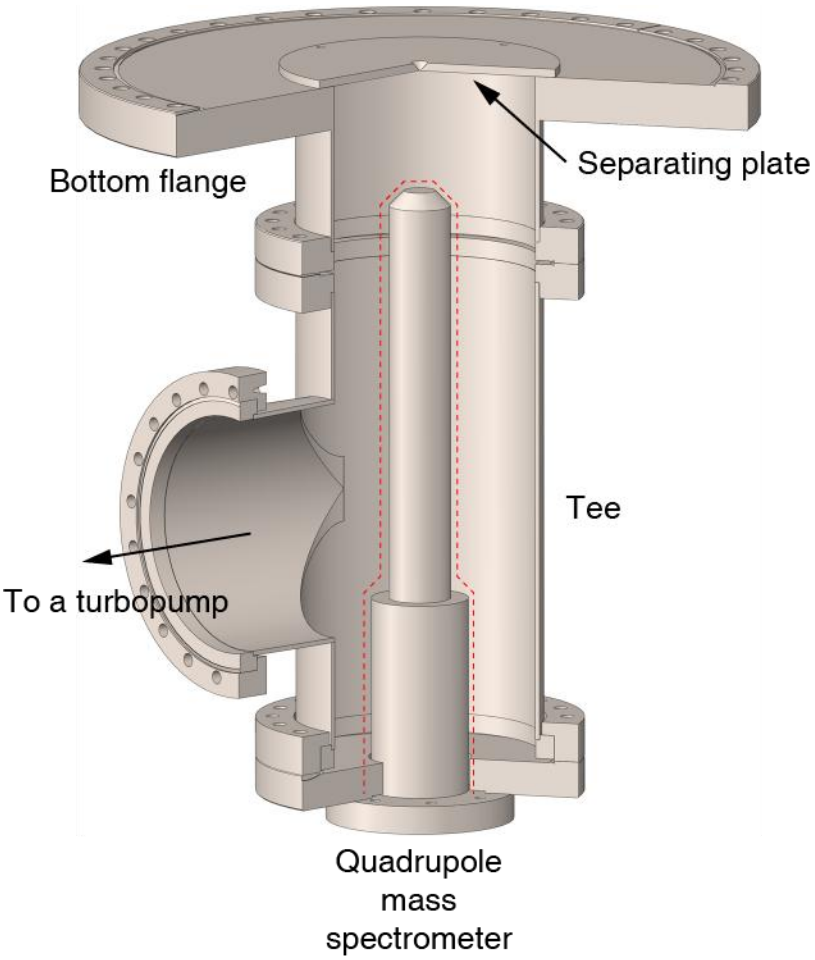

Figure 25. Cross-section of the RGA modification to the HHIC reactor.

Once the RGA is attached to the system, a standard background pressure ($\sim 2 \times 10^{-6}$ Torr is reached. Because there is no load-lock mechanism on the system—the vacuum part of the reactor is always exposed to air when manipulating with samples—it is advisable to let the RGA sit under vacuum for extended period of time (a day in this case) before commencing measurements. The first thing to do, after the RGA is ready, is to let the filament of the ionizer degas for ~10 mins.

To properly set up the RGA it is necessary to run it through an auto tune procedure, which iteratively finds the best combination of the internal voltages (as referenced in Figure 24) to get the highest signal for a specific element. There are also a couple of parameters that need to be adjusted manually, although strictly speaking the tune-up procedure could include every single modifiable parameter. The most important are the

emission current pushed through the filament, electron energy, and a (high) voltage on the secondary electron multiplier detector. When the RGA is set up, a residual background gas is scanned for calibration and referencing.

The results of experiments presented in the following section were collected under the following RGA conditions:

$$I_{em} = 300\ \mu\text{A}$$
$$KE_e = 70\ \text{eV}$$
$$V_{source\ focus} = -17\ \text{V}$$
$$V_{cylinder} = 0.5\ \text{V}$$
$$V_{end\ cap} = -20\ V$$
$$V_{focus} = -37\ \text{V}$$
$$V_{SEM} = 1800\ \text{V}$$
$$V_{energy} = -5\ ..\ 100\ \text{V}$$
$$\text{mass} = 2.15\ \text{amu}$$

where I_{em} is the filament emission current, KE_e is the energy of ionizing electrons, mass is the value, which goes into an m/z ratio, and the rest is referenced in Figure 24.

The HHIC conditions were

$$P_{MW} = 200\ \text{W}$$
$$p = 0.5, 0.8, 1.0, 1.5\ \text{mTorr}$$
$$V_{acc} = -V_{r1} = -50, -100, -200\ \text{V}$$
$$V_{r2} = -50\ \text{V}$$
$$I_{acc} = 50\ \text{mA}$$

where P_{MW} is the input microwave power, p is the operational pressure in the chamber, V_{acc} is the accelerating voltage, V_{r1} and V_{r2} are the retarding voltages repelling residual ions and electrons, respectively, and I_{acc} is the total current drawn from the accelerating electrode.

In this experiment, five pairs of V_{acc}–p were looked at: −50, −100, −200 V at 0.8 mTorr (as the typical pressure used in HHIC applications); and 0.5, 0.8, 1.0, 1.5 mTorr at −50 V For every combination the following steps were undertaken to collect a representative set of data. First, a background gas is scanned to provide for a baseline. Second, hydrogen is introduced inside the reactor and another background scan is taken. Third, the HHIC is turned on and the system is left alone for 1 min to stabilize. Forth and last, four RGA scans with V_{energy} as the parameter are taken, the first one is discarded and the remaining three algebraically averaged.

2.3.1.2 Results and discussion

It is unfortunate to report that the results obtained from this method were unsatisfactory. As can be seen in Figure 26, changing either the reaction chamber pressure between 0.5 and 1.5 mTorr for constant $V_{acc} = -50$ V or the V_{acc} between −50 and −200 at constant $p = 0.8$ mTorr does not affect the position of the peaks. In fact, the only property that changes is the intensity.

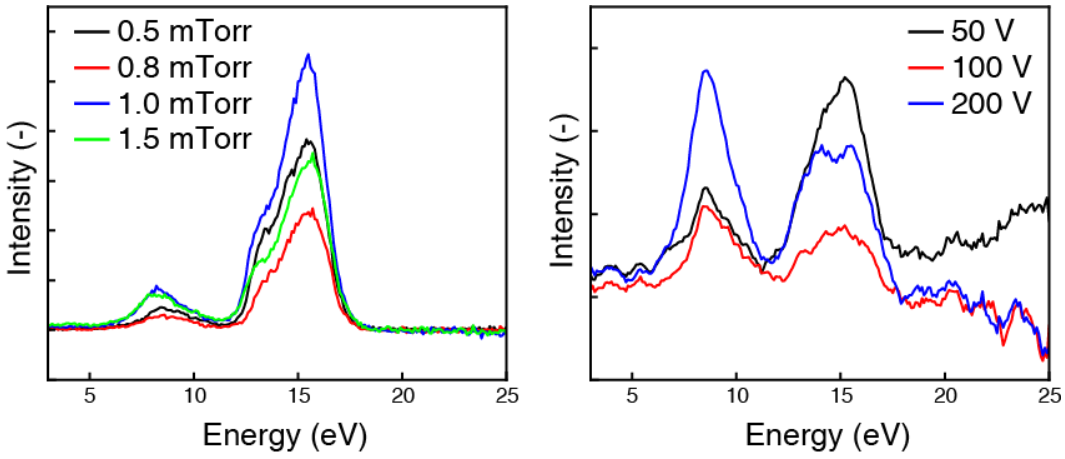

Figure 26. Energy distribution of neutral hydrogen molecules as measured by RGA for a) constant $V_{acc} = -50$ V and four pressures (left), and b) constant $p = 0.8$ mTorr and three accelerating voltages.

This discouraging observation led to a series of steps that were aimed at resolving the issue. It is known that ionizing hyperthermal neutrals can be a difficult task (Ranjan et al., 2006), as the electrons may not have a chance to collide with the fast moving molecules

during the short time they spend inside the ionizer. Therefore, we repeated the experiments for higher emission currents, which did not yield any major improvement. There was no straightforward answer as to why the neutrals generated under different HHIC conditions displayed the same energy distribution. To eliminate the possibility that the QMS cannot handle hyperthermal neutrals, the same experiments were performed operating the QMS in a SIMS (secondary ion mass spectroscopy) mode, where we looked at the energy distribution of ions. Unfortunately, the results were again problematic showing no difference for different HHIC conditions and flat energy distributions. At that point we had to resort to a consultation with the technicians of Hiden Analytical who were very helpful and after going through the provided logs and experimental files they concluded that the method is correct.

Similar RGA setups are commonly used to measure energy distributions of both ions and neutrals so the only explanation could lie in the system configuration. Indeed, running a SIMION® (modelling and simulation computer program created by Dahl, 2000) simulation of the HHIC-QMS configuration revealed that having the entrance to the RGA ~7.5 cm away from the separating plate opening leads to a significant ion beam repulsion across the divide. This in turn smears out all information about ionic energy distribution because only the ions with high energy (and at preferable angles) have a chance to enter the RGA undisturbed. Even for neutrals, the amount that passes through a hole (in the separating plate) at a trajectory compatible with the solid angle of acceptance of the RGA and does not undergo a collision is comparable in magnitude to noise.

2.3.1.3 Conclusion

Although measuring energy distribution of neutral particles using various implementations of mass analyzers is in principle easy, its practical application may not be straightforward. Once the right implementation is chosen, the basic condition is that the system under study has to allow for housing of an analyzer. In the case of HHIC, we realized the need to place the RGA head within a couple of millimetres only after critical examination of collected data and thorough investigation of the working principle of the spectrometer with the given configuration.

In the end, it was concluded that a significant change had to be made to the system to place the RGA closer to the plate opening. Unfortunately, we were unable to complete the necessary steps in time but they will be addressed in the last chapter as a critical part of the evaluation of the HHIC method.

2.3.2 Energy measurements using Faraday cup

Because of the experimental failure of the quadrupole mass spectrometer approach as presented in the previous section, we have decided to obtain an energy distribution of hydrogen ions. It is known that during a HHIC operation charged particles are reflected back into the drift zone, thus effectively prohibited from reaching the sample apart from a) those generated between the sample and the second retarding electrode, and b) the stray ions. Yet in the absence of a direct method to measure distribution of hyperthermal neutrals, measurements based on a Faraday cup (FC) detector were employed to provide supporting evidence for our theoretical framework. It is believed that the correlation between ionic and neutral energy distributions supports this approach as will be elaborated on and discussed later on.

A Faraday cup is a straightforward detector offering a simple way to measure energy distribution of charged particles. Although FCs are readily used to measure both positively and negatively charged particles, in the case of HHIC it is used exclusively for measuring positive ionic hydrogen species. The principle stems from the neutralization of charged particles impinging on a metallic detector, where the net charge gain is measured as electrical current by an ampere meter. However simple the principle seems, the detector must be designed to significantly minimize the two main sources of error: a) the emission of low-energy secondary electrons from the surface struck by the incident charged particle; and b) backscattering of incident particles leaving the detector before neutralization. It should be noted that it is fundamentally impossible to distinguish between a pure electronic current and a virtual current caused by secondary emission.

In the following section, detailed information about the design and working principle of our FC detector will be provided. Results obtained during measurements under representative conditions of HHIC operation will also be shown and discussed.

2.3.2.1 Experimental setup

The design of our home-made FC detector is show in Figure 27. The detector including a bevelled insert is made of copper; the housing, meshes, and ion lenses are made of stainless steel; and the non-conductive separators are made of poly(tetrafluorethylene).

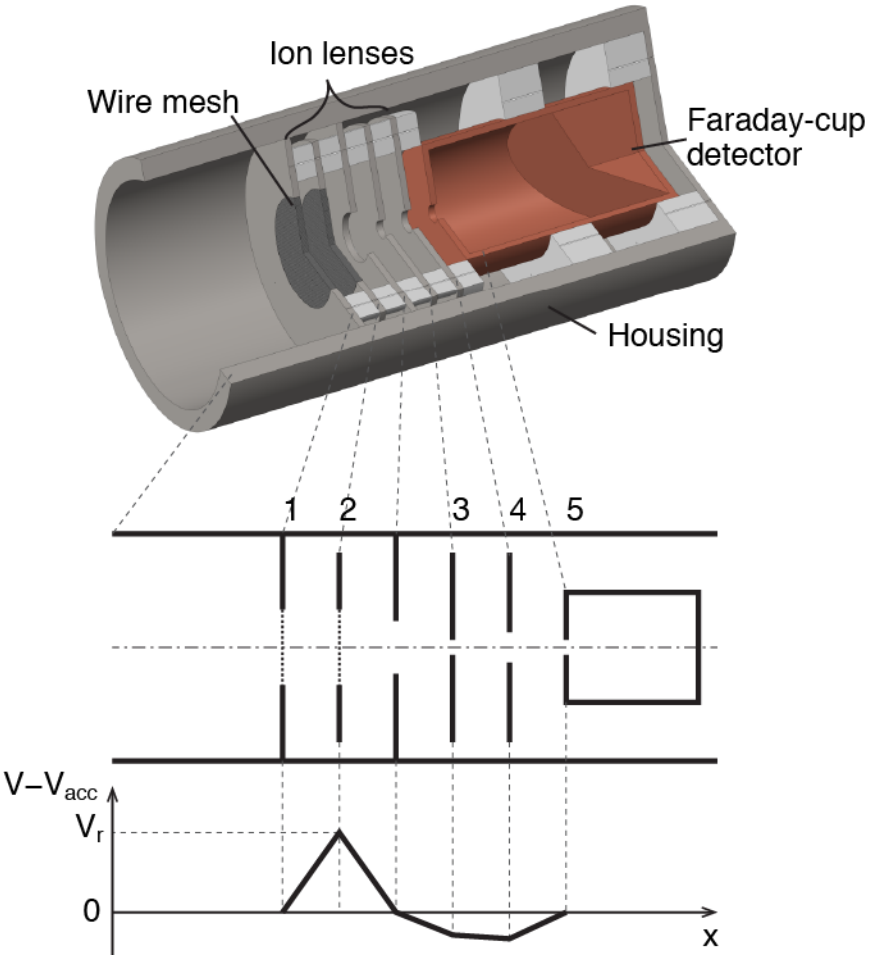

Figure 27. Faraday cup detector with a set of ion lenses and a pair of mesh electrodes for energy discrimination. Below is the typical potential profile.

In designing the FC detector to properly repel, focus, and contain incident ions, SIMION® was used to simulate ion trajectories under the influence of electric field. The electric field is set up by biasing the five electrodes shown in Figure 27 by independent power supplies. Electrode #1 and the electrode between electrodes #2 and #3 are all on the same potential and this potential is the same as the applied accelerating voltage V_{acc}. We could say that the whole FC detector floats on V_{acc}. The reason behind this

configuration of potentials is simple: If the FC (electrode #5) was on a different potential than the ions entering the drift zone, then the FC would, on its own, behave as an energy filter. This is not a desirable behaviour. Rather, electrode #2 sets up a potential barrier V_r with respect to the electrode #1 and repels all ions with energy lower than the magnitude of this barrier. All ions overcoming this potential barrier get focused into the small opening inside the FC detector, where they collide with the bevelled bottom and scatter at an angle pointing into a wall. This minimizes the error of virtual current caused by escaping secondary electrons. The example of SIMION® simulations for ions with energies above and below the potential barrier and coming straight at the detector is shown in Figure 28. Incident ion energies were of 20 eV (top) and 30 eV (bottom) and the potential barrier was $V_r = 20$ eV. The FC is modeled without the bevelled insert because it does not affect the results.

The spatial distribution of ion trajectories that this FC detector accepts is determined by a solid angle ~0.005 sr. For a modified version of the detector, which has not been built yet and is still in drawing form only, the ion lenses are re-designed to better focus the incident ions and the solid angle increases to ~0.08 sr. This parameter, however, does not significantly affect the measurements because it primarily increases the overall number of neutralized ions, i.e., increasing the magnitude of the measured current.

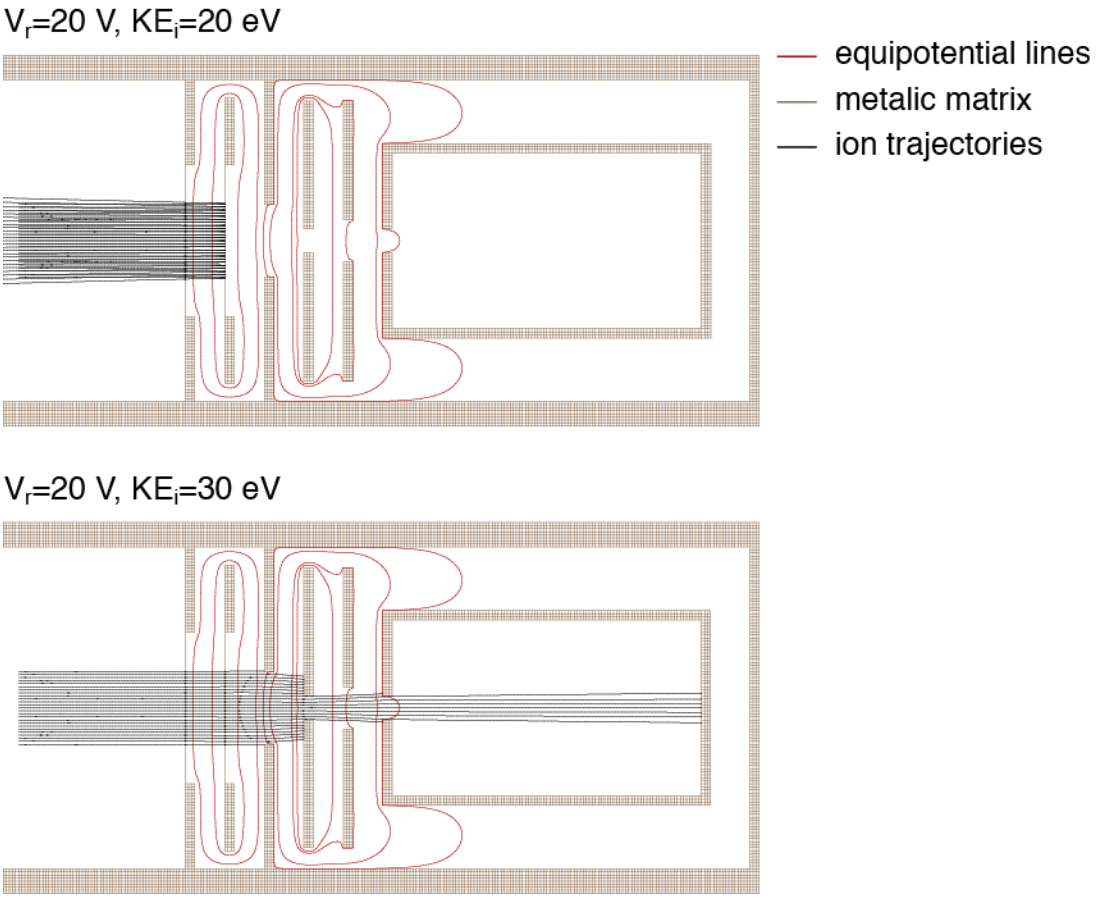

Figure 28. SIMION® simulation of the behaviour of the FC detector for ions with incident energies of 20 (top) and 30 (bottom) eV and the potential barrier V_r of 20 V. The FC is modeled without the bevelled insert because it does not affect the results and is difficult to model in a system of cylindrical symmetry.

From the given example it is evident that there will always be ions that enter the detector (not just the FC) at an angle or trajectory outside the bounds defined by the solid angle of the detector. These ions most likely end up hitting a surface of a lens, a wall, or the FC itself. If these ions give rise to secondary electrons, the electrons may contribute to the measurement error depending upon from which electrode they originated. The equipotential lines are set up such that the only electrodes that could adversely affect (decrease) the FC current if struck by an ion emitting a secondary electron are electrode #4 and the Faraday cup. In the case when the electron originates from the FC its kinetic energy determines whether it will be forced back toward the cup by electrode #4 or it will escape and artificially increase the measured current.

In light of all these facts the following voltages (relative to V_{acc}) were applied to the electrodes (numbered in Figure 27) as:

$$V_1 = V_{housing} = 0,$$
$$V_2 = V_r \in (0,2V_{acc}),$$
$$V_3 = -60,$$
$$V_4 = -30,$$
$$V_5 = V_{FC} = 0.$$

As already mentioned, these voltages were set up by four independent power supplies. One of these power supplies was a built-in voltage source of a Keithley 6517A electrometer, which was also used as an ammeter to measure the FC current.

Measurements were carried out using a home-made computer program written in LabVIEW™ C. The output current values were averaged by the instrument in two stages. In stage one, the FC current was processed by an analog-digital converter with an integration time as the parameter. A digital averaging (and moving) filter was then applied to a set of ten consecutive readings before sending the final value to the PC. To satisfy the time demands of taking such a number of readings per step, the program waits for 2 seconds before taking a reading. Each measurement at every HHIC condition was repeated three times and an algebraic average was taken. As will soon be obvious this amount of averaging was necessary to minimize noise in the data. A voltage step was chosen to be 2.5 V. Voltage step, range of spanned voltages, time step, and number of repetitions had to be considered collectively and adjusted accordingly in order to minimize any potential heating effects associated with prolonged measurement. Current data were differentiated using an OriginPro™ built-in function without any artificial smoothing.

The HHIC conditions were selected to best represent an everyday operation and to provide information about the behaviour of the source of hyperthermal projectiles. The output microwave power was set to 200 W, and the strength of the magnetic field was varied in the range of 86.0–92.0 mT in order to set the accelerating current I_{acc} to 3 mA.

A combination of three pressures (0.5, 0.8, and 1.0 mTorr) and two accelerating voltages (0 and −50 V) was chosen. Other parameters copy those given in Section 2.3.1.1.

The Faraday cup approach to measure energy distribution of charged species has one major advantage over the QMS method. The FC detector is relatively small and can be placed virtually anywhere inside the HHIC reactor. This has allowed us to measure the energy distribution at two different angles (0 and 45°) relative to the vertical, eliminating the effect of uncollided projectiles as well as confirming the isotropic nature of the HHIC method. The three configurations of the detector are shown in Figure 29.

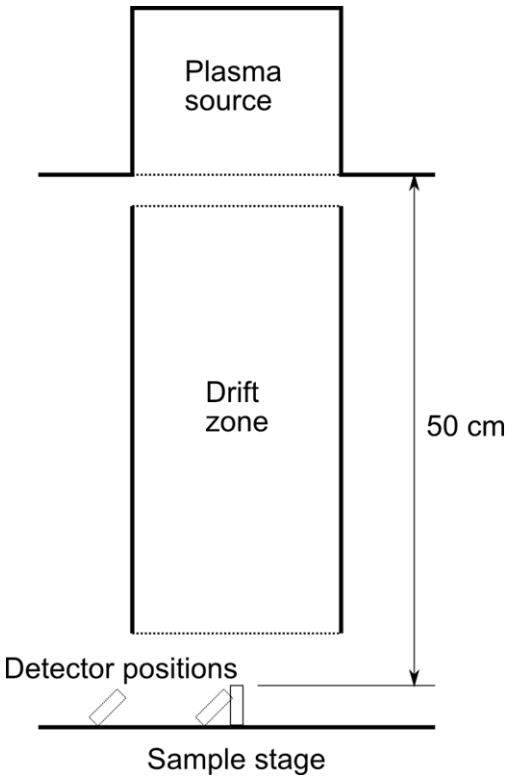

Figure 29. Three positions of the FC detector during measurements: at the centre of the drift zone at 0° and 45°, and at the side of the drift zone out of line-of-sight of plasma at 45° (angles relative to the vertical).

2.3.2.2 Results and discussion

Although measuring energy distribution using a FC detector is not as sensitive as using a secondary electron multiplier, it is highly accurate because of a direct relationship

between the measured current and the number of neutralized ions. In fact, the electric current measured at the detector is given by $I = dQ/dt$, which can be translated into the current scheme as

$$\int Idt = \int_{N_{KE>eV_r}} edN$$

with N being the number of neutralized ions. Because the current is representative of all ions having energy higher than the potential barrier, the resultant current has to be differentiated in order to get the energy distribution of ions.

The following three figures (Figure 30, Figure 32, and Figure 33) show the measured FC current and the corresponding energy distribution for a combination of the parameters provided earlier. As can be seen, the plots of energy distribution are noisy even after significant averaging (as discussed above), which is primarily due to a large fluctuation in the plasma generated ionic flux as well as a small gradient of the FC current (in respective regions). However, the peak positions and trends are still discernible especially considered together.

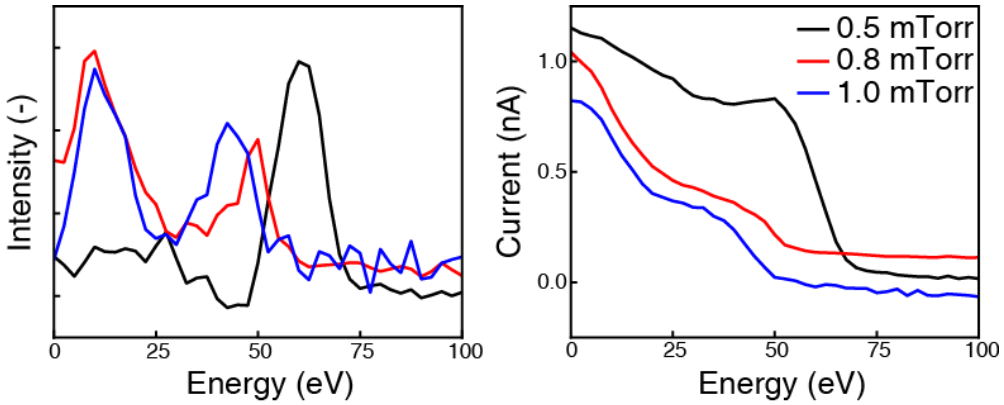

Figure 30. Energy distributions of positive hydrogen ions (left) and the corresponding FC currents (right) as measured for $V_{acc} = 0$ V and three pressures at the centre of the drift zone and 0°.

If we first look at Figure 30, an interesting phenomenon shows up. Although the accelerating voltage was $V_{acc} = 0$ V, the position of main peaks for all three pressures is much higher than one would reasonably expect. Similar results, however, are often found in the literature (see Ono et al., 1986; Matsuoka et al., 1988a; Matsuoka et al., 1988b) as shown in Figure 31.

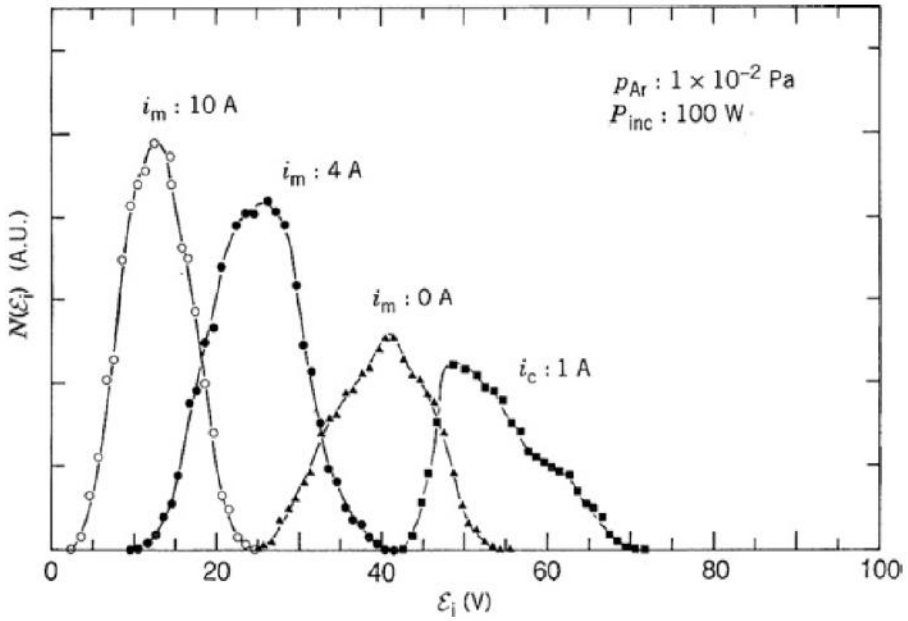

Figure 31. Change of ion energy distribution in the plane of a sample with the sample-level coil current i_m (Matsuoka et al., 1988b). The case of $i_m = 0$ A should be considered.

It would seem that the accelerating voltage is the only source of energy responsible for propelling the extracted ions into the drift zone. Strictly speaking, this is a correct statement, however, the extracted ions are already energetic prior to their extraction. They acquire their kinetic energy in plasma through direct mechanisms such as microwave heating (insignificant amount, slightly above thermal energy), collisions with energetic electrons, and plasma drifting. In addition, another source of energy is the plasma potential (through sheath and distributed potential, V_s and V_d, respectively). The kinetic energy is on average given by (Lieberman et al., 2005, p. 511)

$$KE = e(V_d + V_s) + \frac{1}{2}kT_e \, .$$

Numerical simulations of energy distribution of electrons in ECR plasmas (Weng et al., 1992) suggest that for argon plasma induced by microwaves of 150 W and at pressures ≤1 mTorr, the temperature of electrons T_e can increase above 50 eV and the plasma potential up to 40 V. It is therefore reasonable to expect the ions in HHIC to possess energies up to ~60 eV at low pressures. At higher pressures, the energy shifts to lower values as the number of collisions increases.

Applying negative bias to the accelerating electrode shifts the energy spectrum by a given amount to higher energies, as can be seen in Figure 32.

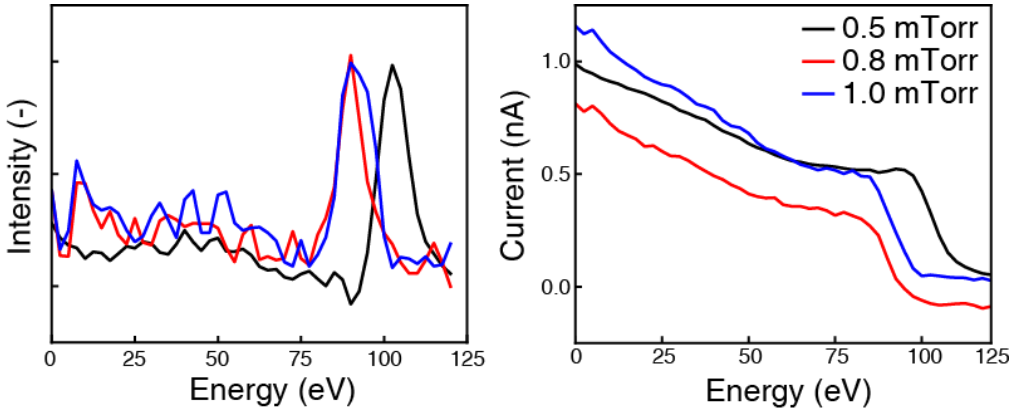

Figure 32. Energy distributions of positive hydrogen ions (left) and the corresponding FC currents (right) as measured for $V_{acc} = -50$ V and three pressures at the centre of the drift zone and 0°.

Concentrating now on the issue of isotropy of the HHIC method, three experiments were carried out with the FC detector placed at two spots and tilted at two angles for the same V_{acc} and pressure. The results are summarized in Figure 33.

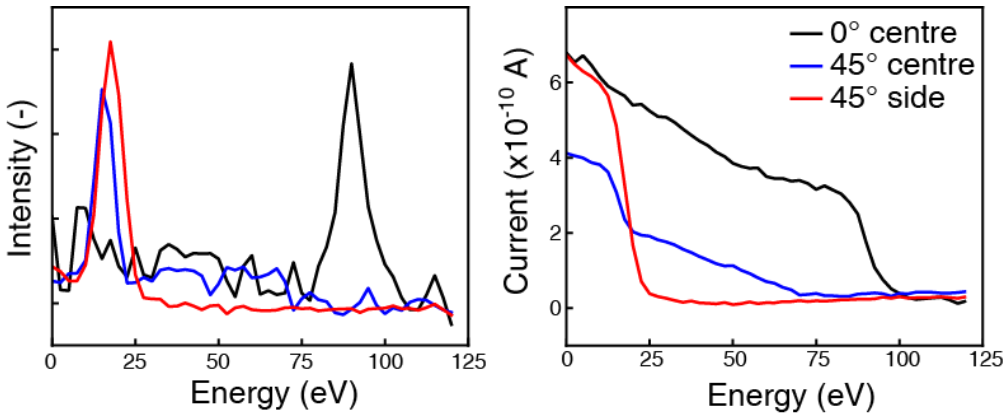

Figure 33. Energy distributions of positive hydrogen ions (left) and the corresponding FC currents (right) as measured at the centre of the drift zone and two angles (0° and 45°), and an edge of the drift zone at 45°, for $V_{acc} = -50$ V and pressure 0.8 mTorr.

With the detector in the centre of the drift zone and tilted at 45° it is evident that the majority of uncollided ions are prohibited from entering the ion lens system as confirmed by the lack of the high-energy peak. In this case, the peak in the energy spectrum corresponds to an average residual energy of ions that underwent a certain number of collisions before entering the detector at a 45-degree angle. It is also apparent that when the detector is moved out of line-of-sight of plasma, to the side of the drift zone, the energy spectrum does not substantially differ from the axial one. This has two implications. First, the effect of energetic electromagnetic radiation on the validity of the data can be ignored. Second, this phenomenon could potentially be exploited in designing experimental configurations where the harmful UV radiation would be screened out by a shade placed above the sample.

Relating these results to the MC simulation provides us with an interesting insight. Comparing energy distributions for the same V_{acc} indicates that little difference exists between 0.8 and 1.0 mTorr. Going back to Figure 18, we might suggest that we found a plateau region of the yield curve or the onset thereof.

The presented results can also be used in a rough way to support the concept of fluence as defined at the beginning of Section 2.3. Let us compare the current densities of ions

extracted from the plasma body (j_{acc}) and those measured by the FC detector (j_{fc}). The areas across which the currents are measured are $A_{acc} = 175$ cm^2 and $A_{fc} = 5 \times 10^{-3}$ cm^2. The $I_{acc} = 3$ mA was given in the Experimental section and the Faraday cup current $I_{fc} = 6 \times 10^{-10}$ A will be taken from a measurement shown in Figure 33(right) for the detector at 0° relative to the vertical. The current densities are

$$j_{acc} = \frac{I_{acc}}{A_{acc}} = \frac{3 \times 10^{-3}}{175} \cong 1.7 \times 10^{-5} \text{ A cm}^{-2}$$

$$j_{fc} = \frac{I_{fc}}{A_{fc}} = \frac{6 \times 10^{-10}}{5 \times 10^{-3}} = 1.2 \times 10^{-7} \text{ A cm}^{-2} .$$

Taking into account the solid angle of the detector j_{fc} becomes $1.2 \times 10^{-7}/0.005 = 2.4 \times 10^{-5}$ A cm^{-2}. The fact that the two current densities are very close justifies the use of Equation 5 for a rough quantification of the degree of sample exposure to hyperthermal hydrogen neutrals even though that the $yield$ factor is represented by a slightly different physical mechanism for the case of ions and neutrals.

One last question remains to be answered. How can we correlate the energy distribution of ions to the energy distribution of neutral particles. If we take into consideration the available collision mechanisms for ions and neutrals as described in Section 2.2.2 we conclude that apart from being affected by electromagnetic fields (the drift zone is an electric field-free region) hydrogen ions and hydrogen molecules collide in gas phase following the same mechanisms. However, there are two fundamental differences, which both pertain to a measurement of energy distribution. First, in order to generate a hyperthermal neutral particle, at least one primary ion must collide with a background gas molecule. Therefore, we expect the energy distribution of hyperthermal neutral particles not to comprise the high-energy peak because the probability of a head-on collision in the solid angle of the detector is low. Second, disregarding uncollided ions, the concentration of neutrals relative to ions is higher because when a neutral collides with a wall or other metallic stationary object, it usually does not ionize while an ion bouncing off a conductive wall does neutralize.

2.3.2.3 Conclusion

In summary, the presented energy distributions of hydrogen ions are consistent with those reported in the literature and provide for better understanding of hyperthermal hydrogen-induced cross-linking. The results show that the ECR hydrogen plasma can on its own generate highly energetic particles. The angle-resolved study shows that these particles indeed undergo a series of collisions after being extracted from the plasma body.

Yet, further experiments have to be conducted in order to conclusively quantify the amount of energetic particles impinging on a sample. In other words, it is desirable to correlate the results obtained by the MC simulations (yields) with those directly measured in the reactor under typical conditions.

References

Bardet, R., Consoli, T. and Geller, R.: 1964, *Physics Letters* **10**, 67-69

Becke, A. D.: 1993, *The Journal of Chemical Physics* **98**, 5648-5652

Bersin, R. L.: 1978, *Solid State Technology* **21**, 117-121

Bird, G. A.: 1998, *Molecular gas dynamics and the direct simulation of gas flows*, Published by Clarendon Press ; Oxford University Press

Boswell, R. W.: 1970, *Physics Letters A* **33**, 457-458

Boswell, R. W. and Porteous, R. K.: 1987, *Applied Physics Letters* **50**, 1130-1132

Chapman, B. N., Hansen, T. A. and Minkiewicz, V. J.: 1980, *Journal of Applied Physics* **51**, 3608-3613

Consoli, T. and Hall, R. B.: 1963, *Nuclear Fusion* **3**, 237-247

Dahl, D. A.: 2000, *SIMION for the personal computer in reflection*

Dandl, R. A., England, A. C., Ard, W. B., Eason, H. O., et al.: 1964, *Nuclear Fusion* **4**, 344-353

Davies, B. and Christia.Pj: 1969, *Plasma Physics* **11**, 987

Devine, R. A. B., Mayberry, C., Kumar, A. and Yang, Y.: 2010, *Ieee Transactions on Nuclear Science* **57**, 3109-3113

Flohr, R. and Piel, A.: 1993, *Physical Review Letters* **70**, 1108-1111

Forster, J. and Holber, W.: 1989, *Journal of Vacuum Science & Technology a-Vacuum Surfaces and Films* **7**, 899-902

Frisch, M. J., Trucks, G. W., Schlegel, H. B., Scuseria, G. E., et al.: 2003, *Gaussian 03, Revision C.02*, Retrieved April 14, 2011, from http://www.gaussian.com

Germann, G. J., Huh, Y. D. and Valentini, J. J.: 1992, *The Journal of Chemical Physics* **96**, 5746-5757

Godyak, V. A., Piejak, R. B. and Alexandrovich, B. M.: 1992, *Physical Review Letters* **68**, 40-43

Gorbatkin, S. M., Berry, L. A. and Roberto, J. B.: 1990, *Journal of Vacuum Science & Technology a-Vacuum Surfaces and Films* **8**, 2893-2899

Hopwood, J., Guarnieri, C. R., Whitehair, S. J. and Cuomo, J. J.: 1993, *Journal of Vacuum Science & Technology a-Vacuum Surfaces and Films* **11**, 147-151

Jacobs, D. C.: 2002, *Annual Review of Physical Chemistry* **53**, 379-407

Keller, J. H., Forster, J. C. and Barnes, M. S.: 1993, *Journal of Vacuum Science & Technology a-Vacuum Surfaces and Films* **11**, 2487-2491

Kerkeni, B. N. and Clary, D. C.: 2006, *Physical Chemistry Chemical Physics* **8**, 917-925

Kosmahl, H. G., Miller, D. B. and Bethke, G. W.: 1967, *Journal of Applied Physics* **38**, 4576-4582

Lee, Y. H., Heidenreich, J. E. and Fortuno, G.: 1989, *Journal of Vacuum Science & Technology a-Vacuum Surfaces and Films* **7**, 903-907

Levine, I. N.: 2002, *Physical chemistry*, Published by McGraw-Hill, ISBN 0072318082

Li, G. and Yang, Y.: 2008, *Nanotechnology* **19**

Lide, D. R.: 2009, *Handbook of chemistry and physics*, Published by Taylor and Francis, ISBN 9781420090840

Lieberman, M. A. and Lichtenberg, A. J.: 2005, *Principles of plasma discharges and materials processing*, Published by Wiley-Interscience, ISBN 0471720011

Margot, J. and Moisan, M.: 1993, *Journal of Plasma Physics* **49**, 357-374

Matsuo, S. and Adachi, Y.: 1982, *Japanese Journal of Applied Physics Part 2-Letters* **21**, L4-L6

Matsuoka, M. and Ono, K.: 1988a, *Journal of Applied Physics* **64**, 5179-5182

Matsuoka, M. and Ono, K. I.: 1988b, *Journal of Vacuum Science & Technology a-Vacuum Surfaces and Films* **6**, 25-29

Miller, D. B.: 1966, *Ieee Transactions on Microwave Theory and Techniques* **MT14**, 162

Moisan, M., Barbeau, C., Claude, R., Ferreira, C. M., et al.: 1991, *Journal of Vacuum Science & Technology B* **9**, 8-25

Ono, T., Oda, M., Takahashi, C. and Matsuo, S.: 1986, *Journal of Vacuum Science & Technology B* **4**, 696-700

Payne, M. C., Teter, M. P., Allan, D. C., Arias, T. A., et al.: 1992, *Reviews of Modern Physics* **64**, 1045-1097

Perry, A. J., Vender, D. and Boswell, R. W.: 1991, *Journal of Vacuum Science & Technology B* **9**, 310-317

Popov, O. A.: 1995, *High density plasma sources : design, physics and performance*, Published by Noyes Publications, ISBN 0815513771

Rabalais, J. W.: 1990, *Science* **250**, 521-527

Ranjan, A., Donnelly, V. M. and Economou, D. J.: 2006, *Journal of Vacuum Science & Technology A* **24**, 1839-1846

Ricard, A., Barbeau, C., Besner, A., Hubert, J., et al.: 1988, *Canadian Journal of Physics* **66**, 740-748

Rodriguez, L. M., Gayone, J. E., Sanchez, E. A., Grizzi, O., et al.: 2007, *Journal of the American Chemical Society* **129**, 7807-7813

Rossnagel, S. M., Whitehair, S. J., Guarnieri, C. R. and Cuomo, J. J.: 1990, *Journal of Vacuum Science & Technology a-Vacuum Surfaces and Films* **8**, 3113-3117

Sakimoto, K.: 2000, *Journal of Chemical Physics* **112**, 5044-5053

Samukawa, S., Mori, S. and Sasaki, M.: 1991, *Journal of Vacuum Science & Technology a-Vacuum Surfaces and Films* **9**, 85-90

Sandreczki, T. C. and Brown, I. M.: 1990, *Macromolecules* **23**, 1979-1983

Sezen, M., Plank, H., Nellen, P. M., Meier, S., et al.: 2009, *Physical Chemistry Chemical Physics* **11**, 5130-5133

Shuttle, C. G., O'Regan, B., Ballantyne, A. M., Nelson, J., et al.: 2008, *Applied Physics Letters* **92**

Stevens, J. E., Huang, Y. C., Jarecki, R. L. and Cecchi, J. L.: 1992, *Journal of Vacuum Science & Technology a-Vacuum Surfaces and Films* **10**, 1270-1275

Tokiguchi, K., Sakudo, N. and Koike, H.: 1986, *Review of Scientific Instruments* **57**, 1526-1530

Torii, Y., Shimada, M. and Watanabe, I.: 1987, *Nuclear Instruments & Methods in Physics Research Section B-Beam Interactions with Materials and Atoms* **21**, 178-181

Torii, Y., Shimada, M. and Watanabe, I.: 1992, *Review of Scientific Instruments* **63**, 2559-2561

Tuma, D. T.: 1970, *Review of Scientific Instruments* **41**, 1519

Verlet, L.: 1967, *Physical Review Online Archive (Prola)* **159**, 98

Weng, Y. L. and Kushner, M. J.: 1992, *Journal of Applied Physics* **72**, 33-42

Yamashita, M.: 1989, *Journal of Vacuum Science & Technology a-Vacuum Surfaces and Films* **7**, 151-158

Zheng, Z., Kwok, W. M. and Lau, W. M.: 2006, *Chemical Communications* 3122-3124

Chapter 3

3 Evaluation of HHIC method

3.1 Introduction

The HHIC method is theoretically very interesting and promises broad applications in numerous fields of applied physics and chemistry. One such area is organic electronics (Klauk, 2006), where the demands on material purity are very high (Takimiya et al., 2004; Boudinet et al., 2009; Braga et al., 2009; Horowitz, 2010). Making of a functional device from solution proceeds in many steps and typically requires the use of more than one solvent (Horowitz, 2004; Horowitz et al., 2004; Yaghmazadeh et al., 2008). P-n junction or hetero-junctions in general are a great example. If the two materials of opposite conductivity or, better say, materials processed in sequence require the use of the same or different, but orthogonal, solvent, than it is necessary to protect the first layer from dissolution in subsequent step (Pang et al., 2009; Ie et al., 2010; Suganuma et al., 2011; Zhao et al., 2011). The only viable method to achieve this goal is to cross-link the material rendering it insoluble. Typically, cross-linking proceeds through intermediate agents, which when activated (e.g., by temperature (Cheng et al., 2008; Liu et al., 2008; Cho et al., 2011; Yip et al., 2011), or by radiation (Qiu et al., 2005; Rentenberger et al., 2006; Himmelhuber et al., 2008; Zhang et al., 2011)) change their chemical composition and recombine with another such agent. This results in “foreign” bodies which present a threat to the integrity of the conducting material. This is where the HHIC method as a physical process promises to deliver a significant increase in performance of organic electronic devices (e.g., field effect transistors, solar cells) prepared from solution. However, even for devices made by dry processing (Ma et al., 2010; Zou et al., 2010), the HHIC offers interesting uses. If a penetration of evaporated material during deposition into the organic matrix is of concern, the HHIC may protect the top surface by increasing its density, i.e., increasing its inelastic mean free path.

Organic electronics is not the only field where the strengths of HHIC can be utilized. Surface-initiated polymerization (Horak et al., 2011; Park et al., 2011) or grafting of

chemical moieties (Zhang et al., 2008; Mu et al., 2009; Lao et al., 2011) onto inert surfaces is another broad area, which greatly benefits from the physical nature of HHIC. Imagine a material comprising sensitive functional groups being exposed to harsh (even remote) plasma environment (Hegemann et al., 2003; Hwang et al., 2004; Forch et al., 2005; Tajima et al., 2007), which indiscriminately reacts with all present bonds. An overwhelmingly high retention of functional groups is the hallmark of the HHIC method, as will be shown in the example of poly(acrylic acid) in Section 3.4.

The fabrication of organic transistors (see for example Jia et al., 2007; Kim et al., 2008; Pang et al., 2009) as well as solar cells (to a certain degree) involves a deposition of spatially distributed conducting, semiconducting, and insulating pathways or layers. To achieve such uneven coverage one has to either deposit the material in a specific area or to remove already deposited material from regions where it is not supposed to be. The HHIC method is capable of preferentially cross-linking selected areas by using a shadow mask. The uncured material is then removed by exposing the sample to a solvent (in analogy to a standard lithography process).

This chapter is divided into three parts to best represent all important aspects of the HHIC method: ability to cross-link short hydrocarbon molecules (Section 3.2), ability to cross-link a semiconducting organic polymer without degrading its properties (Section 3.3), selectivity towards chemical functional groups, and ability to pattern cross-linked areas (both Section 3.4).

3.2 Dotriacontane

With the availability of this practical reactor to run HHIC experiments, we set to evaluate the effectiveness of the HHIC method. In this analysis, we deposited a thin layer of a simple and short alkane molecule dotriacontane (n-$C_{32}H_{66}$) onto freshly cleaved mica and used the surface sensitive technique of X-ray photoelectron spectroscopy to monitor the layer thickness. In this experiment, when the exposure of the layer to hyperthermal H_2 was not sufficient, the layer was removed by a simple heptane rinse. With an increased exposure to hyperthermal H_2, the degree of cross-linking was raised which reduced the layer solubility and led to a greater retention of the material (as measured by the layer

thickness). Using the thickness as a metric allowed us to study the dependence of the degree of cross-linking on the H^+ extraction energy, pressure, and fluence. It also provided a simple methodology to compare the effects of hydrogen and helium bombardment on C–H and C–C bond cleavage as presented in Section 2.2.4.2.

Dotriacontane has not been extensively studied but its simple nature, vacuum stability and ability to form semi-crystalline layers (Beiny et al., 1990; Cisternas et al., 2009) make it an interesting model material for the evaluation of HHIC. Atomic force microscopy (Trogisch et al., 2005) and ellipsometry (Volkmann et al., 2002) show that dotriacontane forms smooth uniform layers, which is very important for obtaining representative and reproducible XPS results.

3.2.1 Experimental setup

Samples for XPS analysis were prepared using the following procedure. Based on the requirements for atomically flat surface on a large scale and based on preliminary wettability trials, mica (phyllosilicate mineral) in its most common muscovite form was chosen as a substrate over polished silicon dioxide. Mica offers highly-perfect basal cleavage producing a fresh surface with long environmental stability. Mica sheets of dimensions $2.54 \times 2.54\ cm^2$ were purchased from Sigma Aldrich and diced down to yield four smaller pieces of the same area. Prior to deposition of a dotriacontane solution, mica substrate was cleaved using a scotch tape to prepare a fresh surface.

A solution of 0.2 wt.% of dotriacontane ($C_{32}H_{66}$, purchased from Alfa Aesar, used as received) in heptane (HPLC grade purchased from Fisher Scientific, used as received) was prepared and filtered through a 0.2 µm PTFE syringe filter to remove large inorganic contaminants. A thin layer of dotriacontane was deposited on mica by spin-casting of 70 µL of the solution at 1500 RPM and acceleration 1490 RPM/s for 60 s[*]. The sample was then immediately transferred into the XPS machine for analysis of as-deposited dotriacontane. In fact, every experiment was conducted for four samples at a time. All

[*] In regards to all spin-casting procedures referenced throughout this text, it should be noted that the spin-casting was static. It means that during an acceleration period and depending upon the solvent vapor pressure, it is possible that the solvent fully evaporates before reaching the final speed.

four samples were inserted inside the reactor and the ones not being exposed covered by a sheet of stainless steel

X-ray photoelectron spectroscopy (XPS) spectra were recorded on a Kratos AXIS Ultra instrument using a monochromatic Al Kα photon source at 10 mA and 14 kV. The analyzer used both electric and magnetic fields to focus secondary electrons. A size of the analysis area from which the secondary electrons were collected was $\sim 300 \times 700$ μm^2. Sample data were collected at a take-off angle of 0° (relative to the sample normal) and at three different spots to show a variation of thickness across the area of a sample. Spectra recording commenced after reaching a background gas pressure $< 1 \times 10^{-8}$ Torr in the analytical chamber to ensure a complete removal of solvent residues. Survey scans were conducted in order to confirm the exact composition of mica and dotriacontane and to gather low-resolution data for thickness calculation. Six survey scans per sample were collected for binding energies ranging from 0 to 1100 eV, at 0.5 eV steps, the pass energy 160 eV, and scan times of 120 s. Ten high-resolution C 1s scans were collected for binding energies spanning 278–295 eV, at 0.1 eV steps, the pass energy 20 eV, and scan times of 60 s. CasaXPS version 2.3.15 was used for the analysis of all the XPS spectra. All spectra were referenced to the aliphatic C–H bond at 285 eV and the fitting of the high-resolution C 1s peak was accomplished using one envelope (Gaussian to Lorentzian ratio of 40).

Hyperthermal hydrogen bombardment was carried out for a combination of the following parameters after reaching the background gas pressure of 2×10^{-6} Torr. The output microwave power was 200 W for all experiments. Accelerating voltages were −50, −100, −200, −400 V, first retarding voltages copied the values of V_{acc} with opposite polarity and the second retarding voltage was −50 V. Operating pressures (for both hydrogen and helium) ranged from 0.5 to 1.5 mTorr. The extraction current was set to 10 mA for a given combination of V_{acc} and p by varying the strength of the magnetic field, which ranged from 82 to 93 mT. Samples were cross-linked for 10 or 20 s after which time they were left under vacuum at the same pressure for 2 mins to allow for recombination of remaining carbon radicals in a predominantly hydrogen environment.

Every sample underwent three XPS data collection cycles, one HHIC bombardment, and one washing step. XPS spectra were recorded: 1) for fresh dotriacontane layer immediately after deposition; 2) after HHIC treatment; and 3) after washing. Washing of uncross-linked material was achieved by spin-casting of 70 µL of heptane at 1500 RPM and acceleration 1490 RPM/s for 60 s. The washing step was repeated two times.

3.2.2 Results and discussion

Evaluation of the HHIC method by measuring a thickness of the dotriacontane layer is in a way representative of the degree of cross-linking. If our polymerization agents (hyperthermal hydrogen molecules) do not generate a high enough density of cross-links (increasing the average molecular weight) parts of the material layer will wash away during the wash test.

The thickness of the dotriacontane layer is calculated from XPS intensities using a modified formula originating from a very popular method developed by Hill et al.

$$t = -\lambda \cos\theta \ln\left(1 + \frac{I_0}{I_s}\frac{s_s}{s_0}\right),$$

where t is the layer thickness, λ is the attenuation length of the secondary electrons (photoelectrons) in the film, θ is the take-off angle, I_0 and I_s are the measured peak intensities from the overlayer and substrate, respectively, and s_0 and s_s are their sensitivity factors. The formula was modified for the purpose of measuring a carbon rich layer over carbon deficient mica as

$$t = -\lambda \ln\left[1 + \frac{I_C}{\left(\frac{I_O}{s_O} + \frac{I_K}{s_K} + \frac{I_{Si}}{s_{Si}} + \frac{I_{Al}}{s_{Al}}\right)}\right],$$

where $\cos 0° = 1$, $s_O = 2.93$ is the sensitivity factor of oxygen, $s_K = 3.97$ is the sensitivity factor of potassium, $s_{Si} = 0.817$ is the sensitivity factor of silicon, and $s_{Al} = 0.537$ is the sensitivity factor of aluminum.

The degree of cross-linking as measured from thickness changes induced by HHIC ($p = 0.5$ mTorr, $I_{acc} = 10$ mA, $t_{bombardment} = 10$ s, with accelerating voltage as parameter) is summarized in Figure 34. The individual values represent ratios of thicknesses (of the dotriacontane layer) after specific steps and could be expressed as

$$\text{HHIC} \leftrightarrow \frac{thickness\ after\ bombardment}{thickness\ of\ pristine\ material}, \text{and}$$

$$\text{washed} \leftrightarrow \frac{thickness\ after\ washing}{thickness\ of\ pristine\ material}.$$

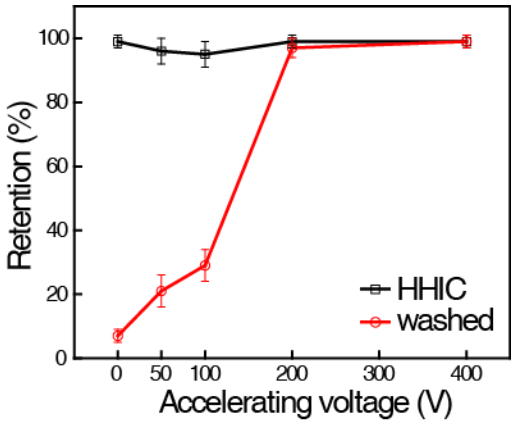

Figure 34. Effectiveness of C–H cleavage of n-$C_{32}H_{66}$ as a function of V_{acc} (initial KE of hydrogen initiators), showing a drastic reduction of cross-linking efficiency for projectiles having insufficient energy to cleave C–H bonds. Shown is the retention of sample thickness after HHIC and after washing.

As expected, the HHIC effectiveness drops when the H^+ extraction energy (eV_{acc}) is too low, as not enough H_2 projectiles having sufficient energy to break C–H bonds are produced. The points corresponding to $V_{acc} = 0$ V were collected for a control sample which was not HHIC treated, correctly demonstrating virtually complete dissolution of the hydrocarbon film.

The results shown in Figure 34 led to a series of follow-up experiments aimed at providing additional information about the effects of pressure and fluence on the efficiency of HHIC. The first condition, where HHIC effectively cross-linked the dotriacontane film ($V_{acc} = 200$ V) was taken as a reference and fixed. Pressure, on the

other hand, was varied from 0.5–1.5 mTorr. The extraction current was set to 10 and 20 mA. The results are summarized in Figure 35.

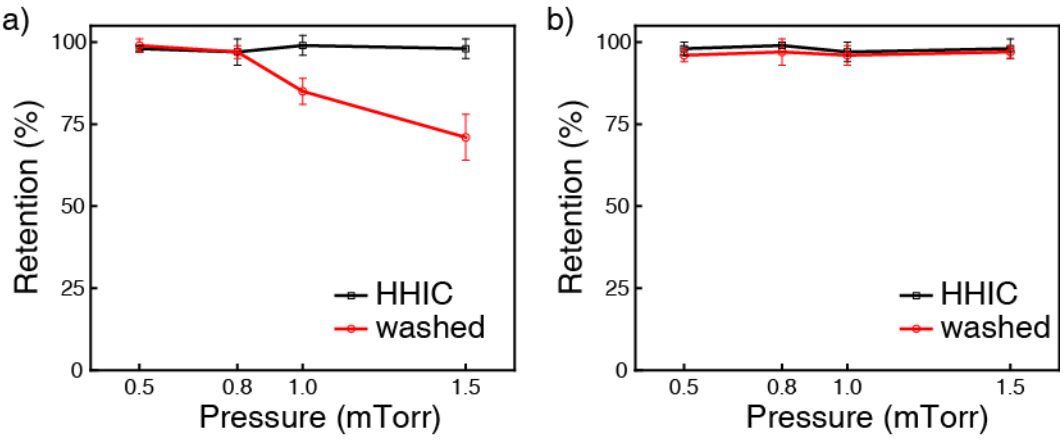

Figure 35. Further studies of efficiency of the HHIC method. Thickness ratios for constant $V_{acc} = 200$ eV, and a) $I_{acc} = 10$ mA and b) $I_{acc} = 20$ mA.

It is not surprising to observe that for pressures ≤1.0 mTorr the average energy of hyperthermal projectiles is insufficient to fully cross-link the alkane layer. Quite unexpected, however, was the effect of an increased bombardment time. This relatively small difference, although in absolute values twice as large, in the cross-linking time led to rendering the film completely insoluble.

Hydrogen molecules were chosen as a cross-linking agent because collisions between H_2 and H of a C–H bond and between H_2 and C of a C–H bond result in the highest and lowest energy transfers, respectively. Table 1 documents that using helium instead of hydrogen (under the same HHIC conditions) leads to a significant fragmentation of the hydrocarbon chain due to the cleavage of C–C bonds and subsequent desorption of the resulting parts. However, helium induced cross-linking occurs at the same time.

Table 1. Comparison of thickness retention ratios for hydrogen and helium driven HHIC.

	H_2 (%)	He (%)
HHIC	99	85
washed	97	79

It should be noted that the control samples, which were carried along throughout the experiment, experienced an average increase in thickness of $5 \pm 2\%$ between the first and second XPS analyses. This effect is a by-product of running the experiments *ex situ* where samples are exposed to ambient conditions for prolonged periods of time (up to 30 min). If the experiments were carried out *in situ*, one would expect to observe a small decrease in thickness after bombardment, which would be due to the decrease in the intra-chain distances caused by cross-linking (as was observed in other experiments on butyl rubber and octadecylphosphonic acid). The fact that we observe virtually no decrease in thickness after HHIC may be a result of the combination of hydrocarbon contamination and material shrinkage. If the HHIC reactor was connected to an XPS machine (and the standard deviations were smaller), one could quantify the magnitude of the film thickness reduction.

3.2.3 Conclusion

Dotriacontane offered a simple experimental model for proving the concept of HHIC. It is evident that a small hydrocarbon molecule such as $C_{32}H_{66}$ increases its molecular weight by surface-initiated polymerization when exposed to hyperthermal hydrogen. A highly surface-sensitive X-ray photoelectron spectroscopy technique was adopted to provide chemical composition data for thickness measurements, which served as a metric of the degree of cross-linking. The results showed that finding the right bombardment conditions is important to fully complete the cross-linking of the material rendering it insoluble. We have also shown that it is possible to use helium instead of hydrogen, as was suggested by simple theoretical calculations, to drive the HHIC reaction, yet it is impractical because it loses selectivity in preferentially breaking C–H bonds.

3.3 Poly(3-hexylthiophene)

The next step in evaluating the HHIC method is to shift the focus to more application oriented materials. We have chosen poly(3-hexylthiophene) (P3HT) to represent a broad family of semiconducting polymers because thiophenes, in general, and their derivatives show one of the highest charge mobilities (~0.1 $cm^2\ V^{-1}$ as reported by Sirringhaus et al.) for both solution and evaporation based organic devices (Park et al., 2003; Yang et al.,

2003; Seol et al., 2007; Zimmermann et al., 2009; Scarpa et al., 2010). P3HT has long been used in field effect transistors (Park et al., 2003; Yang et al., 2003; Jia et al., 2007; Seol et al., 2007; Pang et al., 2009) and solar cells—in blends (Alet et al., 2006; Kim et al., 2007; Wang et al., 2010) and heterojunctions (Kalita et al., 2010; Shen et al., 2011).

A complex set of experiments was carried out to qualify and quantify the effects of HHIC on the most common material used in semiconductor organic electronics. These experiments involved topographical changes, changes of elemental and chemical composition, and changes of electrical properties.

3.3.1 Experimental setup

P3HT, poly(3-hexylthiophene-2,5-diyl) with product number 4002-EE (high electronic grade) and typical regioregularity between 90–94%, was purchased from Rieke Metals, Inc. Solutions of 0.15 wt.% and 0.5 wt.% of P3HT in chloroform (HPLC grade purchased from Fisher Scientific) were prepared in the dark and filtered through a 0.2 μm PTFE filter. All chemicals and materials were used as purchased.

Samples for atomic force microscopy (AFM) studies were prepared as follows: a layer of P3HT was deposited on clean silicon chip (1×1 cm^2) by spin-casting of 50 μL of the solution at 2500 RPM and acceleration 1490 RPM/s for 60 s under ambient conditions. Hyperthermal hydrogen bombardment was carried out for a combination of the following parameters after reaching the background gas pressure of 2×10^{-6} Torr. The output microwave power was 200 W for all experiments, $V_{acc} = -100$ V, $V_{r1} = 100$ V, $V_{r2} = -50$ V, $p = 0.8$ mTorr, and $I_{acc} = 100$ mA. Samples were cross-linked for 5, 15, 25, and 30 s after which time they were left under vacuum at the same pressure for 2 min. Washing was completed by spin-casting of 50 μL of chloroform at 2500 RPM and acceleration 1490 RPM/s for 60 s. This step was repeated two times.

AFM studies were performed using a XE-100 station made by Park Systems. All scans were carried out in a non-contact mode using uncoated VISTAprobes® tips T300-25 with the spring constant of $k = 40$ Nm^{-1}, resonant frequency 300 kHz, and an average tip radius <10 nm. Once a significant degradation in image quality was observed, a fresh tip

was used. Scans were collected over two areas (5 and 40 μm^2) at a constant image resolution of 256×256 pixel^2. Thickness measurements were conducted across an interface that was previously scratched for pristine samples, samples after HHIC, and after washing. Three measurements were taken from one image (spot) for a total three spots evenly distributed across the scratch and averaged.

X-ray photoelectron spectroscopy (XPS) spectra were recorded on a Kratos AXIS Ultra instrument using a monochromatic Al Kα photon source at 1486.6 eV and with source filament current set to 10 mA at 14 kV. The analyzer was set to hybrid mode using both electric and magnetic fields to focus secondary electrons. A size of the analysis area from which the secondary electrons were collected was $\sim 300 \times 700$ μm^2. Sample data were collected at a take-off angle of 0° (relative to the sample normal) and three different spots to show a variation of thickness across the area of a sample. Survey scans were collected from 0 to 1100 eV, with energy step of 0.7 eV, and the analyzer pass energy at 160 eV. One survey scan was collected for 90 s. High-resolution C 1s spectra (5 scans total) were collected for binding energies ranging from 278 to 295 eV and high-resolution S 2p spectra (10 scans total) were recorded for binding energies spanning 160–170 eV, with energy step of 0.1 eV, the analyzer pass energy at 20 eV, and scan time of 120 s. CasaXPS version 2.3.15 was used for the analysis of all the XPS spectra. All spectra were referenced to the C–H bond at 285 eV and the fitting of high-resolution C 1s peak was accomplished with a Gaussian/Lorentzian profile of ratio 40.

Samples for UV-Vis studies were prepared as follows: Two solutions of different concentrations of P3HT in chloroform were prepared (0.15 wt.% and 0.5 wt.%). A P3HT film was deposited on clean round microscope cover slips by spin-casting of 100 μL of solution at 2500 RPM and acceleration 1490 RPM/s for 60 s under ambient conditions. Hyperthermal hydrogen bombardment was carried out for a combination of the following parameters after reaching the background gas pressure of 2×10^{-6} Torr. The output microwave power was set to 200 W, $V_{acc} = -100$ V, $V_{r1} = 100$ V, $V_{r2} = -50$ V, $p = 0.8$ mTorr, $I_{acc} = 10$ and 100 mA. Samples were cross-linked for 5, 10, 15, and 20 s followed by a 2 min stay under vacuum. Washing was completed by spin-casting of 100

µL of chloroform at 2500 RPM and acceleration 1490 RPM/s for 60 s. This step was repeated two times.

Ultraviolet-visible spectroscopy experiments were carried out using a Perkin Elmer Lambda 850 spectrometer. Spectra were collected at wavelengths ranging from 750 to 350 nm at a wavelength step of 1 nm for three samples (for statistical purposes). Reference spectra of air and glass substrates were collected and subtracted during data analysis.

The sample design used for four probe measurement is depicted in Figure 36. The area of electrodes was first etched using reactive ion etching to the depth of 100 µm. Gold electrodes were then e-beam evaporated onto a silicon wafer with a 1 µm thick thermally grown oxide using chromium as an adhesion promoter. Burying the electrodes below the oxide surface shields the chromium adhesion layer from oxidation and was shown to reduce undesired Au spike residues resulting from a lift-off process.

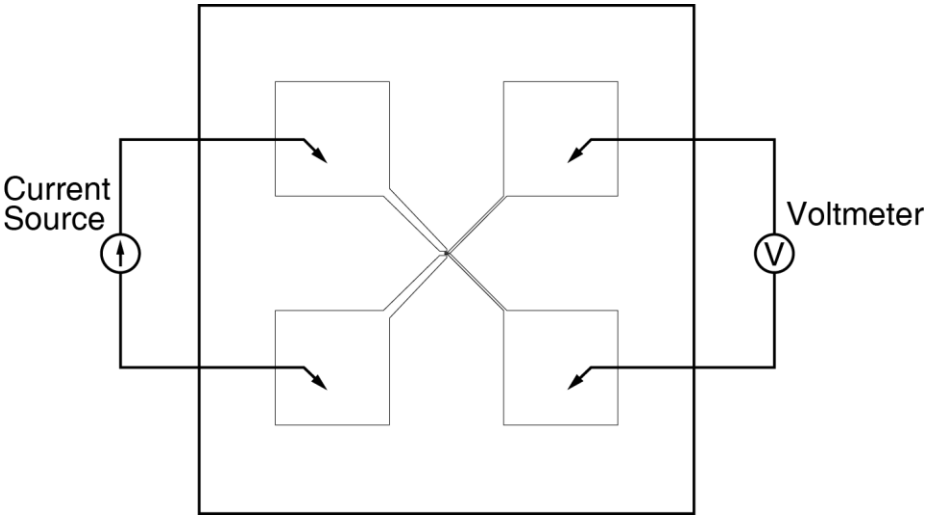

Figure 36. Layout of a four-probe measurement device with a diagram of current-voltage sensing mechanism.

Samples for 4-probe measurements were prepared from 0.15 wt.% solution of P3HT in chloroform. A P3HT film was deposited on clean silicon chips by spin-casting of 50 µL of solution at 2500 RPM and acceleration 1490 RPM/s for 60 s under ambient conditions. Hyperthermal hydrogen bombardment was carried out for a combination of the following

parameters after reaching the background gas pressure of 2×10^{-6} Torr. The output microwave power was set to 200 W, $V_{acc} = -100$ V, $V_{r1} = 100$ V, $V_{r2} = -50$ V, $p = 0.8$ mTorr, $I_{acc} = 100$ mA. Samples were cross-linked for 30 s followed by a 2 min settling period under vacuum. Washing was completed by spin-casting of 50 µL of chloroform at 2500 RPM and acceleration 1490 RPM/s for 60 s. This step was repeated two times.

Resistivity measurements were carried out using a Keithley 2400 source meter acting as a current source and a voltmeter. All samples were mounted using a Signatone HS100 probe station. The procedure for taking current-voltage characteristics is the same as presented in Section 2.3.2.1.

ToF-SIMS data were collected on an ION-TOF TOF-SIMS-IV instrument equipped with a Bi liquid metal ion source using a 25 keV $Bi3^+$ cluster primary ion beam pulsed at 10 kHz with a pulse width of 12 ns and a target current of 1 pA.

3.3.2 Results and discussion

It is obvious that, if HHIC were to cause significant topographical alteration of the target material, it would not be a very useful method. We have studied topographical changes induced by HHIC using atomic force microscopy. Results show (Figure 37) that (a) a pristine P3HT sample carried through (b) a HHIC bombardment and a subsequent (c) washing step does not suffer any major spatial distortion under the right HHIC conditions (average roughness across the scanned area is provided in Table 2).

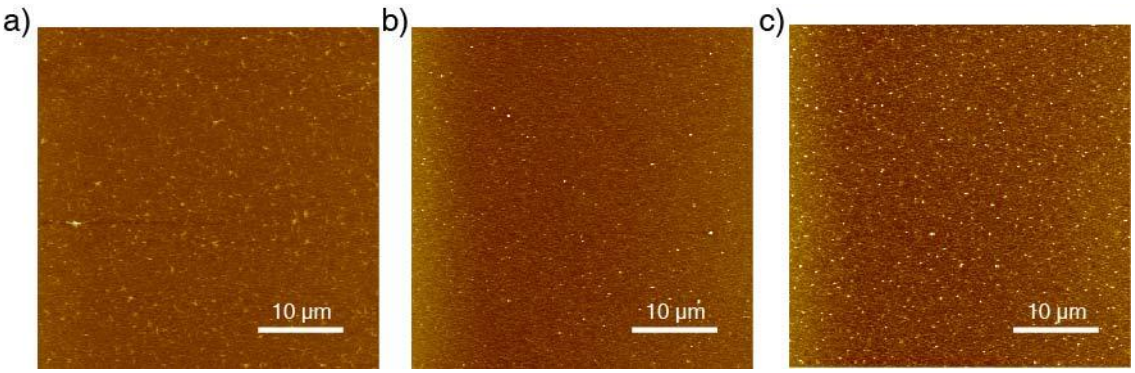

Figure 37. AFM topography images of P3HT thin film on silicon substrate for a) pristine sample, b) HHIC treated sample, and c) HHIC treated and washed.

As already suggested, thickness changes may occur during HHIC treatment. If the cross-linking is incomplete it may also lead to a significant drop in thickness after washing. For these reasons, we have decided to quantify thickness variation throughout the process of deposition, HHIC bombardment, and washing. The results are summarized in Table 2.

Table 2. Variation in P3HT film thickness in nm.

Spot	Pristine	HHIC	washed
1st	12.56	12.46	12.07
	12.38	12.50	12.05
	12.58	12.39	12.42
2nd	12.44	12.41	12.06
	12.34	12.24	12.03
	12.43	12.26	13.05
3rd	12.43	12.18	12.56
	12.26	12.25	12.37
	12.43	11.99	12.22
Thickness (nm)	12.43±0.11	12.30±0.16	12.32±0.34
RMS roughness (nm)	0.764	0.770	0.692

Having a pristine P3HT film with a starting thickness of 12.43±0.11 nm and the same film after HHIC treatment with a thickness of 12.30±0.16 nm, it is unclear whether HHIC bombardment causes a P3HT layer to shrink, although it is suggested. It is, however, very encouraging that neither thickness nor topography of the washed sample changed as a result of HHIC. We have therefore produced a cross-linked polymer film without any topographical or evident morphological changes.

As we well know, the HHIC process consists of setting many different parameters such as pressure, accelerating voltage, extraction current, or bombardment time. If we chose the parameters in a way to decrease the fluence of hyperthermal projectiles the results might change. Let us take a look at what happens when the bombardment time decreases from 30 s (Figure 37) to 25, 15, and 5 s (other parameters kept the same). We see, yet again, that finding the right HHIC conditions for a given material is very important. If the bombardment time (fluence) decreases by 5 s (Figure 38c) we start to see the formation of localized areas with low degree of cross-linking. If we decrease the exposure time by an additional 10 s (Figure 38b), it becomes evident that solvent starts to penetrate the P3HT matrix, swells it, and dissolves it. AFM shows that the affected area is elevated above the film surface, which is probably a result of P3HT cramping during a drying period. If we further decrease the bombardment time to 5 s (Figure 38a), the degree of cross-linking becomes so low that the P3HT layer readily dissolves during washing and leaves only isolated islands of cured material.

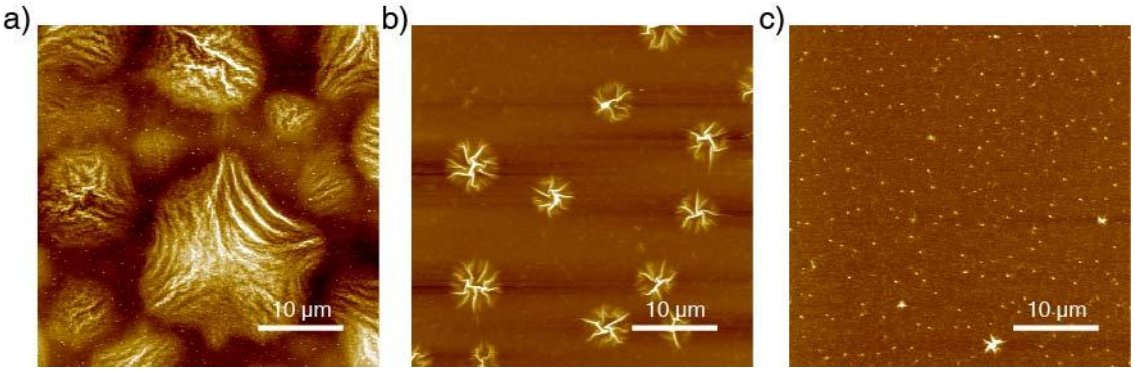

Figure 38. AFM topography images of P3HT thin film after HHIC and washing. HHIC bombardment times were: a) 5 s, b) 15 s, and c) 25 s.

XPS was used to quantify the degree to which HHIC affects the chemical composition of P3HT. The HHIC bombardment conditions were exactly the same as those for AFM studies. High-resolution XPS spectra (shown in Figure 39[*]) of C 1s (top row) and S 2p (bottom row) regions represent a) pristine, b) HHIC treated, and c) HHIC treated and

[*] Note: red lines represent the actual spectrum, thin black lines represent the GL fitting curve, and dashed black lines represent a sum of individual fits.

washed P3HT film. The C 1s spectra are described by a two component fit, consistent with the assignment of two forms of carbon in the polymer, those of the alkyl side chains (~285 eV) and those arising from the aromatic ring (~285.3 eV) as well as by a broad peak representing various carbon oxide states. The two carbon types were optimized to an energy separation of 0.34 eV (Gelius et al., 1971) and an atomic ratio of 4:1, as dictated by the chemical structure. The S 2p region was fit with a single doublet S 2p3/2 (164.2 eV) and S 2p1/2, maintaining a ratio of 2:1 and a peak energy separation of 1.19 eV, consistent with previously reported results of 1.25 eV for thiophene by Gelius et al. The S 2p region of HHIC treated samples was additionally fit with a doublet S 2p3/2 (shifted down to 163.4 eV) and S 2p1/2 keeping the same energy separation. This second S 2p doublet represents S–H bonds.

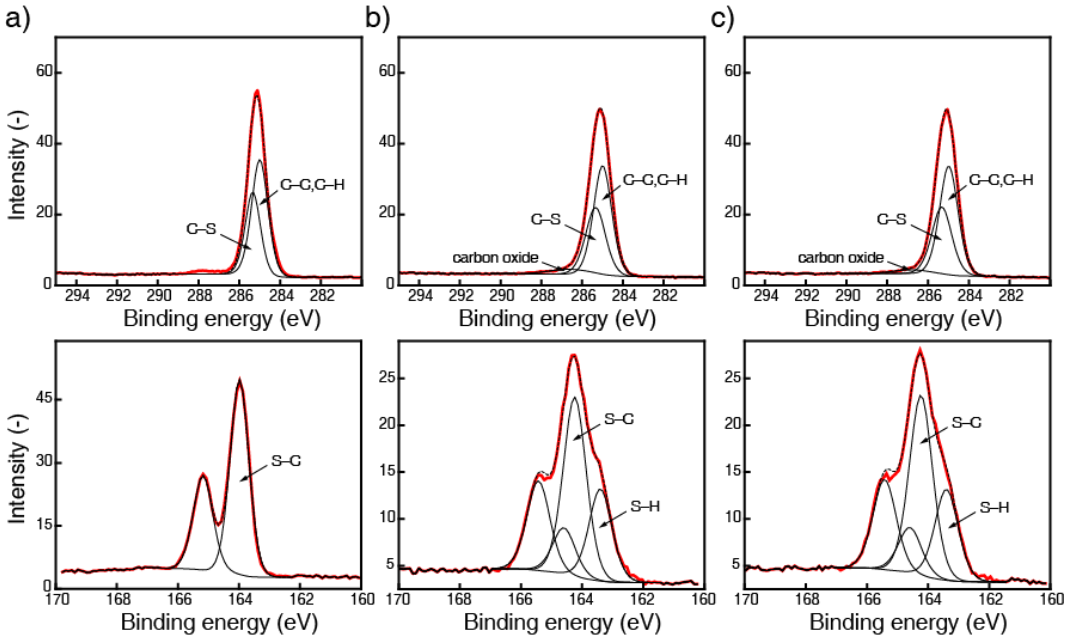

Figure 39. High-resolution XPS spectra of C 1s (top row) and S 2p (bottom row) regions for P3HT film: a) pristine, b) HHIC treated, and c) HHIC treated and washed.

The results clearly indicate that HHIC method does not preserve the presented conjugated system very well. The sulfur S–C single bond photo-dissociates forming a S–H bond with an atomic concentration ratio 2:1. This negative effect is primarily due to plasma induced radiation degradation. In order to confirm this hypothesis, a modified configuration of

P3HT sample placement was used. In a distance of 1 cm directly above the sample a piece of glass (borosilicate and quartz) was mounted during the HHIC bombardment. The XPS results showed virtually no change (±1%) in either C 1s or S 2p high-resolution peaks indicating that filtering deep vacuum UV (bellow 180 nm cut-off wavelength for the used quartz glass) radiation is responsible for preserving the conjugated system. However, under the same HHIC conditions the P3HT layer is not fully cross-linked, as the fluence of hyperthermal particles is not high enough, and partially dissolves upon washing.

It is also necessary to report on a very unfortunate behaviour of the present HHIC reactor. Since its inception, it has undergone two rather complicated relocations. Ever since the moves were completed, the system started to oxidize samples, which is most probably due to a vacuum leak. Despite a significant effort to find and correct the problem, we have not yet been successful. Let us take a look (Figure 40) at XPS survey spectra characterizing the effects of HHIC on the same P3HT film as shown above.

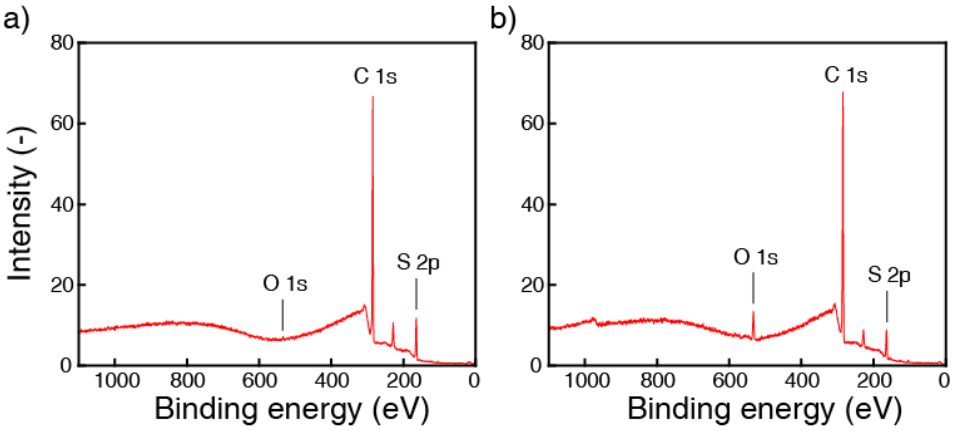

Figure 40. XPS survey spectra of a) pristine and b) HHIC treated P3HT film showing elemental composition of oxygen, carbon, and sulfur.

Figure 40a shows a pristine P3HT layer indicating virtually no oxidation (0.72 at.%), carbon concentration of 88.87 at.%, and sulfur concentration of 10.41 at.%. Figure 40b corresponds to a HHIC treated P3HT film with a clearly visible increase in oxygen concentration (4.47 at.%), carbon concentration of 88.17 at.%, and sulfur concentration of 7.36 at.%. Based on these values, it would be obvious to assign the increased oxygen

content to the formation of sulfur oxides. However, consulting the high-resolution S 2p spectra summarized in Figure 39, we have to conclude that no oxidation of sulfur occurred as there are no visible oxide peaks shifted toward higher binding energies (as would be consistent with the observations of Hintz et al., 2010). The apparent increase in oxygen atomic concentration at the expense of sulfur is most likely a result of an overall decrease in sulfur concentration due to chain fragmentation and desorption, which leads to a relative increase in carbon content.

The unfortunate photo-induced degradation of P3HT is also supported by ultraviolet-visible spectroscopy (UV-Vis) as measured by the loss of optical absorbance. It is evident in Figure 41 that the absorption spectrum after HHIC is blue-shifted. This effect could be attributed to either a decrease in regio-regularity or a photo-induced oxidation, however, based on the XPS results the latter is not the case. Figure 42 shows the UV-Vis results of P3HT layers thicknesses retention for 15 nm (a, b) and 35 nm thin films (c, d) exposed at $I_{acc} = 10$ mA (a, c) and 100 mA (b, d).

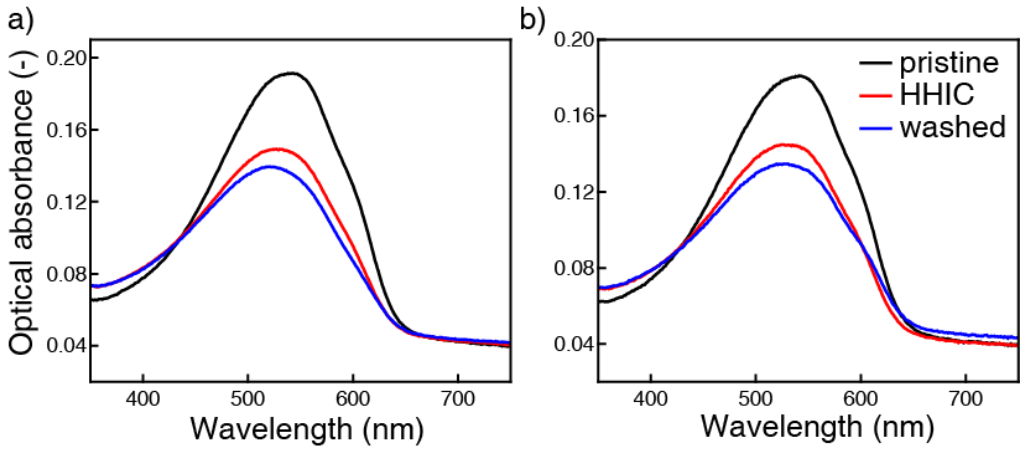

Figure 41. UV-Vis optical absorbance for 10 nm thick P3HT layer exposed to HHIC at a) 10 mA, and b) 100 mA showing a blue shift.

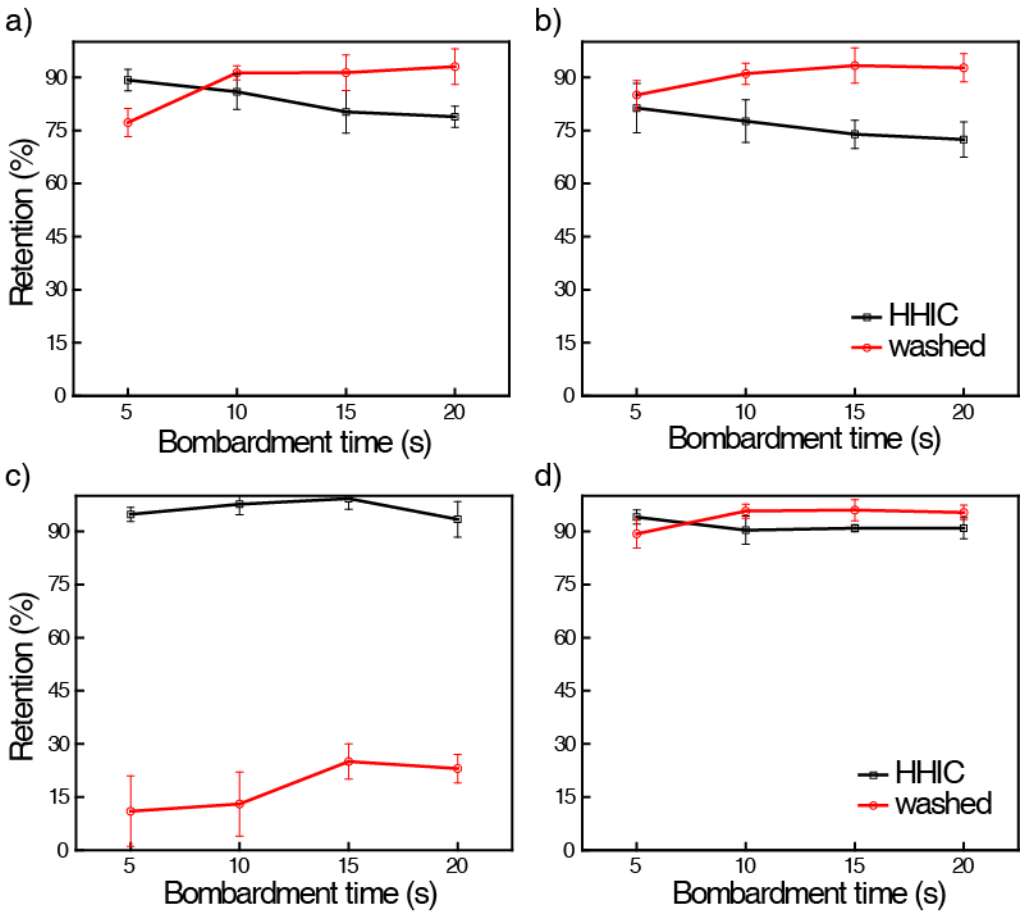

Figure 42. Retention of lost optical absorbance as measured by UV-Visible spectroscopy for 15 nm P3HT film HHIC treated at a) 10 mA and b) 100 mA extraction current, and 35 nm P3HT film HHIC treated at c) 10 mA and d) 100 mA extraction current.

Generally speaking, samples exposed for short periods of time suffer less from optical absorbance degradation. It is also quite interesting that samples bombarded at higher hyperthermal particle concentration (higher plasma density=more intense plasma radiation) lose roughly (taking errors into account) the same amount of optical absorbance. It is, therefore, imperative to solve the issue of sample radiation exposure to allow this technique be conveniently applied to light sensitive materials.

Although we know that HHIC causes photo-degradation of P3HT a set of conductivity (resistivity) measurements was carried out to quantify its impact on electrical properties. Strictly speaking, the results yield resistance of the device under test and we are primarily

interested in differences between pristine P3HT, HHIC treated, and HHIC treated and washed samples, instead of absolute values of resistance. It can be seen that resistance increases after bombardment, which is by no means surprising considering the effect of plasma radiation on the thiophene π–π* conjugated system. What is, however, unexpected is that the increase amounts to only about 2.5%. Based on the XPS data, where almost half the sulfur double bonds were converted into S–H, one would anticipate a more significant degradation in electrical properties.

Table 3. Resistance ratios for HHIC treated P3HT films.

	Pristine	HHIC	Washed
Resistance (kΩ)	224.9±3.2	230.7±7.4	230.9±2.9
Ratios	← 2.54% →		
		← 0.11% →	
	← 2.66% →		

Although the exact mechanism of charge transport in organic (semi)conductors is still unknown (Horowitz et al., 2001; Horowitz, 2011), the majority of the scientific world tends to describe it in terms of delocalized charge hopping (i.e., tunneling). It is therefore possible that by lowering the intra-chain distance HHIC decreases the tunneling barrier and, in effect, increases the macroscopic current. This is unfortunately only a theory, which needs to be proven correct (or disproved) after the problem of harmful plasma radiation is solved.

Without any doubt, the HHIC method is an excellent tool for cross-linking of various organic moieties. Even for organic semiconductors the technique promises to deliver increased electronic performance. But it is quite uncertain how the HHIC method would perform in a model situation simulating a real device configuration. We have to remember that making an electronic device typically proceeds in multiple steps. We, thus, chose as a simple model a sandwich consisting of three polymer layers: top representing an insulator, poly(methyl methacrylate), middle representing a semiconductor, P3HT, and bottom, poly(ethylene terephthalate) as a substrate. In one case the P3HT film was cross-linked and in the other it was left as deposited. To document what changes the P3HT layer (and the sandwich as a whole) underwent, we employed the time-of-flight secondary ion mass spectroscopy to perform a depth profile

measurement. Characteristic signals were chosen to be atomic oxygen (present in both PMMA and PET), SH (P3HT), and two molecular fragments $C_7H_5O_2$ (not ideally representing PET) and $C_8H_{13}O_2$ (PMMA). The cross-linked P3HT layer easily survived a deposition of a PMMA layer as evidenced in Figure 43a by sharp transitions between neighboring layers. When the PMMA layer was deposited on top of an uncross-linked P3HT film, both polymers formed an indistinguishable blend.

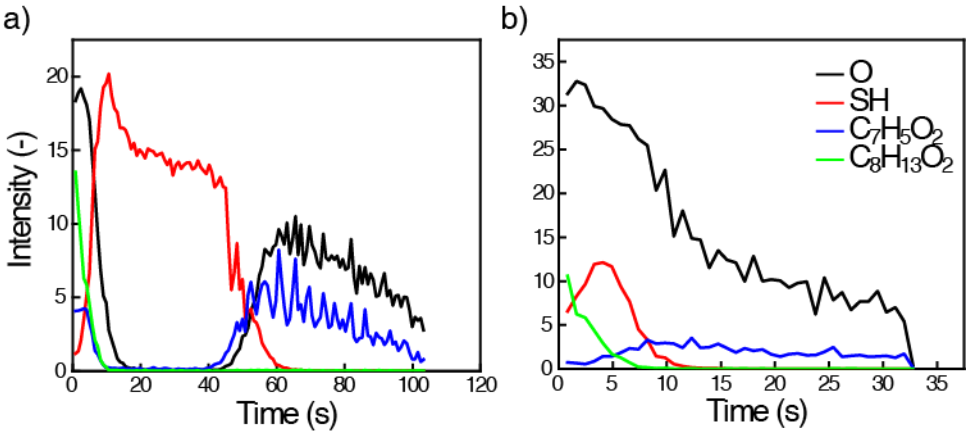

Figure 43. ToF-SIMS depth-profile data of a sandwich structure comprising (in order from top to bottom) cross-linked poly(methyl methacrylate) (green line), a) cross-linked, and b) uncross-linked P3HT (red line), and poly(ethylene terephthalate) (blue line).

3.3.3 Conclusion

The HHIC method is a very promising technique for cross-linking of materials used in organic electronic devices. Although in a current state it doesn't deliver a significant enhancement of electrical properties, it does accomplish material curing as evidenced by AFM and ToF-SIMS studies. It is true that the HHIC method is responsible for roughly a 3 percent decrease in resistance but considering that tolerances for ordinary discrete resistors range between 5 and 20%, the HHIC induced degradation is insignificant.

A major obstacle to a broad deployment of HHIC to (semi)conducting organic materials is plasma radiation. The photo-dissociation of S–C bond suggested by XPS and by the

loss of optical absorption loss has to be addressed. One possible way to solve this problem will be presented in Chapter 5.

3.4 Poly(acrylic acid)

The HHIC method was predicted to provide cross-linking with excellent selectivity toward various chemical functional groups. The concept of the HHIC method in synthesizing molecular films has already been demonstrated both with ab initio quantum chemistry calculations and partially with actual experiments. In this section, we aim to show the ability of the HHIC method to synthesize molecular films with hydrogen containing chemical functionalities. The impact is high because COOH, OH (binding dissociation energy, BDE=4.46 eV), NHx, and SH (BDE=3.66 eV) are among the most important chemical functional groups, and the kinematics considerations in the HHIC method expect hydrogen to recoil from both C–H and X–H groups. Whereas cleaving hydrogen in C–H (BDE=3.5 eV) bonds leads to the desirable formation of C–C cross-links, abstracting hydrogen from X–H groups may trigger undesirable side reactions that would compromise the merit of the HHIC method in preserving chemical functionalities of the precursor molecules during the cross-linking process.

The high chemical selectivity of the HHIC process was demonstrated through the treatment of thin films of poly(acrylic acid) (PAA), which was chosen for the high concentration of the COOH group because its loss and degradation can be quantified with a high level of confidence. In this example, a ~10 nm thick layer of PAA was prepared and subsequently cross-linked by HHIC. Although this layer was initially soluble, wash tests verified that it was converted into an insoluble and stable molecular network following HHIC treatment while preserving ~95% of the COOH groups as confirmed by XPS results.

3.4.1 Experimental setup

A solution of 0.3 wt.% of PAA in ethanol (HPLC grade purchased from EMD, used as received) was prepared and filtered through a 0.2 μm PTFE syringe filter. A thin layer of dotriacontane was deposited on silicon wafer chips by spin-casting of 50 μL of the

solution at 4000 RPM and acceleration 1490 RPM/s for 60 s and was followed by an XPS analysis.

XPS spectra were recorded on a Kratos Nova using a monochromatic Al Kα photon source at 10 mA and 14 kV. The analyzer used both electric and magnetic fields to focus secondary electrons. A size of the analysis area from which the secondary electrons were collected was $\sim 300 \times 700$ μm^2. Sample data were collected at a take-off angle of 0° (relative to the sample normal) and three different spots. Survey scans were conducted in order to confirm the exact elemental composition. Three survey scans per sample were collected for binding energies ranging from 0 to 1100 eV, energy step of 0.7 eV, pass energy 160 eV, and 60 s per scan. Ten high-resolution C 1s scans were collected for binding energies spanning 278–295 eV and fifteen high-resolution O 1s spectra were recorded at binding energies ranging from 520 to 540 eV, at the energy step of 0.1 eV, the pass energy 20 eV, and each scan lasted 60 s. CasaXPS version 2.3.15 was used for the analysis of all the XPS spectra. All spectra were referenced to the aliphatic C–H bond at 285 eV and the high-resolution C 1s peaks were fit using Gaussian to Lorentzian ratio of 40.

Hyperthermal hydrogen bombardment was carried out for a combination of the following parameters after reaching the background gas pressure of 2×10^{-6} Torr. The output microwave power was set to 200 W, $V_{acc} = -100$ V, $V_{r1} = 100$ V, $V_{r2} = -50$ V, $p = 0.8$ mTorr, $I_{acc} = 10$ mA. Samples were cross-linked for 10 s followed by a 2 min stay under vacuum.

Every sample underwent three XPS data collection cycles, one HHIC bombardment, and one washing step. XPS spectra were recorded: 1) on a fresh dotriacontane layer immediately after deposition; 2) after HHIC treatment; and 3) after washing. Washing of uncross-linked material was achieved by spin-casting of 50 μL of ethanol at 4000 RPM and acceleration 1490 RPM/s for 60 s. The washing step was repeated two times.

ToF-SIMS data were collected on an ION-TOF TOF-SIMS-IV instrument equipped with a Bi liquid metal ion source using a 25 keV $Bi3^+$ cluster primary ion beam pulsed at 10 kHz with a pulse width of 12 ns and a target current of 1 pA.

3.4.2 Results and discussion

Figure 44 shows the X-ray photoelectron spectroscopic evidence that virtually no acrylic acid groups (~95%) were damaged during the HHIC process. In comparison, ~27% of the acrylic acid groups were lost when the best plasma polymerization process to date was used to cross-link PAA (Friedrich et al., 2003). In fact, no other known method can cross-link PAA with less than 27% loss of the COOH groups. Similar results to those obtained by our group were reported by Zheng et al. using protons as hyperthermal projectiles.

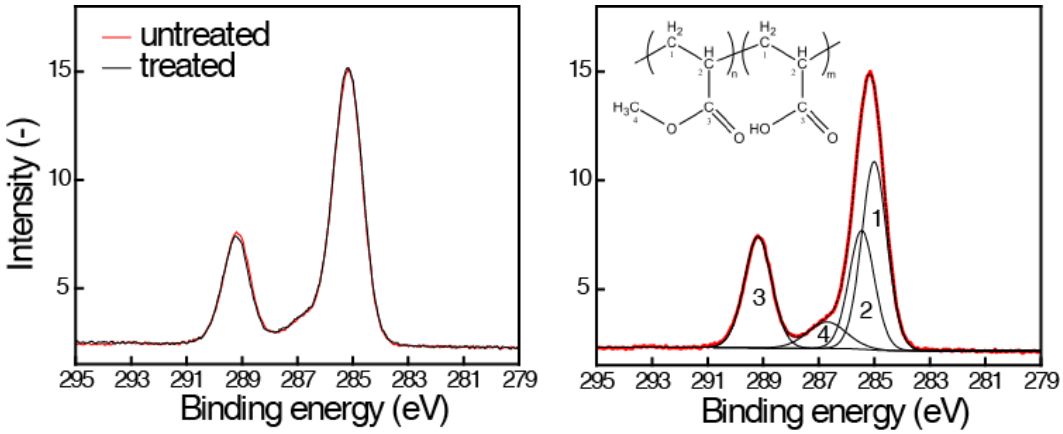

Figure 44. XPS high-resolution C 1s spectra of pristine and HHIC treated PAA showing over 95% retention of COOH functionality.

In the semiconductor industry, making electronic devices usually proceeds in multiple steps. Some of these steps require pattering of certain areas to shield them from the effects of applied processes. Because HHIC induces cross-linking by directing a flow of hyperthermal projectiles onto a sample, it was perceived that placing a shadow mask right above the sample should lead to preferential cross-linking of the exposed area. Figure 45 shows ToF-SIMS elemental maps of area 500×500 μm^2 for two negative ions: SiO_2H^- representing the silicon substrate, and C_6H^- representing cross-linked PAA. A clear pattern becomes visible after sample was washed. The result proves the feasibility of using shadow masks in conjunction with HHIC. In short, a selective-area patterning of cross-linked and insoluble PAA was accomplished.

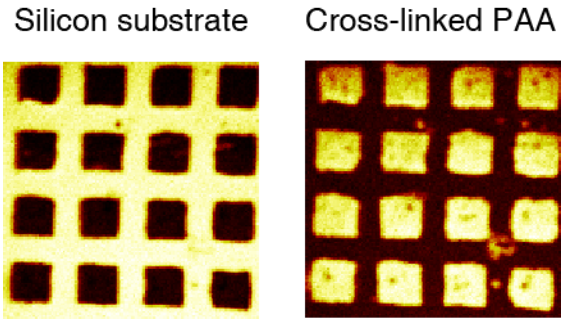

Figure 45. ToF-SIMS elemental maps of patterned PAA through HHIC treatment.

3.4.3 Conclusion

Any practical application that involves cross-linking of chemical moieties containing hydrogen bonded functional groups requires the curing process to preserve those functional groups. The HHIC method was tested on PAA, which has a high concentration of COOH, and was shown to perform excellently (~95% retention) by breaking exclusively the C–H bonds.

By applying a shadow mask to a PAA film and exposing it to hyperthermal hydrogen the HHIC method was shown to combine cross-linking and patterning into one single step. It goes without saying that pattern transfer is applicable to the production of chemical and biomedical sensors, or electronic devices.

References

Alet, P. J., Palacin, S., Cabarrocas, P. R. I., Kalache, B., et al.: 2006, *European Physical Journal-Applied Physics* **36**, 231-234

Beiny, D. H. M., Mullin, J. W. and Lewtas, K.: 1990, *Journal of Crystal Growth* **102**, 801-806

Boudinet, D., Le Blevennec, G., Serbutoviez, C., Verilhac, J. M., et al.: 2009, *Journal of Applied Physics* **105**

Braga, D. and Horowitz, G.: 2009, *Advanced Materials* **21**, 1473-1486

Cheng, Y. J., Liu, M. S., Zhang, Y., Niu, Y. H., et al.: 2008, *Chemistry of Materials* **20**, 413-422

Cho, N., Yip, H. L., Hau, S. K., Chen, K. S., et al.: 2011, *Journal of Materials Chemistry* **21**, 6956-6961

Cisternas, E. A., Corrales, T. P., del Campo, V., Soza, P. A., et al.: 2009, *Journal of Chemical Physics* **131**

Forch, R., Zhang, Z. H. and Knoll, W.: 2005, *Plasma Processes and Polymers* **2**, 351-372

Friedrich, J., Mix, R., Kuhn, G., Retzko, I., et al.: 2003, *Composite Interfaces* **10**, 173-223

Gelius, U. and et al.: 1971, *Physica Scripta* **3**, 237

Hegemann, D., Brunner, H. and Oehr, C.: 2003, *Nuclear Instruments & Methods in Physics Research Section B-Beam Interactions with Materials and Atoms* **208**, 281-286

Hill, J. M., Royce, D. G., Fadley, C. S., Wagner, L. F., et al.: 1976, *Chemical Physics Letters* **44**, 225-231

Himmelhuber, R., DeRose, C. C., Norwood, R. A. and Peyghambarian, N.: 2008, *UV-patternable inorganic-organic hybrid materials, tailored for the use in electro-optic modulators* as part of *Linear and Nonlinear Optics of Organic Materials Viii* **7049**, ISBN 0277-786

Hintz, H., Egelhaaf, H. J., Peisert, H. and Chasse, T.: 2010, *Polymer Degradation and Stability* **95**, 818-825

Horak, D., Shagotova, T., Mitina, N., Trchova, M., et al.: 2011, *Chemistry of Materials* **23**, 2637-2649

Horowitz, G.: 2004, *Journal of Materials Research* **19**, 1946-1962

Horowitz, G.: 2010, *Interfaces in Organic Field-Effect Transistors* as part of *Organic Electronics* **223**, ISBN 0065-3195

978-3-642-04538-7, 113-153

Horowitz, G.: 2011, *European Physical Journal-Applied Physics* **53**

Horowitz, G. and Hajlaoui, M. E.: 2001, *Synthetic Metals* **121**, 1349-1350

Horowitz, G., Kalb, W., Mottaghi, M., Lang, P., et al.: 2004, *Structure-performance relationship in pentacene-based thin-film transistors*, ISBN 0-7803-8304-4

Hwang, Y. J., Matthews, S., McCord, M. and Bourham, M.: 2004, *Journal of the Electrochemical Society* **151**, C495-C501

Ie, Y., Nitani, M., Tada, H. and Aso, Y.: 2010, *Organic Electronics* **11**, 1740-1745

Jia, H. P., Gross, E. K., Wallace, R. M. and Gnade, B. E.: 2007, *Organic Electronics* **8**, 44-50

Kalita, G., Masahiro, M., Koichi, W. and Umeno, M.: 2010, *Solid-State Electronics* **54**, 447-451

Kim, H., Yoon, B., Sung, J., Choi, D. G., et al.: 2008, *Journal of Materials Chemistry* **18**, 3489-3495

Kim, M. R., Shin, W. S., Kim, W. S., Lee, H. J., et al.: 2007, *Molecular Crystals and Liquid Crystals* **462**, 91-99

Klauk, H.: 2006, *Organic Electronics - Materials, Manufacturing and Applications*, Published by Wiley-VCH, Weinheim, ISBN 3527312641

Lao, H. K., Renard, E., El Fagui, A., Langlois, V., et al.: 2011, *Journal of Applied Polymer Science* **120**, 184-194

Liu, M. S., Niu, Y. H., Ka, J. W., Yip, H. L., et al.: 2008, *Macromolecules* **41**, 9570-9580

Ma, H., Yip, H. L., Huang, F. and Jen, A. K. Y.: 2010, *Advanced Functional Materials* **20**, 1371-1388

Mu, B., Shen, R. P. and Liu, P.: 2009, *Colloids and Surfaces B-Biointerfaces* **74**, 511-515

Pang, S. P., Tsao, H. N., Feng, X. L. and Mullen, K.: 2009, *Advanced Materials* **21**, 3488

Park, J. T., Koh, J. H., Seo, J. A., Cho, Y. S., et al.: 2011, *Applied Surface Science* **257**, 8301-8306

Park, S. K., Kim, Y. H., Han, J. I., Moon, D. G., et al.: 2003, *Synthetic Metals* **139**, 377-384

Qiu, W. L., Ma, X. H., Yang, Q. H., Fu, Y. B., et al.: 2005, *Journal of Materials Science-Materials in Electronics* **16**, 89-95

Rentenberger, S., Vollmer, A., Zojer, E., Schennach, R., et al.: 2006, *Journal of Applied Physics* **100**

Scarpa, G., Idzko, A. L., Gotz, S. and Thalhammer, S.: 2010, *Macromolecular Bioscience* **10**, 378-383

Seol, Y. G., Lee, J. G., Lee, N. E., Lee, S. S., et al.: 2007, *Thin Solid Films* **515**, 5065-5069

Shen, Y., Li, K. J., Majumdar, N., Campbell, J. C., et al.: 2011, *Solar Energy Materials and Solar Cells* **95**, 2314-2317

Sirringhaus, H., Tessler, N. and Friend, R. H.: 1998, *Science* **280**, 1741-1744

Suganuma, K., Watanabe, S., Gotou, T. and Ueno, K.: 2011, *Applied Physics Express* **4**

Tajima, S. and Komvopoulos, K.: 2007, *Journal of Applied Physics* **101**

Takimiya, K., Kunugi, Y., Konda, Y., Niihara, N., et al.: 2004, *Journal of the American Chemical Society* **126**, 5084-5085

Trogisch, S., Simpson, M. J., Taub, H., Volkmann, U. G., et al.: 2005, *Journal of Chemical Physics* **123**

Volkmann, U. G., Pino, M., Altamirano, L. A., Taub, H., et al.: 2002, *Journal of Chemical Physics* **116**, 2107-2115

Wang, J. G., Wang, Y. S., He, D. W., Liu, Z. Y., et al.: 2010, *Synthetic Metals* **160**, 2494-2500

Yaghmazadeh, O., Bonnassieux, Y., Saboundji, A., Horowitz, G., et al.: 2008, *Organic Thin-Film Transistors Modeling; Simulation and Design of a Fully Organic AMOLED Pixel Circuit*, ISBN 978-1-4244-1753-7

Yang, Y. S., Kim, S. H., Lim, S. C., Lee, J. I., et al.: 2003, *Applied Physics Letters* **83**, 3939-3941

Yip, H. L., Ma, H., Tian, Y. Q., Acton, O., et al.: 2011, *Journal of Materials Research* **26**, 311-321

Zhang, H., Shouro, D., Itoh, K., Takata, T., et al.: 2008, *Journal of Applied Polymer Science* **108**, 351-357

Zhang, Y., Zou, J. Y., Yip, H. L., Chen, K. S., et al.: 2011, *Macromolecules* **44**, 4752-4758

Zhao, Y., Di, C. A., Gao, X. K., Hu, Y. B., et al.: 2011, *Advanced Materials* **23**, 2448

Zheng, Z., Wong, K. W., Lau, W. C., Kwok, R. W. M., et al.: 2007, *Chemistry-a European Journal* **13**, 3187-3192

Zimmermann, B., Wurfel, U. and Niggemann, M.: 2009, *Solar Energy Materials and Solar Cells* **93**, 491-496

Zou, J. Y., Yip, H. L., Hau, S. K. and Jen, A. K. Y.: 2010, *Applied Physics Letters* **96**

Chapter 4

4 Functional polymer laminates

4.1 Introduction

The low cost and ease of processing polyolefins (also known as polyalkenes with a general formula C_nH_{2n}) make them attractive materials for applications ranging from beverage containers to medical devices. While the bulk properties of these polymers are often favorable, some properties such as gas permeability and poor adhesiveness can complicate their use in certain applications (Brewis et al., 2002; Denes et al., 2004). Switching to higher performance polymers such as butyl rubber, silicones or fluoropolymers can overcome some, but not all, of these limitations. However, the higher overall cost and unique bulk properties of these materials can make their use impractical. In light of this, a large body of work has been undertaken to expand the available methods for chemical functionalization of polymer surfaces. Wet chemical methods such as hydrolysis or oxidation can be used, but these reactions are relatively nonspecific, leading to a range of functional groups and the results depend on the nature of the polymer surface (Mathieson et al., 1995; Desai et al., 2004; Goddard et al., 2007; Jiao et al., 2007). UV initiated polymerizations of monomers from surfaces in the presence of a photoinitiator or photosensitizer have been extensively investigated (Kato et al., 2003; Deng et al., 2009), while recent work has demonstrated that the functionalization of surfaces with polymer brushes via controlled surface initiated polymerizations such as atom transfer radical polymerization (ATRP) and reversible addition-fragmentation chain transfer polymerization can provide high levels of functionality and good control (Edmondson et al., 2004; Huang et al., 2007; Ranjan et al., 2007). However, the introduction of the initiators required for these polymerizations onto polymer surfaces in the latter case requires extra steps and the excesses of reagents and solvents required for these polymerizations may limit their applicability on large scale.

Various plasma methods have also been used to functionalize polymer surfaces either via the generation of the required reactive species above the substrate surface and/or by the

creation of radicals on the surface (Schonhorn et al., 1967; Yasuda, 1985; Yu et al., 1998; Yasuda et al., 2001; Biederman, 2004; Siow et al., 2006; Desmet et al., 2009). Plasma techniques can indeed allow for the incorporation of desired functionalities very effectively on otherwise non-functional polymer substrates. Unfortunately, these plasma techniques are frequently harsh and can ablate the surface, compromising the physical properties of the substrate. More problematically, multiple reactive species are often present in these plasma environments, which bars the surface engineering of a single chemical functionality or a precise set of functionalities. To harness the plasma process and reduce undesirable side-reactions, the method of "Cross-linking with Activated Species from INert Gas" (CASING) was developed such that the sample to be treated is placed downstream and remote from the plasma, and its surface is exposed to excited inert gas atoms flowing down from the plasma to conduct the cross-linking reaction (Schonhorn et al., 1967; Yu et al., 1998; Yasuda et al., 2001). Nevertheless, even well-engineered plasma techniques still give considerable heterogeneity in chemical functionality and cannot support any chemical or biochemical applications that require single chemical functionality or a precise composition of multiple functionalities (Siow et al., 2006; Desmet et al., 2009) because the reactive plasma species unavoidably reach the sample.

When applied to the cross-linking of materials coated on a polymer substrate, the HHIC technique opens many new possibilities for the modification of polymer surfaces. Crucially, the HHIC technique as applied to surface modification using polymers is additive, rather than ablative. This should make it possible to rigorously characterize polymers prior to their coating and cross-linking at the surface, allowing for greater control of morphology and composition than is typically available from plasma treatments. Moreover, the additive nature of this technique should permit successive cross-linking of multiple different materials at a surface, creating laminate materials. Such layered architectures, particularly with polyolefin materials, represent an ongoing challenge (Xu et al., 2009).

Described here is the first application of HHIC for the preparation of functional polymer laminates (Figure 46). Bi-axially oriented polypropylene (BOPP) was used as a model

polyolefin substrate. Poly(isobutylene-co-isoprene) commonly referred to as butyl rubber (Bu), a commercially relevant polymer with interesting properties such as gas impermeability, was chosen as the next layer to demonstrate the lamination process. While many properties of butyl rubber are advantageous, it would be useful to reduce its hydrophobicity for some applications, particularly in biological systems (Puskas et al., 2004). In theory, this could be accomplished by cross-linking a hydrophilic polymer such as poly(vinyl alcohol) (PVA) at the Bu surface using HHIC. Unfortunately, the mutual incompatibility of PVA and Bu preclude the formation of a uniform and cohesive layer of PVA at the surface. Thus poly(vinyl acetate) (PVAc) was selected as the third layer as it can subsequently be hydrolyzed to PVA. In addition, the choice of PVAc allows for an evaluation of the functional group tolerance of HHIC, as there have been no reported cases of plasma technologies successfully grafting this molecule to a surface with any significant retention of the ester functionality, though some groups have retained some functionality by polymerizing the monomer from a surface using solution methods (Faibish et al., 2002; Yoshida et al., 2003; Tan et al., 2004). Thus, the choice of these three layers allows for the full utility of the HHIC process to be demonstrated. Each layer of the laminate was thoroughly characterized and it was also demonstrated that chemical reactions could be performed on the PVAc layer in order to alter the surface reactivity and wettability.

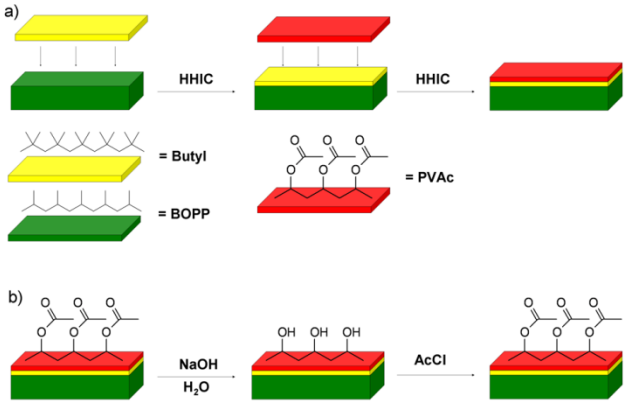

Figure 46. Schematic diagram of a) the preparation of laminates using HHIC and b) chemical transformations of the PVAc layer.

4.2 Experimental setup

LANXESS Butyl 101-3 (Bu) was a gift from LANXESS Inc. PVAc (MW ca. 100,000) was purchased from Aldrich. Hexanes, ethyl acetate and sodium hydroxide were purchased from Caledon. All polymers, reagents and solvents were used as delivered. ATR-FTIR spectra were collected using a Bruker IFS55 spectrometer using the micro-attenuated total reflectance (micro-ATR) attachment equipped with a germanium crystal on the IRScope II microscope. Time-of-flight secondary ion mass spectroscopy (ToF-SIMS) data were collected on an ION-TOF TOF-SIMS-IV instrument equipped with a Bi liquid metal ion source using a 25keV $Bi3^+$ cluster primary ion beam pulsed at 10kHz with a pulse width of 12 ns with a target current of 1 pA.

Atomic force microscopy (AFM) experiments were performed on a Dimension V AFM system with a Nanoscope V controller from Veeco Inc., which was equipped with a HarmoniX mapping module. The tip used for the torsional harmonic mode was T-shaped with a tip radius of 8 nm as calibrated by the blunt method via the SPIP software (Image Metrology); and its spring constant of 2.76 N/m was calibrated by the thermal fluctuation method (Butt et al., 1995). Young's modulus was calibrated on a PS-LDPE calibration sample (Veeco Inc.) before, during and after experiments. Topography and Young's Modulus were collected simultaneously on the BOPP and Bu/BOPP samples.

X-ray photoelectron spectroscopy (XPS) spectra were recorded on a Kratos AXIS Ultra instrument using a monochromatic Al Kα photon source at 10 mA and 14 kV. Sample data was collected at a take-off angle of 90°. Survey scans were conducted in order to confirm the sole presence of carbon and oxygen species, which were then analyzed at higher resolution. CasaXPS version 2.3.15 was used for the analysis of all the XPS spectra. All spectra were referenced to the aliphatic C–H bond of 285 eV and fitting was accomplished using a Gaussian and Lorentzian ratio of 40. The peak areas of the beta-shifted C–H bonds (285.5 eV) were constrained to be equal to the area of the ester (289.2 eV), and the aldehyde peak was constrained to fall within 0.1 eV of the 288 eV. Peak FWHW (full width at half maximum) was constrained to fall within 0.9–1.4. All other components were allowed to refine freely.

Samples were inserted into a the HHIC reactor and pumped down to a background pressure of 2×10^{-6} Torr. Hydrogen gas was then introduced inside the reactor until a pressure of 0.8 mTorr was reached and maintained throughout the experiment. An ECR microwave plasma (87.5 mT, 2.45 GHz) was set up in the vacuum part of the plasma system. Residual electrons and positive ions were repelled in two stages with an applied voltage of +100 V and −50 V, respectively. The samples were exposed to hyperthermal H_2 neutrals for 30 s. Based on these values and an extraction current of 7 mA, the fluence of hyperthermal neutrals was sufficient to cross-link the polymeric layer to the extent that the solubility of the precursor molecules in common organic solvents (hexanes, heptane, chloroform, etc.) decreased to the level of no materials loss in a brief wash of ~5 minutes.

Surface Science Western provided BOPP films of area $25 \times 25\ mm^2$ originally purchased from 3M, which were affixed to glass slides of the same dimensions using a carbon-adhesive disk. LANXESS Butyl 101-3 (56.0 mg) was dissolved in hexanes (10.0 mL), and this solution (0.2 mL) was used to flood the BOPP films by means of a syringe equipped with a 0.2 μm PTFE filter. The surfaces were then spun to 6000 RPM at an acceleration of 1620 RPM/s for 60 s. The resulting films were cross-linked using the HHIC reactor. The cross-linked surfaces were rinsed with hexanes (5×10 mL aliquots) and blown dry with compressed argon.

BOPP/Bu surfaces as above were flooded (0.2 mL) with a solution of poly(vinyl acetate) (63.1 mg) in ethyl acetate (12.5 mL) by means of a syringe equipped with a 0.2 μm PTFE filter. The surfaces were then spun to 6000 RPM at an acceleration of 1620 RPM/s for 60 s. The resulting films were cross-linked using the HHIC reactor. The cross-linked surfaces were rinsed with ethyl acetate (5×10 mL aliquots) and blown dry with compressed argon.

A solution of sodium hydroxide (NaOH, 5.56 g) in water (200 mL) was prepared. This solution was used to flood the surface of PVAc/Bu/BOPP surfaces described above. The flooded surfaces were placed under an inverted beaker to prevent evaporation and left for 24 hours. The resulting surfaces were rinsed with 5×2 mL aliquots of 25% acetic acid in H_2O, followed by 2×10 mL H_2O, and blown dry with compressed argon.

PVA/Bu/BOPP surfaces from above were surface coated with acetyl chloride (~0.5 mL), and placed under an inverted beaker for 4 hours. The resulting surfaces were rinsed with 2×5 mL of ethyl acetate, followed by 2×10 mL water. Residual solvent was removed by blowing with dry compressed argon.

4.3 Results and discussion

Bi-axially oriented polypropylene was used as a model polyolefin substrate. For the initial surface modification, the BOPP was spin coated with a 5 mg/mL solution of LANXESS butyl 101-3 (Bu), a commercially available food-grade butyl rubber, in hexanes. This solution was filtered through a 0.2 μm PTFE filter to remove inorganic additives prior to the spin coating. The resulting coated surfaces were subjected to the HHIC treatment for 30 s, and were then washed thoroughly with hexanes. While the somewhat delicate fibrous surface of BOPP made direct measurements of the film thickness difficult, atomic force microscopy (AFM) trials on silicon wafers suggested a film thickness of approximately 15–20 nm was formed using the same concentration and spin coating speeds. This was the target film thickness as the estimated depth of cross-linking is expected to be approximately 15 nm (Zheng et al., 2004; Zheng et al., 2006; Zheng et al., 2007; Liu et al., 2011). As shown in Figure 47, AFM measurements of the virgin BOPP sheets clearly showed fibers of polypropylene. After the spin coating and HHIC treatment these fibers were no longer visible and the surface was much smoother. When the butyl coated surfaces were not cross-linked, washing with hexanes resulted in restoration of the BOPP surface. Measurement of the Young's Modulus of both the BOPP and Bu/BOPP samples provided additional characterization of the surfaces. The BOPP had a measured hardness of 2.1 GPa, whereas the Bu/BOPP surface showed a significantly reduced modulus of 39 MPa owing to the elastomeric nature of the butyl rubber. Time-of-flight secondary ion mass spectrometry was also used to analyze the HHIC treated surfaces, and the isobutylene repeat unit was visible in the spectrum. In contrast, the films formed on control samples that were not treated with HHIC were shown by TOF-SIMS to be removed in the washing step. Together these data provide conclusive evidence that the butyl was indeed cross-linked to the BOPP surface.

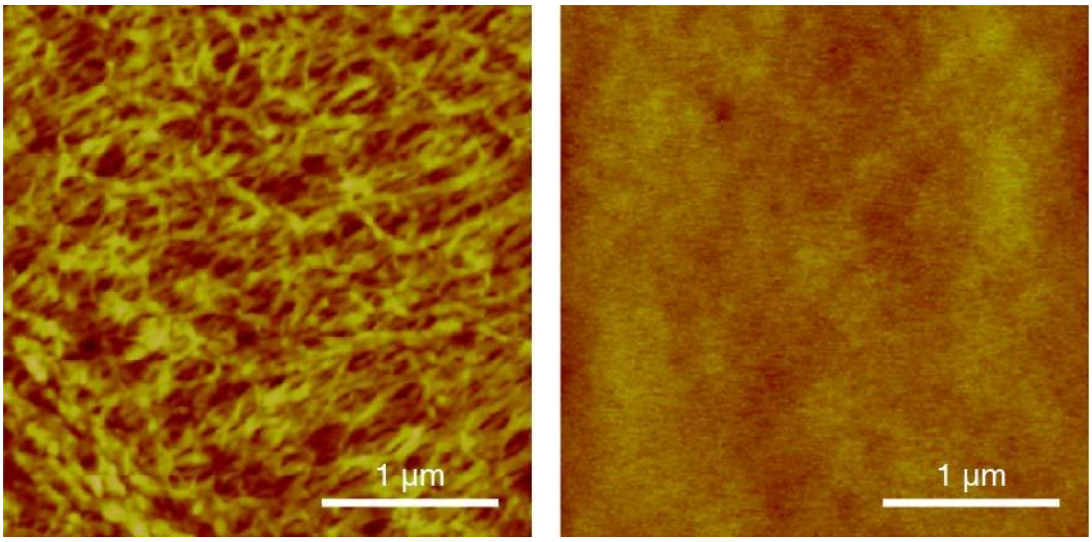

Figure 47. AFM topography images of BOPP surface (left) and Bu/BOPP surface after HHIC (right).

PVAc (5 mg/mL) in ethyl acetate was then spin coated onto the Bu/BOPP surface. The surface was dried, and then treated with HHIC for 30 s. The surface was then washed to remove any material that was not cross-linked, and the resulting surface was dried. Attenuated total reflectance Fourier transform infrared (ATR-FTIR) spectroscopy was performed before and after the HHIC treatment. Figure 48 depicts ATR-FTIR spectra showing changes in chemical functionalities at surface layers: a) cross-linked Bu/BOPP; b) cross-linked PVAc/Bu/BOPP; c) hydrolysis gave PVA/Bu/BOPP; and d) treatment of PVA/Bu/BOPP with acetyl chloride restored ester functional groups. As shown in Figure 48, in comparison with the Bu/BOPP surface, new peaks corresponding to the ester of PVAc were clearly present at 1742 and 1255 cm^{-1} in the sample that was treated with HHIC, thus confirming the effectiveness of the cross-linking process and also demonstrating that the ester functionality was not destroyed in the HHIC process.

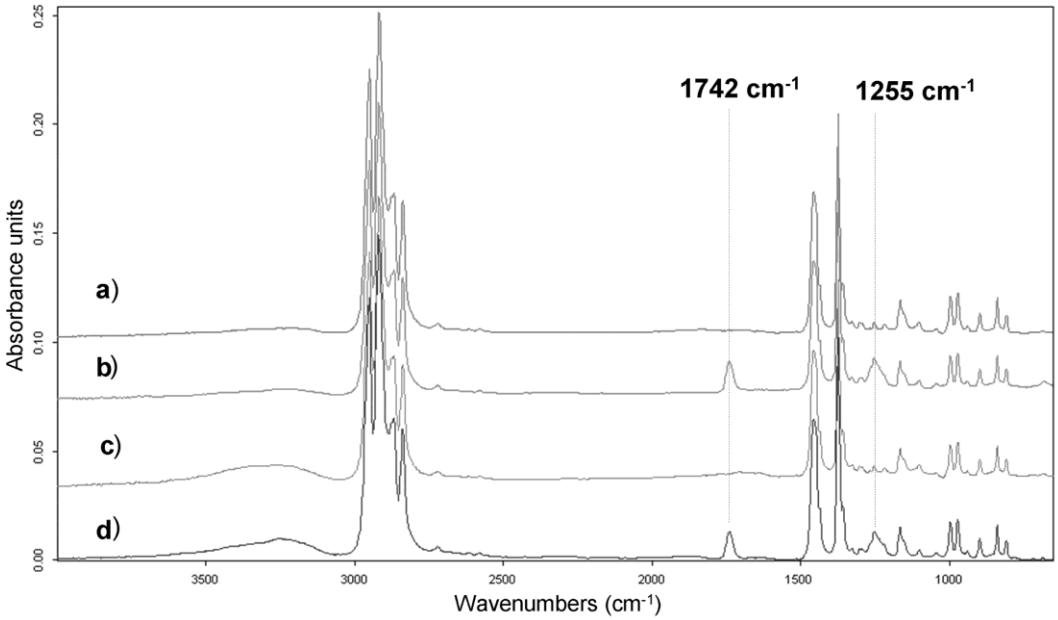

Figure 48. ATR-FTIR spectra showing changes in chemical functionalities at surface layers: a) cross-linked Bu/BOPP; b) cross-linked PVAc/Bu/BOPP; c) hydrolysis gave PVA/Bu/BOPP; d) treatment of PVA/Bu/BOPP with acetyl chloride restored ester functional groups.

X-ray photoelectron spectroscopy also verified the presence of the PVAc on the surface following the cross-linking and washing steps and high-resolution spectra of C 1s and O 1s regions demonstrated that the ester functionalities were not chemically modified as shown in Figure 49 for a) cross-linked Bu/BOPP surface, b) cross-linked PVAc/Bu/BOPP surface, c) NaOH treated PVAc/Bu/BOPP surface showing PVA formation, d) re-esterified surface after acetyl chloride (AcCl) treatment of PVA/Bu/BOPP. Control samples that were spin coated with PVAc, but not cross-linked did not reveal ester peaks in the ATR-FTIR spectra after washing.

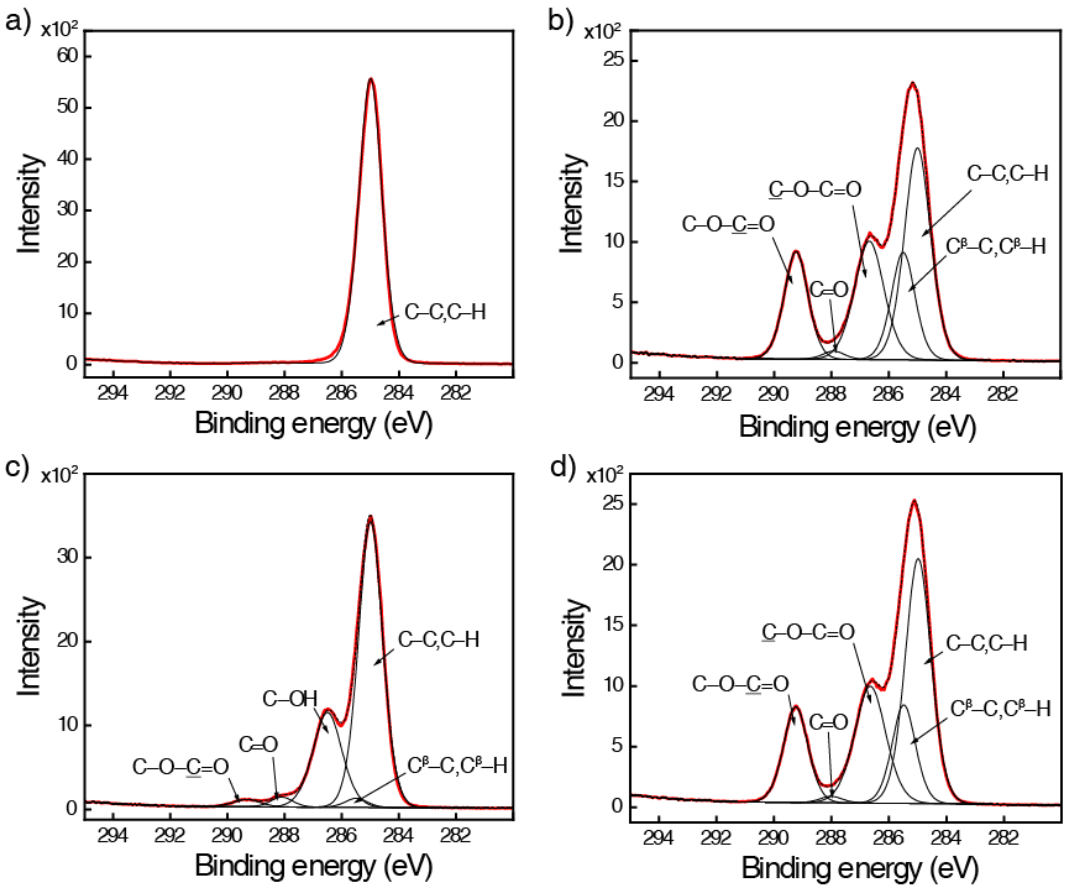

Figure 49. High-resolution XPS spectra of the C 1s region showing C–C,C–H, beta shifted C^{β}–C,C^{β}–H, C–O-C=O, C=O, and C–O–C=O species for a) cross-linked Bu/BOPP surface, b) cross-linked PVAc/Bu/BOPP surface, c) NaOH treated PVAc/Bu/BOPP surface showing PVA formation, d) re-esterified surface after acetyl chloride (AcCl) treatment of PVA/Bu/BOPP. The red line represents the actual spectrum, the thin black line represents GL fitting curve, and the dashed black line represents a sum of individual fitting curves.

Having created a three-layer polymer laminate with intact surface functionalities, it was of interest to determine if these functional groups were available for subsequent reactions. In particular, the ability to deprotect the PVAc layer, affording a hydrophilic PVA surface, would potentially allow for further layers of cross-linked hydrophilic polymers to be added. With this in mind, PVAc/Bu/BOPP samples were exposed to a 0.5 M NaOH solution for 12 hours, and then were washed with 10 mL aliquots of 25% acetic acid and 2×10 mL of water. ATR-FTIR spectroscopy confirmed that the hydrolysis

reaction had taken place, showing removal of the carbonyl signals (Figure 48c). In addition, measurements of the hydrolyzed surfaces gave a receding contact angle of 20°, a decrease of 25° from the PVAc surface and 51° less than the cross-linked butyl surface. The results are summarized in Figure 50 for a) BOPP, b) Bu/BOPP, c) PVAc/Bu/BOPP, d) PVA/Bu/BOPP, e) PVA/Bu/BOPP aged 3 days, and f) PVA/Bu/BOPP treated with AcCl to give back PVAc/Bu/BOPP. Importantly, contact angle measurements taken 3 days after the hydrolysis showed little or no change. This indicates that unlike conventional plasma surface oxidations, hydrophobic recovery, also referred to as surface reversion (see for example Moosheimer et al., 1999; Stefecka et al., 2003), did not occur. In many plasma surface treatments, the obtained hydrophilic surface will recover to the original hydrophobic state in a matter of hours (Behnisch et al., 1993). While the individual hydroxyl groups on a plasma oxidized surface can be easily taken into the surface to present a lower energy hydrophobic air interface, the functional layer provided by hydrolysis of the HHIC treated PVAc cannot be readily absorbed below the surface.

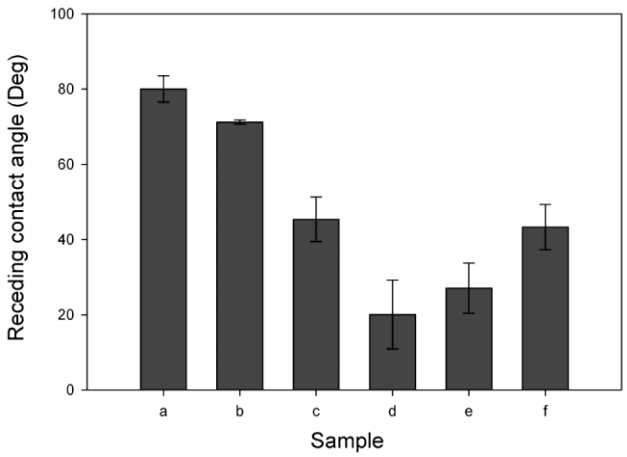

Figure 50. Receding contact angle measurements of polymer surfaces for a) BOPP, b) Bu/BOPP, c) PVAc/Bu/BOPP, d) PVA/Bu/BOPP, e) PVA/Bu/BOPP aged 3 days, and f) PVA/Bu/BOPP treated with AcCl to give back PVAc/Bu/BOPP.

An analysis of high-resolution XPS C 1s spectra showed a significant intensity reduction of the ester carbonyl peak (Figure 49c). Also a high-resolution O 1s spectrum of the hydrolyzed sample showed only one signature peak, confirming the presence of PVA on the surface. The results are summarized in Figure 51 showing a) cross-linked

PVAc/Bu/BOPP surface, and b) NaOH treated PVAc/Bu/BOPP surface with PVA formation.

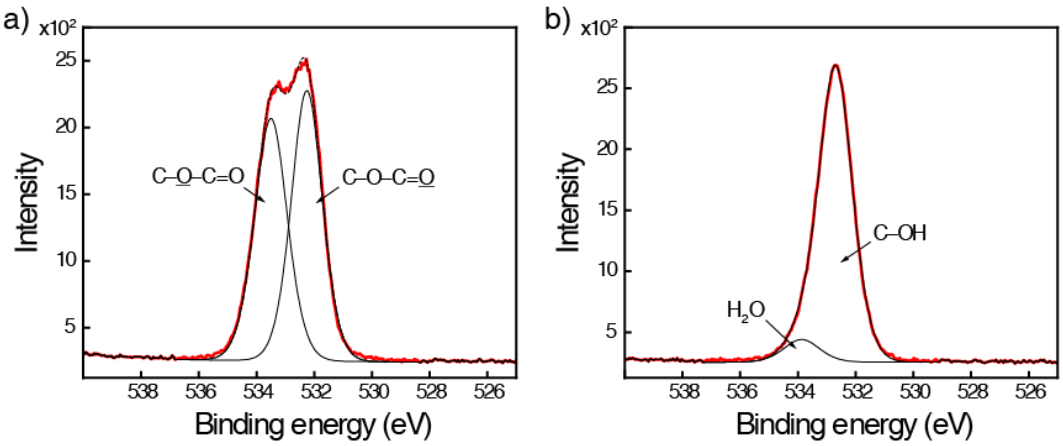

Figure 51. High-resolution XPS spectra of the O 1s region showing C–O–C=O, C–O–C=O, and H_2O species for a) cross-linked PVAc/Bu/BOPP surface, and b) NaOH treated PVAc/Bu/BOPP surface showing PVA formation.

Final confirmation of the presence of a PVA layer was obtained through chemical derivatization. Surface treatment with acetyl chloride (AcCl) caused the reappearance of the ester signal in the ATR-IR spectrum as shown in Figure 48d, with a corresponding increase in the receding contact angle as shown in Figure 50f. Control Bu/BOPP surfaces showed no change on treatment with AcCl. This result also confirms that the hydroxyl groups on the PVA/Bu/BOPP surface are chemically reactive and suggests that they can be used for introducing a wide variety of chemical functionalities onto the polymer laminates. This result was also confirmed by high-resolution XPS spectra of the C 1s (Figure 49d) and O 1s regions (Figure 51).

In order to present a complete picture of the process of laminates preparation, it is necessary to show control samples relevant to those steps that might raise questions as to whether or not there are other potential chemical reactions responsible for the presented results. The high-resolution C 1s XPS spectra in Figure 52 show a) cross-linked Bu/BOPP surface, b) washed uncross-linked PVAc/Bu/BOPP surface, c) AcCl treated cross-linked Bu/BOPP surface, d) NaOH treated cross-linked Bu/BOPP surface, e) AcCl and NaOH treated cross-linked BOPP surface, and f) NaOH treated cross-linked BOPP

surface. It shows Bu/BOPP and PP materials exposed to both AcCl and NaOH treatments to confirm that the reaction of a solvent with the substrate does not change its chemical composition. Indeed, NaOH and AcCl only reacts with PVAc and PVA surfaces.

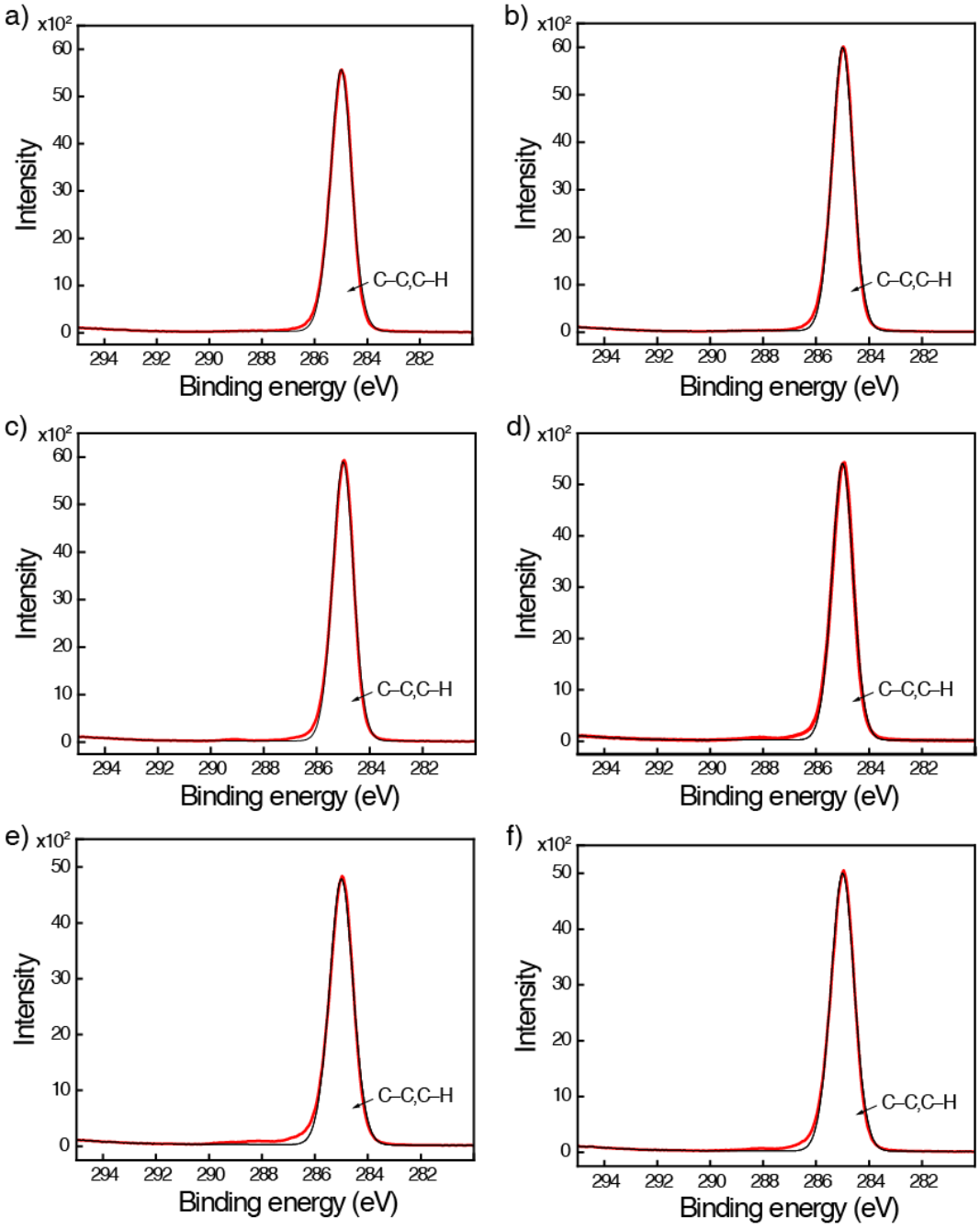

Figure 52. High-resolution XPS control spectra of the C 1s region showing C–C,C–H species for a) cross-linked Bu/BOPP surface, b) washed uncross-linked

PVAc/Bu/BOPP surface, c) AcCl treated cross-linked Bu/BOPP surface, d) NaOH treated cross-linked Bu/BOPP surface, e) AcCl and NaOH treated cross-linked BOPP surface, and f) NaOH treated cross-linked BOPP surface.

The XPS results beautifully depict the changes which are occurring to the surfaces after each step. It is clear from Table 4 that the Bu/BOPP film once spin-coated with PVAc and cross-linked using HHIC forms the desired PVAc layer on the surface. While there is some variation from the expected 25% ratio of each peak, the deviations are rather small and could be a result of the cross-linking subtly changing the electronic environment of the surface bound PVAc. Perhaps the most important metric is that the sum of all C–H and C–O bonds is very close to the expected 1:1 ratio for PVAc demonstrating that this technique is able to retain most of the chemical functionality. Once the surface is treated with NaOH, hydrolysis of the ester results in a near complete loss of the ester functionality (17.7 % to 1.9%). The remaining functionality is attributed to either ester bonds that were inaccessible to the NaOH or to the cross-linking of a small percentage of the ester groups to the surface, which would result in carboxylic acid formation after hydrolysis. Again, the sum total of the C–H and C–O groups is very close to the expected 2:1 ratio (2.2:1). The high resolution O 1s spectrum (Figure 51b) also shows the nearly complete loss of the ester function yielding the singular alcohol peak. Treatment of the PVA surface with acetyl chloride restored the ester group with only a small portion not re-forming as would be expected on the sterically constrained surface. Overall, there was only ~2% difference between the pre-hydrolyzed surface and the re-esterified surface (56.5% C–H before, 58.7% C–H after).

Table 4. XPS results showing area percentages for components of C 1s and O 1s peaks.

	Hi-Res C 1s (%)						Hi-Res O 1s (%)	
	C–C C–H	C^{β}–C C^{β}–H	C–O–C=O	Aldehyde	C–O–C=O / alcohol	Sum C–H	Sum C–O	Ester	Ester / alcohol
Bu/BOPP	100	0	0	0	0	100	0	-	-
PVAc standard	28.33	22.36	26.34	0.65	22.32	50.9	49.1	51.49	48.51
PVAc/Bu/BOPP	38.76	17.78	24.46	1.26	17.74	56.5	43.5	48.56	51.44
PVAc/Bu/BOPP NaOH treated	67.14	1.95	26.84	2.13	1.94	69.1	30.9	7.59	92.41
PVA/Bu/BOPP AcCl treated	42.90	15.76	24.65	0.97	15.72	58.7	41.3	49.68	50.32

With respect to the mildness of the HHIC process, a cross-linked PVAc/Bu/BOPP surface was compared to a sample of pure PVAc to determine what changes, if any, were occurring (Figure 53 showing a) cross-linked PVAc/Bu/BOPP and b) PVAc standard surface.). While the spectra are visually similar, there are some differences, which become more apparent when examining the fitted components. Overall, there appears to be a slight reduction in the oxygen content after the HHIC process (49.1 % vs. 43.5%). This reduction is likely the result of some yet undetermined radical chemistry occurring at the surface, as even though HHIC is designed only to induce radicals at C–H bonds, once formed they are free to react with any nearby atoms including oxygen. Nevertheless, the level of retained functionality is still very high relative to plasma processes involving similar chemical functionalities (as observed by Lens et al., 1997; Evenson et al., 2000; Kelly et al., 2003; Zhang et al., 2003; Swaraj et al., 2005; O'Hare et al., 2006; Chapman et al., 2008; Leber et al., 2009).

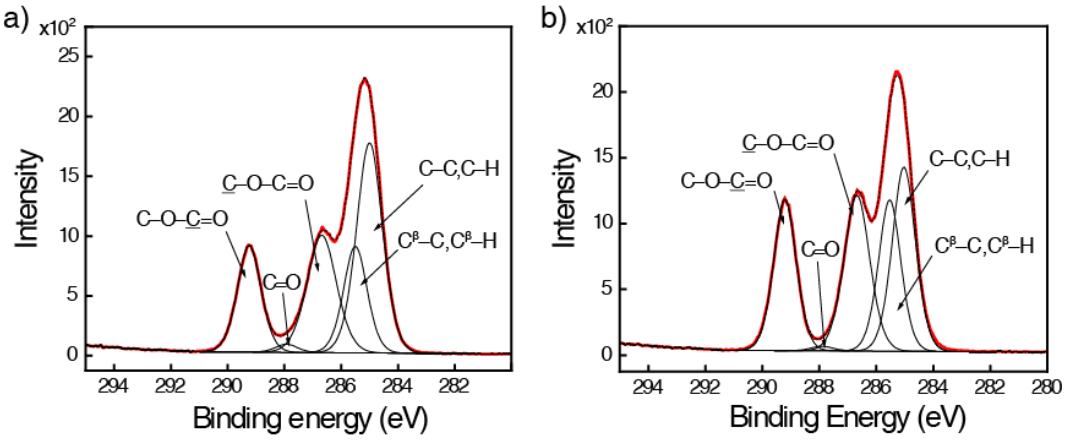

Figure 53. High resolution XPS spectra of the C 1s region showing C–C,C–H, beta shifted C^{β}–C,C^{β}–H, C-O-C=O, C=O, and C-O-C=O species of: a) cross-linked PVAc/Bu/BOPP and b) PVAc standard surface.

4.4 Conclusion

In summary, it was demonstrated that hyperthermal hydrogen-induced cross-linking shows great promise for the additive surface modification of polymer substrates with either non-functional materials with desired performance parameters, or functional materials to tune surface properties or allow subsequent chemical modification.

Functional laminate materials were readily prepared, and were extensively characterized by XPS, ATR-IR, and contact angle measurements. Notably, the hydrophilic surfaces prepared using this method show a reduced tendency towards hydrophobic recovery compared to conventional plasma treatments. In addition, a high level of chemical functionalities were retained on the surface throughout the process, as revealed by XPS.

References

Behnisch, J., Hollander, A. and Zimmermann, H.: 1993, *Surface & Coatings Technology* **59**, 356-358

Biederman, H.: 2004, *Plasma polymer films*, Published by Imperial College Press, ISBN 9781860944673

Brewis, D. M. and Mathieson, I.: 2002, *Adhesion and bonding to polyolefins*, Published by Rapra Technology Ltd., ISBN 9781859573235

Butt, H. J. and Jaschke, M.: 1995, *Nanotechnology* **6**, 1-7

Chapman, C. L., Bhattacharyya, D., Eberhart, R. C., Timmons, R. B., et al.: 2008, *Journal of Membrane Science* **318**, 137-144

Denes, F. S. and Manolache, S.: 2004, *Progress In Polymer Science* **29**, 815-885

Deng, J., Wang, L., Liu, L. and Yang, W.: 2009, *Progress In Polymer Science* **34**, 156-193

Desai, S. M. and Singh, R. P.: 2004, *Long-Term Properties of Polyolefins* **169**, 231-293

Desmet, T., Morent, R., De Geyter, N., Leys, C., et al.: 2009, *Biomacromolecules* **10**, 2351-2378

Edmondson, S., Osborne, V. L. and Huck, W. T. S.: 2004, *Chemical Society Reviews* **33**, 14-22

Evenson, S. A., Fail, C. A. and Badyal, J. P. S.: 2000, *Chemistry of Materials* **12**, 3038-3043

Faibish, R. S., Yoshida, W. and Cohen, Y.: 2002, *Journal of Colloid and Interface Science* **256**, 341-350

Goddard, J. M. and Hotchkiss, J. H.: 2007, *Progress In Polymer Science* **32**, 698-725

Huang, J. Y., Murata, H., Koepsel, R. R., Russell, A. J., et al.: 2007, *Biomacromolecules* **8**, 1396-1399

Jiao, Y. P. and Cui, F. Z.: 2007, *Biomedical Materials* **2**, R24-R37

Kato, K., Uchida, E., Kang, E. T., Uyama, Y., et al.: 2003, *Progress In Polymer Science* **28**, 209-259

Kelly, J. M., Short, R. D. and Alexander, M. R.: 2003, *Polymer* **44**, 3173-3176

Leber, E. R. and Ratner, B. D.: 2009, *Plasma Processes and Polymers* **6**, 219-227

Lens, J. P., Terlingen, J. G. A., Engbers, G. H. M. and Feijen, J.: 1997, *Langmuir* **13**, 7052-7062

Liu, Y., Yang, D. Q., Nie, H. Y., Lau, W. M., et al.: 2011, *Journal of Chemical Physics* **134**

Mathieson, I. and Bradley, R. H.: 1995, *EFFECTS OF ULTRA-VIOLET OZONE OXIDATION ON THE SURFACE-CHEMISTRY OF POLYMER-FILMS* as part of *Advances in Engineering Materials* **99-1**, Published by TRANS TECH PUBLICATIONS, ISBN 0252-1059

Moosheimer, U. and Bichler, C.: 1999, *Surface & Coatings Technology* **116**, 812-819

O'Hare, L.-A., O'Neill, L. and Goodwin, A. J.: 2006, *Surface and Interface Analysis* **38**, 1519-1524

Puskas, J. E., Chen, Y. H., Dahman, Y. and Padavan, D.: 2004, *Journal of Polymer Science Part a-Polymer Chemistry* **42**, 3091-3109

Ranjan, R. and Brittain, W. J.: 2007, *Macromolecular Rapid Communications* **28**, 2084-2089

Schonhorn, H. and Hansen, R. H.: 1967, *Journal of Applied Polymer Science* **11**, 1461

Siow, K. S., Britcher, L., Kumar, S. and Griesser, H. J.: 2006, *Plasma Processes and Polymers* **3**, 392-418

Stefecka, M., Kando, M., Cernak, M., Korzec, D., et al.: 2003, *Surface & Coatings Technology* **174**, 553-558

Swaraj, S., Oran, U., Lippitz, A., Friedrich, J. F., et al.: 2005, *Plasma Processes and Polymers* **2**, 572-580

Tan, L., Deng, J. and Yang, W.: 2004, *Polym. Adv. Technol.* **15**, 523-527

Xu, L., Nakajima, H., Manias, E. and Krishnamoorti, R.: 2009, *Macromolecules* **42**, 3795-3803

Yasuda, H.: 1985, *Plasma polymerization*, Published by Academic Press, ISBN 0127687602

Yasuda, H. K., Lin, Y. S. and Yu, Q. S.: 2001, *Progress in Organic Coatings* **42**, 236-243

Yoshida, W. and Cohen, Y.: 2003, *Journal of Membrane Science* **215**, 249-264

Yu, Q. S., Krentsel, E. and Yasuda, H. K.: 1998, *Journal of Polymer Science Part a-Polymer Chemistry* **36**, 1583-1592

Zhang, J., Feng, X. F., Xie, H. K., Shi, Y. C., et al.: 2003, *Thin Solid Films* **435**, 108-115

Zheng, Z., Kwok, W. M. and Lau, W. M.: 2006, *Chemical Communications* 3122-3124

Zheng, Z., Wong, K. W., Lau, W. C., Kwok, R. W. M., et al.: 2007, *Chemistry-a European Journal* **13**, 3187-3192

Zheng, Z., Xu, X. D., Fan, X. L., Lau, W. M., et al.: 2004, *Journal of the American Chemical Society* **126**, 12336-12342

Chapter 5

5 Summary and outlook

It has been shown that the HHIC method is a novel, dry-reaction approach, to cross-linking of molecular films to obtain tailor-made chemical and mechanical properties by exploiting the intriguing kinematics of collision between hyperthermal hydrogen molecules and hydrogen in C–H bonds, and by optimizing the curing process as a function of hydrogen fluence, energy, and precursor selection. The HHIC approach is extremely useful in applications where it is undesirable to use chemical initiators, additives, or catalysts. Hence, it is compatible with most device-fabrication technologies as well as surface-initiated polymerization and grafting of various chemical moieties onto incompatible surfaces. In the field of solution-based organic electronics, the HHIC promises to deliver a significant increase in electrical conductivity upon shielding the sample from plasma radiation.

The plasma radiation can be screened out in various ways. The easiest approach is to use three "grounding" electrodes instead of one. In fact, only the first one is at a ground potential, whereas the other two share the same potential as the accelerating electrode, which is in the proposed setup (Figure 54) effectively redundant. The top two electrodes (see Figure 4) are machined using the same pattern of hole positioning and separated by ~1 mm. The second electrode is negatively biased to extract positive ions from the plasma chamber with a minimal loss in the overall flux. The third electrode is designed in such a manner that the holes are shifted by half a distance between the centres. This creates a barrier for the electromagnetic waves to pass inside the drift zone. Only a small portion escapes due to reflection. Unfortunately, it also creates a barrier for fast moving perpendicular ions. However, in this case, we rely on Coulomb interaction between the ions to alter their trajectories and allow some of them to leave this region and enter the drift zone. It is just a matter of finding the right separation between the electrodes in order to maintain a high flux of extracted ions as has been verified by SIMION®.

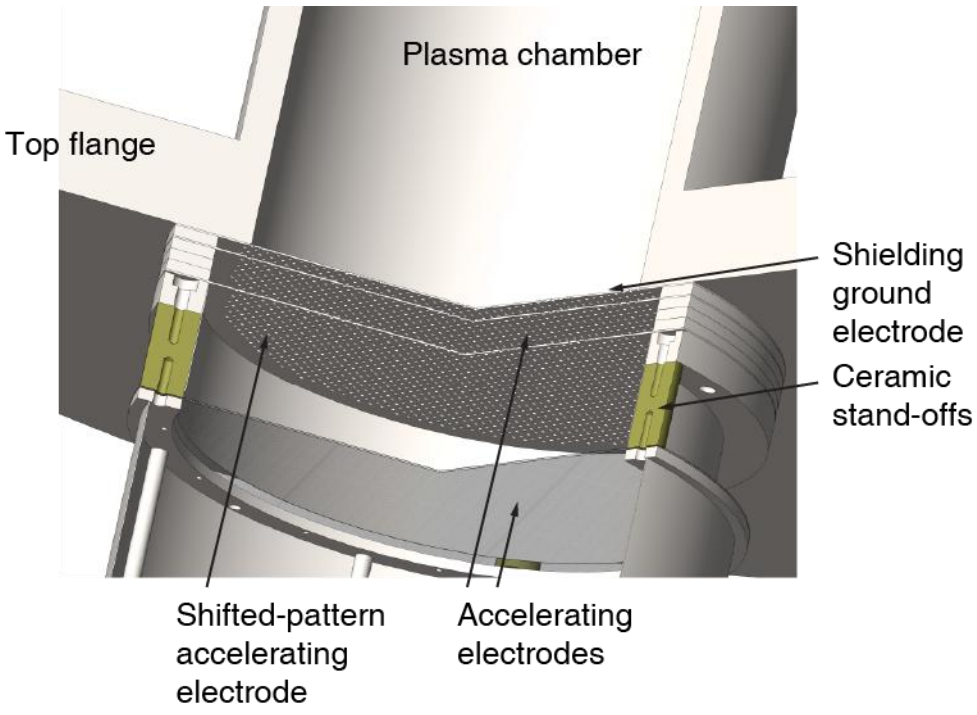

Figure 54. Ion extraction configuration as proposed to minimize the intensity of escaping plasma radiation.

It is also possible to place the plasma chamber out of line-of-sight of the drift zone and the sample area by introducing an elbow piece thus bending the ion trajectories. In this configuration, the system would have to be equipped with an electrostatic ion mirror to deflect extracted ions into the drift zone.

Another issue that has not been satisfactorily resolved is the actual energy distribution of hyperthermal neutral projectiles. We are now aware of the fact that the entrance to the quadrupole mass spectrometer has to be in close proximity to the reaction chamber in order to detect a distinguishable signal of hyperthermal hydrogen neutrals. Figure 55 depicts a proposed modification of the HHIC reactor effectively placing the RGA head near the reaction chamber by expanding the separating plate into a region of the analytical chamber. Although this solution is not ideal, it is the only realistic solution because the use of RGA requires differential pumping and therefore the use of another vacuum pump of finite physical dimensions connected to the system using a tee piece. It

would not be economically feasible to tackle this issue in an "opposite" manner—moving the RGA head up, close to the original separating plate.

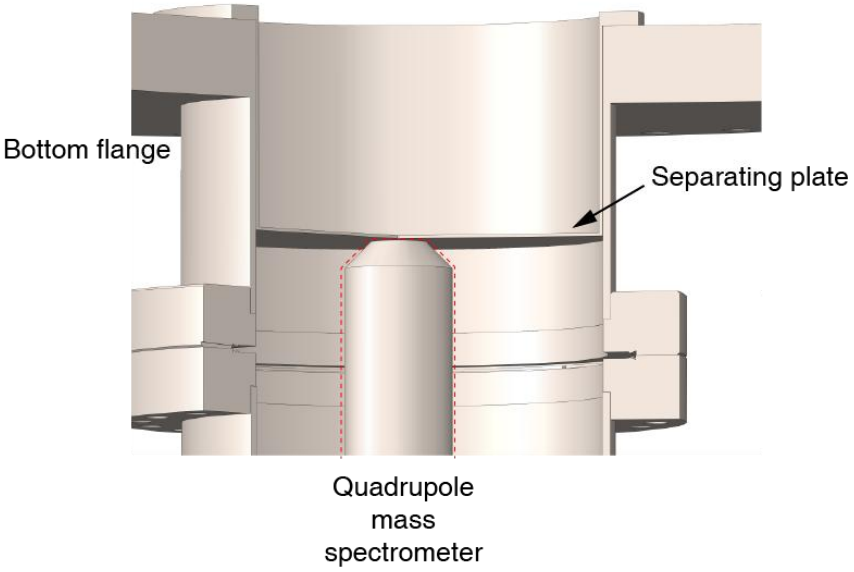

Figure 55. Modification of the HHIC reactor to measure the energy distribution of hyperthermal neutral projectiles using a quadrupole mass spectrometer.

The HHIC method is also suitable for industrial processing due to its high throughput, low energy consumption, and low consumption of the feedstock gases. In Figure 56 we show two examples of implementation of HHIC into an industrial environment: a) assembly line approach requiring the use of differential pumping, and b) replaceable cylindrical cassettes.

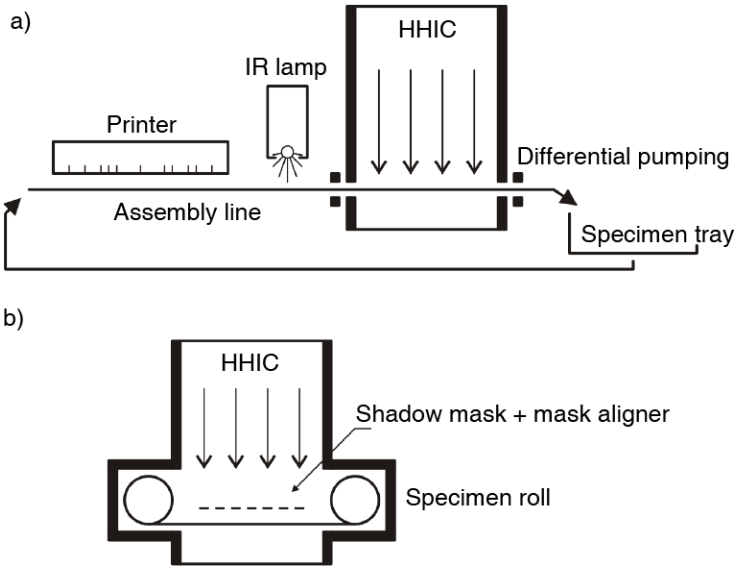

Figure 56. Modification of the HHIC reactor operation for use in industrial environment.

In summary, "chemistry with hyperthermal H_2 as a scalpel" is a unique technology capable of engineering both intra- and inter-molecular cross-linking with high throughput, negligible side reactions, and low energy consumption. This approach is scientifically intriguing because it combines the physics of particle collisions with the chemistry derived from collision-induced dissociation. Although our approach focuses narrowly on cleaving C–H bonds without breaking other bonds, the niche has a wide scope of applications.

Appendices

Appendix A: Reactor operation

The following paragraphs will help the reader understand the HHIC reactor from the point of view of an operator running an experiment. The system as a whole consists of what was described in the previous section—on a construction level of fundamental parts directly related to the HHIC operation—as well as power supplies (both proprietary and commercial), read-outs, gas cylinders, gas lines, and various valves. The operator has to be familiar with vacuum technology and must understand all potential risks of operating a HHIC reactor filled with hydrogen gas. Especially because the HHIC reactor is a research-grade reactor, which neither restricts the user (in any way) nor provides any failsafe mechanisms.

Before an operator starts using the HHIC reactor, he/she must check which gas cylinder is currently connected to the reactor. Because the main gas used for HHIC is hydrogen, a hydrogen leak detector is available and regularly used to monitor whether the lower explosive limit of hydrogen in air was not exceeded.

The next step is an introduction of samples into the reactor. To prevent unnecessary contamination and allow for short pump times, it is imperative to keep both H_2 inlet valves closed before opening the reaction chamber to air. If the chamber was previously kept under vacuum, meaning all pumps had been running, the operator should wait until the current speed of a turbo pump reaches 30% of its nominal speed before introducing a venting medium (in our case dry nitrogen), otherwise he shortens its lifetime (mainly bearings). Another very important aspect of handling samples for vacuum operation is keeping them as clean as possible, meaning the operator should always wear gloves.

When a sample is inside the chamber and the shutter in place with the chamber closed, a gate valve situated in between the roughing pump and the turbo pump is opened and the turbo pump is switched on. Upon reaching the background pressure of $2x10^{-6}$ Torr, the operator introduces hydrogen gas into the chamber using inline flow-controllers to get the

reaction pressure (anywhere between 0.5 and 1.5 mTorr). The next step is to set up the right conditions for plasma initiation and to light it up: a) feed the solenoid electromagnet from a high-current power supply to reach the ECR magnetic field of 87.5 mT (the number of turns is chosen such that $I\,(A) \propto B\,(mT)$); b) inject the microwave energy (forward 200 W) with minimal reflection (reflected <10 W) into the plasma chamber. Before the bombardment of samples can be carried out, it is necessary to bias all three electrodes—one accelerating and two retarding. When all the parameters (pressure, microwave power, extraction current) are set and stable the operator opens up the shutter for a specific time exposing the sample to a beam of hyperthermal neutral hydrogen and inducing cross-linking.

Appendix B: Raw data

Table 5. Raw data for Figure 18.

Pressure (mTorr)	Yield (-)		
	E>5 eV	E>19 eV	E>40 eV
0.125	0.633	0.398	0.239
0.150	0.787	0.461	0.267
0.180	0.928	0.551	0.306
0.217	1.102	0.627	0.366
0.261	1.281	0.729	0.400
0.313	1.566	0.777	0.406
0.377	1.838	0.856	0.410
0.453	2.162	0.857	0.390
0.545	2.387	0.825	0.343
0.656	2.484	0.750	0.294
0.788	2.452	0.659	0.233
0.948	2.450	0.658	0.232
1.140	2.252	0.509	0.148
1.370	1.871	0.374	0.096
1.647	1.354	0.227	0.051
1.981	0.859	0.111	0.022
2.381	0.457	0.056	0.009
2.863	0.215	0.013	0.003
3.442	0.067	0.003	0
4.139	0.011	0	0
4.976	0.002	0	0
5.982	0	0	0
7.193	0	0	0

8.647	0	0	0

Table 6. Raw data for Figure 19.

Pressure (mTorr)	Yield for E>19 eV (-)		
	V_{acc}=−100 V	V_{acc}=−200 V	V_{acc}=−400 V
0.125	0.398	0.520	0.646
0.150	0.787	0.638	0.795
0.180	0.928	0.733	0.944
0.217	1.102	0.857	1.118
0.261	1.281	1.009	1.329
0.313	1.566	1.155	1.595
0.377	1.838	1.333	1.878
0.453	2.162	1.473	2.156
0.545	2.387	1.497	2.425
0.656	2.484	1.515	2.521
0.788	2.452	1.408	2.527
0.948	2.450	1.177	2.323
1.140	2.252	0.915	1.980
1.370	1.871	0.621	1.537
1.647	1.354	0.352	0.969
1.981	0.859	0.177	0.517
2.381	0.457	0.072	0.233
2.863	0.215	0.018	0.085
3.442	0.067	0.001	0.023
4.139	0.011	0	0.004
4.976	0.002	0	0
5.982	0	0	0
7.193	0	0	0
8.647	0	0	0

Table 7. Raw data for Figure 26.

Energy (eV)	Pressure (mTorr)				Acceleration voltage (V)		
	0.5	0.8	1.0	1.5	-50	-100	-200
3	310	70	520	890	270	80	370
3.1	230	50	760	970	210	137	317
3.2	290	220	800	1270	208	60	260
3.3	200	290	610	980	269	91	319
3.4	400	300	670	1010	266	110	304
3.5	130	60	670	1150	274	109	307
3.6	350	280	530	770	310	109	306

3.7	20	200	610	1120	360	164	334
3.8	260	110	590	1160	371	176	360
3.9	450	40	550	1390	373	164	339
4	170	230	690	1350	370	184	359
4.1	200	370	880	1210	341	141	331
4.2	320	360	550	1280	376	149	331
4.3	220	350	700	1380	337	147	323
4.4	350	30	740	890	310	103	299
4.5	270	290	820	1260	279	101	254
4.6	470	0	710	1130	271	101	243
4.7	260	90	800	990	247	67	176
4.8	220	120	560	1190	293	136	213
4.9	380	20	650	1220	279	121	200
5	400	90	560	820	317	139	201
5.1	280	20	610	810	347	150	233
5.2	240	510	800	1150	393	186	277
5.3	250	280	740	940	393	199	321
5.4	280	500	900	870	403	247	336
5.5	440	330	710	1110	389	180	294
5.6	280	340	920	1270	366	180	301
5.7	460	210	740	1300	334	137	313
5.8	640	300	1190	1270	301	151	284
5.9	400	560	1120	1460	304	149	283
6	700	520	1260	1820	320	126	310
6.1	640	430	1140	1650	370	114	376
6.2	660	490	1780	1670	403	144	429
6.3	780	800	1860	1700	454	140	447
6.4	1120	550	1450	2020	500	200	480
6.5	910	650	1940	2210	523	194	551
6.6	1000	880	1980	2340	554	217	601
6.7	1000	620	2320	2460	611	224	610
6.8	1260	660	2490	2360	574	231	631
6.9	1150	860	3000	3130	601	269	703
7	1240	1110	3050	3330	620	286	803
7.1	1490	1130	3310	3680	629	304	826
7.2	1800	1370	3750	4230	654	329	934
7.3	1950	1420	4440	4390	669	350	1070
7.4	1680	1550	4750	5340	664	406	1199
7.5	2240	1580	5360	5080	721	429	1300
7.6	2140	1780	6040	5970	729	444	1434
7.7	2690	2220	6290	6470	739	520	1571

7.8	2870	2410	6880	7190	779	590	1824
7.9	3520	2500	7140	7160	876	703	2003
8	3730	2400	7950	6740	963	743	2110
8.1	3840	2620	7430	7220	1027	809	2249
8.2	4090	2630	8920	6760	1130	930	2467
8.3	4340	2620	8150	7020	1191	1039	2593
8.4	4600	2900	8170	6890	1291	1096	2709
8.5	4560	3010	7790	6440	1319	1087	2729
8.6	4440	3070	7390	7210	1311	1090	2733
8.7	4080	2280	7440	6510	1257	1049	2674
8.8	3970	2520	6930	6530	1219	1041	2631
8.9	4030	2670	6830	6150	1150	1009	2569
9	3690	2670	6290	5830	1103	969	2461
9.1	3670	2550	6110	4880	1040	940	2347
9.2	3880	2360	5510	5060	1037	920	2231
9.3	3780	2370	5080	4760	960	834	2087
9.4	3430	2360	5070	4670	953	846	1997
9.5	3440	2100	4790	4300	947	834	1893
9.6	3090	2130	4800	4390	927	846	1720
9.7	3140	2110	4180	3910	873	770	1613
9.8	2340	1820	4080	3780	817	707	1540
9.9	2350	1760	3960	3510	751	636	1440
10	2420	1490	3730	3710	751	634	1349
10.1	2510	1470	3570	3950	730	629	1339
10.2	2240	1660	3370	3770	657	579	1213
10.3	1970	960	2820	2780	627	471	1147
10.4	1940	1190	2880	3060	636	476	1087
10.5	1930	680	2130	2880	636	476	960
10.6	1840	630	2200	2630	593	480	869
10.7	1720	1050	2270	2710	529	433	796
10.8	1410	650	2180	2420	470	404	660
10.9	1300	810	2050	2510	464	369	650
11	1160	860	1770	2010	406	381	590
11.1	1270	520	1860	2070	383	383	523
11.2	730	560	2080	2240	287	286	453
11.3	1210	470	1970	1960	340	289	480
11.4	1100	660	1940	2030	413	294	446
11.5	1020	740	2210	2270	450	303	454
11.6	1110	720	1980	2410	444	283	419
11.7	1210	710	1970	2390	486	234	407
11.8	1480	1030	3010	2900	483	204	427

11.9	1510	1120	3140	3400	567	249	487
12	1810	1220	3620	3300	566	241	463
12.1	2500	1240	4000	4430	576	243	534
12.2	2910	1570	5700	4800	574	193	590
12.3	3380	1350	7000	6260	627	194	611
12.4	4510	1970	8790	7570	681	227	731
12.5	5850	2460	10950	8660	787	260	793
12.6	7770	3490	13850	9360	886	310	890
12.7	10180	3890	16310	10720	986	354	1023
12.8	11520	4650	17240	11360	1086	411	1141
12.9	13070	6480	19380	12740	1224	477	1171
13	15240	7070	20060	12930	1280	523	1264
13.1	16910	7810	21160	13720	1384	551	1297
13.2	17690	8900	22580	13850	1431	541	1447
13.3	18850	9890	23150	14290	1540	563	1481
13.4	20380	9800	23240	13680	1573	549	1464
13.5	20340	9790	25050	14390	1611	527	1500
13.6	19430	11500	24360	14820	1710	526	1637
13.7	20780	12100	26130	16290	1801	584	1709
13.8	21210	11760	26890	16160	1887	603	1753
13.9	22260	11810	28200	17540	2023	656	1739
14	22860	12500	28750	17850	2040	676	1769
14.1	24280	14310	32060	19450	2180	723	1831
14.2	26020	14090	33520	21190	2266	754	1746
14.3	27260	15460	35120	22000	2230	793	1703
14.4	29550	16620	37760	23420	2323	759	1760
14.5	30730	18140	39560	24560	2336	759	1704
14.6	31190	17660	42250	26680	2374	744	1640
14.7	32310	19900	43460	27000	2417	771	1657
14.8	31070	19610	46600	28120	2434	787	1619
14.9	33270	21440	45630	29430	2471	836	1684
15	34580	21140	50000	30660	2591	804	1720
15.1	34790	22100	50180	31610	2603	833	1677
15.2	36950	23070	52440	32610	2650	863	1747
15.3	36920	23330	52770	32550	2624	813	1820
15.4	38390	23280	54590	33010	2600	761	1814
15.5	37390	23720	55500	33980	2573	729	1827
15.6	37930	22870	52890	33730	2527	701	1810
15.7	37230	24510	52060	35610	2433	740	1741
15.8	36380	22340	51600	33060	2307	704	1669
15.9	33770	22200	47140	32370	2144	630	1621

16	31990	20730	44370	31080	2007	677	1523
16.1	29240	19750	40350	29880	1953	656	1406
16.2	27010	18480	37130	26890	1824	621	1270
16.3	24350	17140	32800	24990	1687	603	1239
16.4	21950	16060	29150	22390	1524	543	1166
16.5	18580	13920	26120	19600	1431	521	1099
16.6	16740	12440	21730	16500	1301	467	911
16.7	12100	9950	17660	15250	1193	389	820
16.8	10490	7720	14650	12280	1066	346	810
16.9	8720	6400	12020	10220	896	253	753
17	7140	4840	10200	7620	820	197	614
17.1	6440	4080	7660	6980	696	139	491
17.2	4520	3290	6850	5720	714	121	454
17.3	3460	3130	5340	5100	696	83	410
17.4	2670	2440	4110	4310	686	90	317
17.5	2520	1590	3390	3190	590	46	194
17.6	2040	1290	2920	2610	597	110	170
17.7	1390	1460	2050	2200	591	103	107
17.8	1000	1060	1980	2020	621	64	23
17.9	910	550	1050	980	484	-59	-83
18	660	170	1310	1510	494	-11	-43
18.1	800	190	890	430	553	-13	7
18.2	380	240	1090	730	499	-81	-16
18.3	380	120	420	330	539	-64	24
18.4	450	100	860	180	550	-136	20
18.5	160	-60	120	60	574	-129	67
18.6	690	250	270	40	607	-64	104
18.7	120	-40	-130	280	589	-73	137
18.8	130	140	80	-20	464	-119	71
18.9	480	210	270	-380	541	-14	119
19	360	-170	-10	270	511	-73	21
19.1	170	-60	-30	170	483	-17	56
19.2	260	-10	-60	340	476	-50	117
19.3	-180	290	-150	790	461	-31	111
19.4	140	-150	-240	580	437	-59	11
19.5	310	-30	-310	-100	471	-54	29
19.6	360	70	-90	50	517	-99	1
19.7	-20	-390	-200	30	543	-94	74
19.8	190	-430	-250	-540	504	-104	84
19.9	70	140	310	500	529	-20	109
20	230	640	-150	100	609	-29	80

20.1	30	430	-290	-80	717	39	169
20.2	480	-580	-170	-40	707	83	194
20.3	-270	130	-430	70	653	71	153
20.4	190	30	-490	-170	674	66	134
20.5	260	-560	-570	-480	740	63	184
20.6	70	-30	220	540	786	73	139
20.7	180	380	-450	-100	681	-13	109
20.8	250	-10	-60	-220	627	-87	34
20.9	440	-450	-180	660	624	-177	-16
21	-150	-270	-830	550	680	-96	23
21.1	210	-590	40	-100	617	-156	-59
21.2	0	-280	-140	540	621	-144	-180
21.3	80	90	-380	-620	574	-219	-170
21.4	160	-160	560	-690	661	-133	-64
21.5	550	-220	-390	240	594	-99	-113
21.6	-190	400	270	-130	693	-96	-69
21.7	90	-500	100	190	671	-126	-73
21.8	210	-100	370	180	766	-27	67
21.9	220	550	-450	20	619	-154	-107
22	-90	350	-490	-570	609	-117	-220
22.1	240	-40	190	-390	653	-50	-231
22.2	340	-170	60	-420	709	-130	-316
22.3	10	270	-660	-500	701	-57	-321
22.4	30	70	330	-400	717	-184	-346
22.5	200	-70	600	-10	680	-296	-439
22.6	190	-200	-240	-430	916	-243	-234
22.7	160	-500	0	180	820	-431	-294
22.8	-50	20	-40	420	847	-586	-371
22.9	-230	440	-560	230	829	-510	-296
23	330	-10	80	-20	881	-416	-276
23.1	120	-40	-780	-970	920	-346	-183
23.2	360	280	-980	-440	1054	-281	-141
23.3	150	-140	-180	-580	993	-161	-74
23.4	810	80	-300	950	1010	-116	-27
23.5	270	-310	440	-290	989	-73	-111
23.6	100	120	-390	-720	1113	-84	-64
23.7	590	-10	-220	-660	1059	-253	-197
23.8	-160	-940	-1670	-40	1053	-184	-300
23.9	330	150	-410	-260	1017	-143	-244
24	-160	-20	-340	-500	1070	-206	-293
24.1	-290	230	-450	-1100	1100	-239	-327

24.2	770	-270	-860	-210	1123	-319	-346
24.3	40	230	-400	-800	1039	-411	-446
24.4	600	-270	-550	-430	1074	-403	-366
24.5	-80	40	-880	-430	1110	-603	-439
24.6	-30	-390	-560	-660	1100	-717	-596
24.7	-210	780	-1260	20	1021	-771	-703
24.8	90	370	-1110	-130	1118	-666	-614
24.9	-70	-30	-450	-20	1200	-733	-677
25	610	-190	-730	-730	920	-350	-620

Table 8. Raw data for Figure 30.

Energy (eV)	p=0.5 mTorr		p=0.8 mTorr		p=1.0 mTorr	
	Current (A)	Intensity (-)	Current (A)	Intensity (-)	Current (A)	Intensity (-)
0	1.15E-09	9.59E-12	4.03E-10	8.36E-12	3.00E-10	8.67E-13
2.5	1.13E-09	7.49E-12	3.82E-10	8.21E-12	2.98E-10	3.41E-12
5	1.12E-09	4.75E-12	3.62E-10	1.08E-11	2.83E-10	7.48E-12
7.5	1.10E-09	8.15E-12	3.28E-10	1.58E-11	2.61E-10	1.23E-11
10	1.07E-09	1.19E-11	2.83E-10	1.66E-11	2.22E-10	1.53E-11
12.5	1.05E-09	1.07E-11	2.45E-10	1.41E-11	1.84E-10	1.33E-11
15	1.02E-09	1.06E-11	2.12E-10	1.19E-11	1.55E-10	1.18E-11
17.5	9.93E-10	1.15E-11	1.86E-10	1.02E-11	1.25E-10	1.02E-11
20	9.64E-10	1.09E-11	1.62E-10	7.77E-12	1.04E-10	5.72E-12
22.5	9.38E-10	8.25E-12	1.47E-10	5.95E-12	9.65E-11	3.16E-12
25	9.22E-10	1.21E-11	1.32E-10	5.04E-12	8.85E-11	2.47E-12
27.5	8.78E-10	1.54E-11	1.22E-10	3.01E-12	8.42E-11	2.78E-12
30	8.45E-10	9.09E-12	1.17E-10	2.55E-12	7.46E-11	2.01E-12
32.5	8.32E-10	3.10E-12	1.09E-10	3.65E-12	7.41E-11	3.69E-12
35	8.30E-10	4.37E-12	9.86E-11	3.42E-12	5.62E-11	5.39E-12
37.5	8.10E-10	4.66E-12	9.18E-11	2.70E-12	4.72E-11	5.76E-12
40	8.06E-10	-6.47E-13	8.51E-11	4.21E-12	2.74E-11	9.59E-12
42.5	8.14E-10	-2.84E-12	7.07E-11	4.95E-12	-7.67E-13	1.12E-11
45	8.21E-10	-2.13E-12	6.03E-11	5.11E-12	-2.85E-11	1.02E-11
47.5	8.24E-10	-2.25E-12	4.52E-11	8.63E-12	-5.15E-11	8.89E-12
50	8.32E-10	8.02E-12	1.71E-11	9.95E-12	-7.29E-11	4.93E-12
52.5	7.84E-10	2.29E-11	-4.60E-12	5.63E-12	-7.62E-11	1.45E-12
55	7.17E-10	3.61E-11	-1.10E-11	2.51E-12	-8.02E-11	2.38E-12
57.5	6.04E-10	5.13E-11	-1.72E-11	1.86E-12	-8.81E-11	2.68E-12
60	4.61E-10	5.67E-11	-2.03E-11	7.67E-13	-9.36E-11	6.00E-14

62.5	3.20E-10	5.55E-11	-2.10E-11	3.20E-13	-8.84E-11	-6.47E-13
65	1.83E-10	4.37E-11	-2.19E-11	4.27E-13	-9.03E-11	1.48E-12
67.5	1.02E-10	2.35E-11	-2.31E-11	4.87E-13	-9.58E-11	1.18E-12
70	6.57E-11	9.95E-12	-2.43E-11	5.33E-13	-9.62E-11	1.87E-13
72.5	5.20E-11	4.08E-12	-2.58E-11	6.33E-13	-9.67E-11	1.91E-12
75	4.53E-11	1.81E-12	-2.75E-11	6.27E-13	-1.06E-10	1.37E-12
77.5	4.29E-11	2.47E-12	-2.89E-11	2.67E-13	-1.04E-10	-1.60E-12
80	3.29E-11	2.86E-12	-2.88E-11	-2.00E-14	-9.78E-11	1.66E-12
82.5	2.86E-11	1.56E-12	-2.88E-11	1.73E-13	-1.12E-10	5.60E-13
85	2.51E-11	6.73E-13	-2.97E-11	3.60E-13	-1.01E-10	-1.07E-13
87.5	2.53E-11	1.55E-12	-3.06E-11	1.67E-13	-1.11E-10	2.27E-12
90	1.74E-11	-4.60E-13	-3.05E-11	-4.00E-13	-1.12E-10	-6.00E-13
92.5	2.76E-11	2.47E-13	-2.86E-11	-3.33E-14	-1.08E-10	-4.53E-13
95	1.61E-11	1.07E-12	-3.04E-11	6.27E-13	-1.10E-10	6.13E-13
97.5	2.22E-11	5.33E-14	-3.18E-11	1.07E-13	-1.11E-10	8.80E-13
100	1.59E-11	9.13E-13	-3.09E-11	-3.47E-13	-1.14E-10	1.08E-12

Table 9. Raw data for Figure 32.

Energy (eV)	p=0.5 mTorr		p=0.8 mTorr		p=1.0 mTorr	
	Current (A)	Intensity (-)	Current (A)	Intensity (-)	Current (A)	Intensity (-)
0	9.90E-10	1.12E-11	1.36E-09	1.02E-11	9.32E-10	1.02E-11
2.5	9.62E-10	8.66E-12	1.31E-09	1.57E-12	9.07E-10	2.41E-12
5	9.46E-10	7.27E-12	1.34E-09	1.47E-12	9.20E-10	4.90E-12
7.5	9.25E-10	6.83E-12	1.29E-09	1.13E-11	8.82E-10	1.43E-11
10	9.12E-10	4.95E-12	1.23E-09	1.12E-11	8.49E-10	1.09E-11
12.5	9.01E-10	6.13E-12	1.18E-09	7.58E-12	8.28E-10	8.41E-12
15	8.81E-10	5.93E-12	1.15E-09	5.26E-12	8.07E-10	7.65E-12
17.5	8.71E-10	4.54E-12	1.13E-09	7.46E-12	7.89E-10	8.02E-12
20	8.59E-10	5.80E-12	1.08E-09	4.37E-12	7.67E-10	7.23E-12
22.5	8.42E-10	7.10E-12	1.08E-09	3.12E-12	7.53E-10	4.97E-12
25	8.23E-10	6.77E-12	1.05E-09	6.56E-12	7.42E-10	3.41E-12
27.5	8.08E-10	7.94E-12	1.02E-09	3.36E-12	7.36E-10	4.18E-12
30	7.84E-10	7.59E-12	1.01E-09	3.00E-12	7.21E-10	6.89E-12
32.5	7.70E-10	6.01E-12	9.89E-10	6.23E-12	7.02E-10	8.61E-12
35	7.53E-10	5.68E-12	9.52E-10	6.95E-12	6.78E-10	6.35E-12
37.5	7.42E-10	7.49E-12	9.19E-10	6.38E-12	6.70E-10	3.99E-12
40	7.16E-10	9.95E-12	8.89E-10	5.44E-12	6.58E-10	9.07E-12
42.5	6.92E-10	7.91E-12	8.65E-10	5.90E-12	6.24E-10	1.03E-11

45	6.76E-10	6.32E-12	8.30E-10	5.84E-12	6.07E-10	4.65E-12
47.5	6.60E-10	8.11E-12	8.07E-10	5.88E-12	6.01E-10	4.66E-12
50	6.36E-10	8.58E-12	7.71E-10	5.26E-12	5.83E-10	9.70E-12
52.5	6.17E-10	6.23E-12	7.54E-10	2.66E-12	5.53E-10	1.01E-11
55	6.05E-10	6.17E-12	7.44E-10	7.43E-13	5.33E-10	5.95E-12
57.5	5.87E-10	6.64E-12	7.47E-10	4.38E-12	5.23E-10	4.97E-12
60	5.72E-10	5.55E-12	7.01E-10	5.65E-12	5.08E-10	5.29E-12
62.5	5.59E-10	3.50E-12	6.90E-10	1.06E-12	4.96E-10	5.39E-12
65	5.54E-10	2.85E-12	6.90E-10	1.49E-12	4.81E-10	4.65E-12
67.5	5.44E-10	3.01E-12	6.75E-10	9.93E-13	4.73E-10	3.58E-12
70	5.39E-10	1.62E-12	6.80E-10	1.21E-12	4.63E-10	7.27E-13
72.5	5.36E-10	1.26E-12	6.63E-10	4.83E-12	4.70E-10	1.67E-13
75	5.33E-10	2.16E-12	6.32E-10	1.19E-12	4.62E-10	3.63E-12
77.5	5.26E-10	2.68E-12	6.51E-10	3.27E-13	4.51E-10	1.47E-13
80	5.19E-10	1.32E-12	6.28E-10	4.36E-12	4.62E-10	1.70E-12
82.5	5.19E-10	7.33E-14	6.08E-10	6.65E-12	4.43E-10	4.05E-12
85	5.19E-10	2.45E-12	5.62E-10	1.07E-11	4.41E-10	9.41E-12
87.5	5.07E-10	1.17E-12	5.01E-10	2.11E-11	3.96E-10	2.30E-11
90	5.13E-10	-3.19E-12	3.51E-10	2.83E-11	3.26E-10	2.73E-11
92.5	5.23E-10	-9.00E-13	2.17E-10	1.99E-11	2.59E-10	2.58E-11
95	5.18E-10	5.98E-12	1.52E-10	1.14E-11	1.97E-10	2.34E-11
97.5	4.93E-10	1.89E-11	1.03E-10	7.41E-12	1.42E-10	1.59E-11
100	4.23E-10	3.31E-11	7.79E-11	4.59E-12	1.18E-10	4.19E-12
102.5	3.27E-10	3.94E-11	5.68E-11	3.12E-12	1.21E-10	-2.00E-14
105	2.26E-10	3.51E-11	4.68E-11	6.50E-13	1.18E-10	1.37E-12
107.5	1.52E-10	2.31E-11	5.03E-11	-7.67E-13	1.14E-10	1.17E-12
110	1.11E-10	1.28E-11	5.44E-11	-7.73E-13	1.12E-10	5.07E-13
112.5	8.76E-11	7.93E-12	5.81E-11	9.77E-13	1.12E-10	1.45E-12
115	7.11E-11	5.80E-12	4.47E-11	3.28E-12	1.05E-10	1.87E-13
117.5	5.86E-11	3.63E-12	2.53E-11	6.70E-13	1.11E-10	3.93E-13
120	5.30E-11	2.24E-12	3.80E-11	-2.53E-12	1.03E-10	3.17E-12

Table 10. Raw data for Figure 33.

Energy (eV)	0 centre		45 side		45 centre	
	Current (A)	Intensity (-)	Current (A)	Intensity (-)	Current (A)	Intensity (-)
0	1.36E-09	1.02E-11	4.12E-10	2.61E-12	1.90E-09	5.47E-11
2.5	1.31E-09	1.57E-12	4.05E-10	2.44E-12	1.83E-09	4.85E-11
5	1.34E-09	1.47E-12	3.99E-10	3.51E-12	1.78E-09	3.58E-11

7.5	1.29E-09	1.13E-11	3.88E-10	3.54E-12	1.74E-09	3.60E-11
10	1.23E-09	1.12E-11	3.82E-10	5.05E-12	1.69E-09	5.71E-11
12.5	1.18E-09	7.58E-12	3.62E-10	1.44E-11	1.60E-09	1.24E-10
15	1.15E-09	5.26E-12	3.10E-10	2.53E-11	1.38E-09	2.65E-10
17.5	1.13E-09	7.46E-12	2.36E-10	2.13E-11	9.35E-10	3.54E-10
20	1.08E-09	4.37E-12	2.03E-10	8.39E-12	4.92E-10	2.84E-10
22.5	1.08E-09	3.12E-12	1.94E-10	2.36E-12	2.24E-10	1.43E-10
25	1.05E-09	6.56E-12	1.91E-10	2.43E-12	1.35E-10	4.40E-11
27.5	1.02E-09	3.36E-12	1.82E-10	3.05E-12	1.14E-10	1.34E-11
30	1.01E-09	3.00E-12	1.76E-10	2.60E-12	1.01E-10	1.18E-11
32.5	9.89E-10	6.23E-12	1.69E-10	3.90E-12	8.48E-11	1.17E-11
35	9.52E-10	6.95E-12	1.57E-10	4.11E-12	7.17E-11	1.81E-12
37.5	9.19E-10	6.38E-12	1.48E-10	3.84E-12	8.03E-11	2.19E-12
40	8.89E-10	5.44E-12	1.37E-10	3.97E-12	6.62E-11	6.56E-12
42.5	8.65E-10	5.90E-12	1.28E-10	3.83E-12	6.39E-11	2.33E-12
45	8.30E-10	5.84E-12	1.18E-10	3.22E-12	6.04E-11	-2.39E-12
47.5	8.07E-10	5.88E-12	1.12E-10	9.73E-13	6.99E-11	2.67E-12
50	7.71E-10	5.26E-12	1.13E-10	2.28E-12	5.37E-11	3.49E-12
52.5	7.54E-10	2.66E-12	1.01E-10	4.22E-12	6.11E-11	-8.01E-12
55	7.44E-10	7.43E-13	9.23E-11	3.92E-12	7.37E-11	4.00E-14
57.5	7.47E-10	4.38E-12	8.12E-11	4.29E-12	6.10E-11	2.21E-12
60	7.01E-10	5.65E-12	7.09E-11	3.01E-12	6.82E-11	-2.40E-12
62.5	6.90E-10	1.06E-12	6.62E-11	3.09E-12	6.70E-11	-3.47E-12
65	6.90E-10	1.49E-12	5.54E-11	3.43E-12	7.69E-11	-3.83E-12
67.5	6.75E-10	9.93E-13	4.90E-11	4.08E-12	7.66E-11	-2.85E-12
70	6.80E-10	1.21E-12	3.50E-11	2.54E-12	8.40E-11	0
72.5	6.63E-10	4.83E-12	3.63E-11	-8.40E-13	7.66E-11	6.27E-13
75	6.32E-10	1.19E-12	3.92E-11	5.20E-13	8.24E-11	-1.09E-12
77.5	6.51E-10	3.27E-13	3.37E-11	1.26E-12	7.93E-11	-4.93E-13
80	6.28E-10	4.36E-12	3.29E-11	4.13E-13	8.37E-11	-3.89E-12
82.5	6.08E-10	6.65E-12	3.16E-11	1.73E-13	8.91E-11	-2.73E-12
85	5.62E-10	1.07E-11	3.20E-11	-1.15E-12	9.05E-11	-2.01E-12
87.5	5.01E-10	2.11E-11	3.74E-11	-1.36E-12	9.41E-11	-1.40E-12
90	3.51E-10	2.83E-11	3.88E-11	-7.00E-13	9.40E-11	-1.08E-12
92.5	2.17E-10	1.99E-11	4.09E-11	8.00E-14	9.68E-11	-6.25E-12
95	1.52E-10	1.14E-11	3.84E-11	1.77E-12	1.10E-10	-1.69E-12
97.5	1.03E-10	7.41E-12	3.20E-11	-2.80E-13	1.01E-10	-9.60E-13
100	7.79E-11	4.59E-12	3.98E-11	-1.25E-12	1.12E-10	-2.93E-13
102.5	5.68E-11	3.12E-12	3.82E-11	-5.53E-13	1.02E-10	2.63E-12
105	4.68E-11	6.50E-13	4.26E-11	-8.73E-13	1.05E-10	-1.17E-12
107.5	5.03E-11	-7.67E-13	4.26E-11	1.13E-13	1.05E-10	-7.47E-13

110	5.44E-11	-7.73E-13	4.20E-11	4.53E-13	1.07E-10	-3.21E-12
112.5	5.81E-11	9.77E-13	4.03E-11	3.33E-13	1.13E-10	4.13E-13
115	4.47E-11	3.28E-12	4.04E-11	-2.60E-13	1.06E-10	4.88E-12
117.5	2.53E-11	6.70E-13	4.16E-11	-7.93E-13	1.01E-10	-2.51E-12
120	3.80E-11	-2.53E-12	4.43E-11	-1.08E-12	1.13E-10	-9.63E-12

Table 11. Raw data for Figure 34.

Accelerating voltage (V)	$\frac{t \text{ after HHIC}}{t \text{ of pristine sample}}$	Standard deviation	$\frac{t \text{ after washing}}{t \text{ of pristine sample}}$	Standard deviation
0	99	2	7	2
50	96	4	21	5
100	95	4	29	5
200	99	2	97	3
400	99	2	99	2

Table 12. Raw data for Figure 35a.

Pressure (mTorr)	$\frac{t \text{ after HHIC}}{t \text{ of pristine sample}}$	Standard deviation	$\frac{t \text{ after washing}}{t \text{ of pristine sample}}$	Standard deviation
0.5	98	1	99	2
0.8	97	4	97	2
1.0	99	3	85	4
1.5	98	3	71	7

Table 13. Raw data for Figure 35b.

Pressure (mTorr)	$\frac{t \text{ after HHIC}}{t \text{ of pristine sample}}$	Standard deviation	$\frac{t \text{ after washing}}{t \text{ of pristine sample}}$	Standard deviation
0.5	98	2	96	2
0.8	99	1	97	4
1.0	97	3	96	3
1.5	98	3	97	2

Curriculum Vitae

Name: Tomas Trebicky

Post-secondary Education and Degrees:
The Czech Technical University in Prague
Prague, Czech Republic
1998–2004 M.Sc.

The University of Western Ontario
London, Ontario, Canada
2006–2011 Ph.D.

Honours and Awards:
Province of Ontario Graduate Scholarship
2009-2011

Related Work Experience
Research Assistant
The University of Western Ontario
2006–2011

Teaching Assistant
The University of Western Ontario
2006–2010

Publications:

T. Trebicky, P. Crewdson, M. Paliy, W.M. Lau *et al. Proceeding of the National Academy of Sciences*, submitted, **2011**.

D. Thompson, T. Trebicky, W. M. Lau *et al. Langmuir*, accepted, **2011**.

W.M. Lau, T. Trebicky *Encyclopedia of Mass Spectrometry, Volume 5 Elemental and Isotope Ratio Mass Spectrometry, Chapter III, Section C*, **2009**, ISBN: 978-0-08-043804-7.

W.M. Lau, T. Trebicky, H.-Y. Nie *US Patent Pending*, **2010**, 349-133-P.

W.M. Lau, T. Trebicky, D.-Q. Yang *US Patent Pending*, **2010**, 349-132-P.

J. Voves, T. Trebicky, R. Jackiev *Journal of Computational Electronics*, **2007**, 6: 259-262.

Presentations:

NanoONTARIO (*University of Western Ontario, London, Canada, **2010***), poster.

International Conference on Computer as a Tool (*Belgrade, Serbia & Montenegro, **2005***), oral.

24th International Conference on Microelectronics (*University of Nis, Nis, Serbia & Montenegro, **2004***), oral.